Reconfigurable contour beam synthesis using a mechanical FEM surface description of dual offset reflector antenna surfaces

W.H. THEUNISSEN

A thesis submitted in partial fulfillment of the requirements for the degree of
Philosophiae Doctor

in the
FACULTY OF ENGINEERING
UNIVERSITY OF PRETORIA
SOUTH AFRICA
January 1999

TABLE OF CONTENTS

ACKNOWLEDGEMENTS

I would like to acknowledge the help and encouragement of the following people:

Professors J. Joubert and W.J. Odendaal of the University of Pretoria, my study leaders, Professor W.D. Burnside of The Ohio State University ElectroScience Laboratory, for all his help and advice, Professor G. Washington of the Smart Materials and Structures Laboratory at The Ohio State University.

I would also like to thank Hwansik Yoon for his valuable help in understanding mechanical finite element analysis and for writing the FEM unit of the diffraction synthesis code and Dr. Teh-Hong Lee, Dr. Hsi-Tseng Chou and Prof. P.H. Pathak for their help and support.

This dissertation is dedicated to Heidi.

LIST OF FIGURES

Chapter 1: Introduction

In this chapter a brief description of geostationary satellites, the motivation for the study of reconfigurable contour beam reflector antennas and this study in particular, and an outline of this dissertation are presented.

1.1. Geostationary satellites

Satellites have been in practical use in telecommunications since Echo 1, a 26.5 inch magnesium sphere launched by a Thor Delta rocket on August 12, 1960 bounced a taped message transmitted from Goldstone, California that was received by the Bell telephone laboratory a Holmdel, N.J. Echo I stimulated a great deal of interest in the development of active communication which lead American Telephone and Telegraph Company (AT&T) to build Telstar, launched on July 10,1962. Telstar was an active satellite with a microwave receiver and transmitter. It was the first satellite to transmit live television and conversations across the Atlantic.

Geostationary satellites were proposed in 1947 by Arthur C. Clark (1917-), a British physicist and astronomer as a means to relay radio signals from one part of the world to another that is beyond the line of sight. Geostationary orbits are orbits occupied by communications satellites which remain at fixed points in the sky relative to observers on the ground. The are defined by an orbit period of one sidereal day, or about 23 hours 56 minutes 4 seconds. During one sidereal day the earth rotates about its polar axis exactly once. To be geosynchronous, a satellite must orbit the earth in the same period. This period defines the average orbit radius of 42155 km. This value is found from Kepler's third law. The earth's radius (6370 km) subtracted from the orbit radius determines the orbit above the earth to be 35785 km. This definition doesn't say anything about the shape of the orbit, or the orientation of the orbit plane with respect to the plane of the equator. The orbit can be highly elliptical, and/or it can be inclined with respect to the plane of the equator, and still be synchronous with the earth's rotation. In this case, a desired class of geosynchronous orbit is the geosationary orbit.

A satellite moving in a geostationary orbit remains at a fixed point in the sky at all times. This is desirable for radio communications because it allows the use of stationary antennas on the ground.

To be geostationary, the orbit must meet three criteria:

- The orbit must be geosynchronous.
- The orbit must be a circle.
- The orbit must lie in the earth's equatorial plane.

Individual satellites within the orbit are identified by the longitudinal position east or west of the prime meridian.

All geostationary orbits comply with the following:

PARAMETER	METRIC UNITS
Height above equator	35785 km
Average orbit radius	42155 km
Orbit circumference	264869 km
Arc length per degree	736 km
Orbital velocity	11066 km/h

To understand the importance of these criteria, consider the result if the orbit fails to meet them. If the orbit is not geosynchronous, the satellite does not move at the same rate as the earth's rotation. Thus, from the point of view of an observer on earth, the satellite appears to be in continuous motion, and it periodically disappears below the horizon. If the orbit is not a circle, the satellite does not move at a constant velocity (Kepler's second law). Instead, it appears to oscillate east-and-west at a rate of two cycles per sidereal day. If the orbit does not lie in the equatorial plane, the satellite does not remain at a fixed point in the sky. Instead, it appears to oscillate north-and-south at a rate of one cycle per sidereal day. The terms geosynchronous and geostationary are not synonymous: geosynchronous specifies only the orbit period, but geostationary also specifies the shape and orientation of the orbit.

These definitions are consistent with the definitions used by the United States Federal Communications Commission (FCC). The following definitions are quoted from the FCC rules, as published in Title 47, Section 2.1, of the United States Code of Federal Regulations:

Geostationary satellite: An earth satellite whose period of revolution is equal to th eperiod of rotation of the earth about its axis.
Geostationary satellite: A geosynchronous satellite whose circular and direct orbit lies in the plane of the earth's equator and which thus remains fixed relative to the earth; by extension, a satellite which remains approximately fixed relative to the earth.

The circular belt containing all the geostationary satellites is called the Clarke belt. Specific satellite positions in the Clarke belt are identified by longitude (or, more specifically, by the longitude of the point on the equator directly beneath the satellite). Figure 1 shows an example of a satellite in the Clarke belt.
The view from one geostationary satellite covers about 40% of the earths suface. At the equator, a 162°-segment of the Clarke belt is visible; the visible segment decreases as the latitude increases, and becomes zero at a latitude of 81.4°. North of 81.4° north latitude and south of 81.4° south latitude the Clarke belt is hidden below the horizon.

Dozens of satellites have been deployed along the Clarke belt in order to accommodate the ever-growing demand for communications capacity. In many parts of the Clarke belt, adjacent satellites use the same frequency band and are located within 2° of each other. A satellite intended for radio communications among fixed earth stations must remain at a fixed point in the sky. This means that the satellite must move in a geostationary orbit. The owners of most geostationary satellites try to maintain their satellites in a box measuring 0.1° x 0.1°. The satellite must be maintained at the proper attitude. This term describes the orientation of the satellite within its box. If the satellite is not maintained at the proper attitude, its antennas will not be aimed properly.

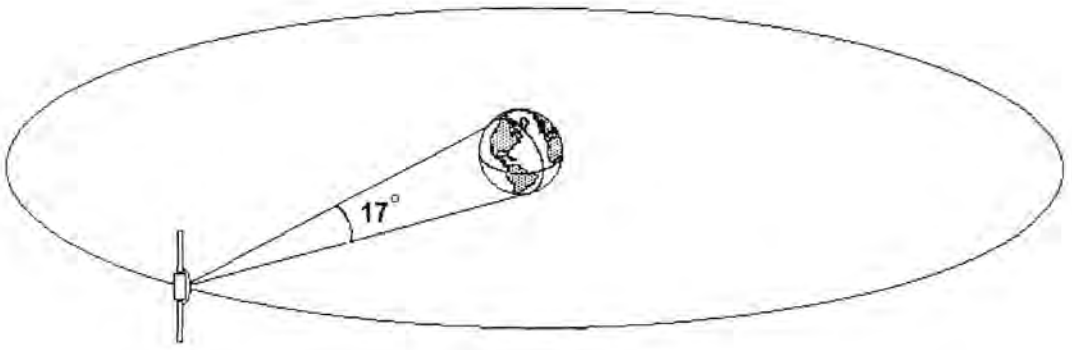

Figure 1. The subtended angle of the earth as seen from a satellite in the Clarke belt is approximately 17°.

Once a satellite is placed in proper position and attitude it tends to drift. Drift degrades the satellite performance in two ways: the satellite may move out of position, or it may assume an improper attitude. Drift results from external forces. While there are many external forces acting on the satellite, the primary forces are those exerted by the sun and other objects in the solar system.

The intensity and direction of the gravitational force exerted by the sun changes continuously in daily, yearly and 55-year cycles. The cyclic nature of this force tends to cancel its own effect; an easterly pull at one part of the cycle is offset by a westerly pull half a day later; similarly a northerly pull is offset by a southerly pull but there is a net resultant force which, over the course of several months causes the satellite to drift away from its geostationary position.

The gravitational pull of other objects in the solar system are considerably weaker than the sun's gravity, and their effects can be measured and predicted. Precise orbit calculations usually account for the moon's gravity, and frequently include the gravitational forces of other planets as well. The uneven distribution of land mass on the surface of the earth also causes mainly east-west drift. To counteract these forces, the satellite must be fitted with some mechanism to move the satellite back into positions when it drifts.

If the satellite is allowed to drift freely two effects manifest itself. First the orbit plane becomes inclined with respect to the earth's equatorial plane. During the course of one sidereal day, the satellite makes one complete revolution around the earth. The orbit plane must pass through the earth's center of gravity (Kepler's first law) which means the satellite must pass through the earth's equatorial plane twice each sidereal day. The satellite is north of the equatorial plane for half of each sidereal day and south of it for the other half. From a point on the earth's surface, the satellite appears to oscillate along its north-south axis at a rate of one cycle per sidereal day. Next, because of the conservation of angular momentum, the orbit assumes and elliptic shape. As a result, the satellite no longer moves at a constant velocity (Kepler's second law). From a point on the earth's surface, it appears to oscillate along its east-west axis at a rate of two cycles per sidereal day. Combining these two apparent motion the result is an elongated 'figure-8' pattern. The satellite complete one cycle along the figure-8 pattern each sidereal day. As the satellite continues to drift the figure-8 pattern becomes larger. Communication satellites are fitted with small rockets called thrusters. On command from a control station, a thruster is fired. During its firing, it ejects a gas propellant. The ejected gas produces the force to counteract these undesired motions. A ground control station precisely controls all the parameters involved in a firing: the position of each thruster relative to the satellite, the timing and duration of each fire and the pressure of the ejected propellant. If these parameters are controlled properly, the satellite can be maintained at the proper position and attitude for years. This process is called stationkeeping.

Every time a thruster is fired, propellant is used. Once the supply of propellant is exhausted the satellite cannot be maintained at proper position and attitude, and the satellite must be retired. Propellant capacity is the primary factor which determines the useful life of a communications satellite. A primary goal of every satellite owner is the conservation of propellant. Many studies have been done to determine the optimum trade-off between satellite stability and propellant usage. These studies have shown that a substantial majority of the propellant is used for just one stationkeeping function: keeping the satellite from drifting along its north-south axis. When the propellant is spent the satellite loses the ability of stationkeeping and becomes useless to the satellite

operator. The last of the propellant is used to decommission the satellite into graveyard orbit, which is usually just a highly inclined geosynchronous orbit to prevent congesting the Clarke belt.

Since 1963, approximately 400 satellites have been placed in geostationary orbit. Conservatively assuming an average lifetime of 8 years per satellite, these satellites have accumulated around 3200 years of in-orbit operation. As satellites are becoming more reliable and launch vehicles get better mass into orbit capability, the expected service life of the satellites will increase. Satellites are already achieving an expected operating service life of 15 years. This increases the probability that the satellite service area and/or satellite operator will change. The Canadian Anik series of satellites is an example of this. Anik C1 was launched on April 12, 1985 from the space shuttle Discovery during the STS-51D mission to a position at 72°W. Anik C1 was built for Telesat Canada by Hughes Aircraft Co., with Spar Aerospace Ltd. And other Canadian companies as subcontractors. It was owned and operated by Telesat Canada until it was replaced by later Anik satellites and sold to Paracomsat, an Argentine operator. Anik C2, otherwise known as Telesat 7, like Anik C1, was also sold to Paracomsat. Both C1 and C2 were later bought back by Telesat, leased to the UAE and were later used to provide coverage to the northern regions of Antartica. This example illustrate that the application and required geographical coverage of a geostationary satellite is very likely to change.

1.2. Antenna systems on geostationary satellites

Telecommunication services provided by satellite include television and telephone transponders and direct broadcast television (DBS). In the case of the first two services an operator will provide a service center or hub from where uplinks and downlinks to the satellite are made. This will be made from ground stations with high gain antennas. From the hub, the service is relayed into the terrestrial network. In the case of direct broadcast television a downlink service is provided to many users each using a lower gain antenna. For example, an 18'' aperture parabolic reflector antenna is used as a DBS receiver. The antenna on the satellite needs to provide coverage over a

geographical region called the service area as opposed to a single beam to each individual ground station. Shaped or contour beams are used on these satellites to increase antenna efficiency and reduce interference in geographical areas adjacent to the service area. The need for shaped or contour beams was a significant challenge to antenna engineers and several methods of implementing contour beams have been studied and used. These include arrays, array front fed paraboloids and shaped single and dual reflector antenna systems.

From the examples in the previous paragraph, it can be seen that there will be a definite advantage in the ability to reconfigure the contour beam to provide coverage for different geographical service areas and from different satellite geostationary positions. In order to comply with FCC regulations on the level of radiation allowed in areas outside the geographical coverage area, contour beams are subject to much more stringent specifications and this is also likely to be enforced on reconfigurable beams.

Reconfigurable contour beams can be implemented in a number of ways, including large aperture arrays, multiple feed reflector antennas and reflector antennas with adjustable main- and/or subreflector surfaces. The contour beam reflector antenna (CBRA) is widely used because of its versatility and low cost per unit aperture. The disadvantage of using the array fed offset reflector is that the beamforming network is heavy, lossy and expensive. The same disadvantage applies to the phased array antenna. Both type have complex components that need to be space qualified. Space qualification includes thermal, electromagnetic compatibility and mechanical (shock and vibration) tests and account for a significant portion of the total cost of the antenna subsystem [26]. The relative low cost of the shaped reflector antenna made it a popular choice for direct broadcasting satellites. The obvious disadvantage used to be the inability to reconfigure the contour beam. A reconfigurable CBRA has been implemented using an adjustable mesh main reflector and a cluster feed arrangement [4]. Another degree of freedom is added if the subreflector of a dual offset reflector antenna can be made adjustable. Piecewise adjustable subreflectors have been used in the past to correct for gravitational distortion in large axally symmetric dual reflector

radio telescope antennas [1,2] and have also more recently been proposed as a way to correct for main reflector distortion in dual offset reflector (DOSR) antennas [3].

1.3. The mechanical finite element diffraction synthesis technique

In this dissertation a novel way to design, synthesize and adjust the reconfigurable dual offset contour beam reflector antenna (DCBRA) using an adjustable subreflector is described. The DCBRA have been studied in this work using a variety of electromagnetic and mechanical analysis techniques which will be described in this dissertation. The reflector surfaces are treated by using a mechanical finite element surface description in a reflector diffraction synthesis code. The mechanical FEM module of the synthesis code was developed by the Smart Materials and Structures Division of the Mechanical Engineering department of The Ohio State University. The mechanical finite element code uses a shell element description and gets integrated into diffraction synthesis software to create a unique tool for studying problems like actuator placement, material property effects on the design and the achievable contour beam coverage. Reflector surface adjustment is studied using a set of linear actuators on the back of a stiff metal coated material and by bonding piezoelectric material onto the surface and applying a controlling voltage to it to change the shape [6]. Studies are mainly done for spaceborne applications, taking into account the fact that mechanical actuators can be difficult to design for use in space where smearing of mechanical components can be impossible in some cases due to the sublimation of smearing fluids like grease and oil.

The diffraction synthesis procedure and methods to calculate the far-field of the DOSR antenna efficiently is discussed in Chapter 2. This chapter includes a brief description of methods studied as possible candidates (including the Jacobi-Bessel method) for use in the diffraction synthesis code and a motivation for the choice of the selected method, a FFT based method, is given. Also included in this chapter is a description of the Gaussian beam method developed by Pathak [4]. This method was used for the first

time by Chou and Theunissen to synthesize a contour beam for an offset front fed parabolic reflector [5] and the advantages of this method is shown in this chapter.

The method of optimization is described in Chapter 3. The calculation of the cost function, that is the function that gets minimized during synthesis, is described and techniques used to minimize this function are introduced. In this chapter the advantages and disadvantages of global and local search techniques for this application are discussed and two methods are compared. These methods are the genetic algorithm and the steepest gradient solver. Both were used individually in some beam syntheses and also used in combination in other syntheses.

In Chapter 4 the mechanical properties of thin sheets are discussed and the set of differential equations governing their shape under different forces is shown. The feasibility of building a reconfigurable reflector antenna is demonstrated by a practical mechanical design using piezoelectric adjustable linear actuators. The design is based on a mechanical finite element analysis of four prototype surfaces and a subsequent actuator placement study. In this study, the main reflector was assumed to be fixed and an adjustable subreflector is designed using a flexible material called Lexan. An actuator placement study is described that was performed on materials with various stiffnesses to determine the suitability for this application by the Smart Structures division of the Mechanical Engineering department of The Ohio State University.

The diffraction synthesis procedure written by the author was modified to incorporate a mechanical finite element description of the surfaces of a dual reflector antenna. The mechanical FEM code designed by Yoon forms a unit in the contour beam synthesis software. This enables direct synthesis in terms of the exerted actuator forces on a surface with a predefined stiffness matrix. This also eliminates the second step of the design of a reconfigurable dual offset reflector antenna, the actuator placement study. In addition, many iterations can be performed much faster and more convenient, as opposed to the example in Chapter 4 where essentially only one mechanical iteration is done with considerable effort. The mechanical FEM diffraction synthesis software creates a unique and very useful tool to create a suitable design and predict the

performance of an antenna taking into consideration the mechanical properties of the reflector surface materials and the actuators used to reconfigure the antenna. The effect of different surface parameters and the required number of actuators and their placement were also studied and is described in Chapter 5. The technique is illustrated through a design of a reconfigurable DOSR antenna.

The dissertation concludes in Chapter 6 with a summary and conclusion.

Chapter 2: Diffraction synthesis and radiation pattern computation for reflector antennas

The diffraction synthesis procedure and methods to calculate the far-field of the DOSR antenna efficiently will be discussed in Chapter 2. This chapter includes a brief description of methods studied as possible candidates (the Jacobi-Bessel and p-series methods) for use in the diffraction synthesis code. The selected method, the p-series method, is compared in terms of accuracy and efficiency to a physical optics code developed at the Ohio State University by Lee and Rudduck [7]. Also included in this chapter is a description of the Gaussian beam method developed by Pathak [4]. This method was used for the first time to synthesize a contour beam for a front fed offset parabolic reflector by Chou and Theunissen [5] and the advantages of this method is shown in this chapter.

The analysis and design of reflector antennas evolved from the early numerical integration approaches to powerful techniques, such as the Jacobi-Bessel method, the Fourier-Bessel method, and sampling methods. One of the first attempts at improving the efficiency of the integration of the surface current density on the reflector was made by Ludwig. This was followed by Rusch's method [8]. Both these methods make use of asymptotic solutions to the radiation integral.

New integration techniques for the design of large, focused reflector antennas came in the last two decades. These include the Fourier-Bessel, Jacobi-Bessel and pseudo-sampling techniques. More recently, a Gaussian beam analysis technique was introduced. This method involves a closed form description of the reflected and diffracted fields of Gaussian beams from doubly curved surfaces with edges, which allows one to compute the far-field of reflector antennas extremely efficiently [4]. In this analysis the observer can be in the Fresnel or far-field region of the reflecting surface. This technique also gives the ability for diffraction synthesis of the near-field of a reflector antenna for special applications where the reflector is used in its near

field. This approach will have a very significant impact on future satellite antenna designs.

The calculation of the radiation pattern of the sub-reflector is performed by using techniques such as the GO/GTD approach [9] where the diffracted field contribution is approximated by a ray-optics field (analogous to the geometrical optics reflected field) which is regarded as originating at a point (or points) located on the rim of the sub-reflector.

Reflector shaping techniques for symmetrical and offset dual reflector systems also evolved from the early geometrical optics techniques to diffraction synthesis [3,10]. The diffraction synthesis technique described by Duan and Rahmat-Samii [11] in terms of the Jacobi polynomial surface description is relatively simple and produces smooth reflector surfaces with continuous first and second derivatives. In the results that follow in this chapter the main reflector of the dual offset reflector antenna is synthesized using this method. It is also used to obtain the initial boundary conditions for the subreflector actuators as will be described later, but the surface description for the subreflector is ultimately made in terms of a mechanical finite element matrix. This will be described in Chapter 5.

Paragraph 2.1 to 2.3 describe the geometry of the dual reflector antenna, show how the subreflector analysis and specular points are calculated and describe three techniques to calculate the far-field radiation pattern. Paragraph 2.4 describes a surface series expansion description in terms of the Modified Jacobi polynomials used in [11] and paragraph 2.5 shows verification of the accuracy of the p-series method and the Gaussian beam method by comparison to an existing full PO-PO solver developed at The Ohio State University. Paragraph 2.5 to 2.6 shows how the footprint is calculated and displayed graphically on a geocentric projection. This chapter leads up to Chapter 3 where the calculation of the cost function is described and a sample synthesis is performed.

2.1. Geometry of the dual reflector antenna and coordinate description

Figure 2 shows an unshaped Cassegrain dual reflector antenna configuration where the main reflector is described by

$$f(x',\ y') = -F + \frac{x'^2+y'^2}{4F^2} + \frac{y_c y'}{2F} + \frac{y_c^2}{4F^2} + z_{ref} \tag{2.1}$$

where y_c the paraboloid offset and F the focal distance of the paraboloid.

The subreflector is described in the x_s, y_s, z_s coordinate system by

$$z_s = -c \pm \sqrt{\frac{c^2}{e^2} + \frac{x_s^2+y_s^2}{e^2-1}} \tag{2.2}$$

where e is the eccentricity of the surface and c the half interfocal distance of the hyperboloid. The subreflector coordinate system is translated and rotated from the main coordinate system and is given by

$$\begin{bmatrix} x_s \\ y_s \\ z_s \end{bmatrix} = \begin{bmatrix} l_{s1} & m_{s1} & n_{s1} \\ l_{s2} & m_{s2} & n_{s2} \\ l_{s3} & m_{s3} & n_{s3} \end{bmatrix} \begin{bmatrix} x'-S_x \\ y'-S_y \\ z'-S_z \end{bmatrix} \tag{2.3}$$

with S_x ,S_y ,S_z the subreflector offset and l,m,n the direction cosines of the rotated axes with respect to the x', y', z' coordinate system.

The feed coordinate system is rotated and translated with respect to the subreflector coordinate system and is given by

$$\begin{bmatrix} x_f \\ y_f \\ z_f \end{bmatrix} = \begin{bmatrix} l_{f1} & m_{f1} & n_{f1} \\ l_{f2} & m_{f2} & n_{f2} \\ l_{f3} & m_{f3} & n_{f3} \end{bmatrix} \begin{bmatrix} x_s - x_{fs} \\ y_s - y_{fs} \\ z_s - y_{fs} \end{bmatrix} \tag{2.4}$$

with x_{fs}, y_{fs}, z_{fs} the feed offset and l,m,n the direction cosines of the rotated axes with respect to the x_s, y_s, z_s coordinate system. The direction cosines for the feed- and subreflector coordinate systems in Figure 2 are determined from spherical trigonometry.

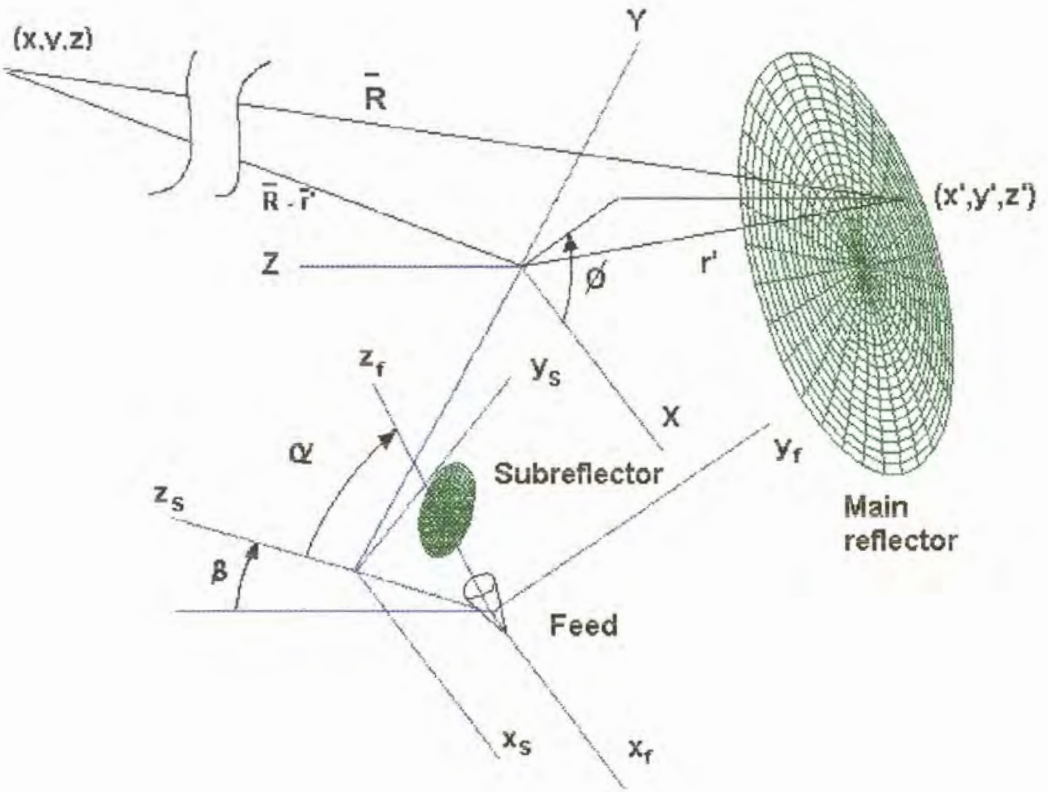

Figure 2. Geometry of the dual offset reflector antenna system.

The reflector antenna description in terms of direction coordinate matrices allows the capability to study the effect of lateral feed defocusing on main beam steering and finding optimum feed positions along the Petzval surface [8]. The effect of other parameters like the focal length/aperture on steering loss (the loss in gain per beamwidth steered) and beam shape and sidelobe level change due to beam steering can also be studied.

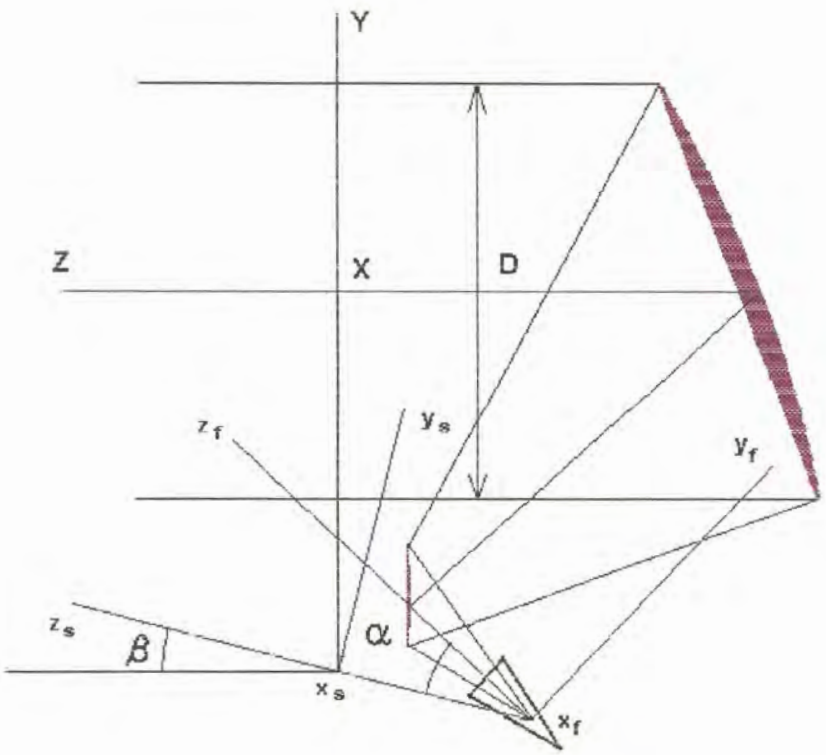

Figure 3. Geometry of Cassegrain dual offset reflector antenna.

2.2. Subreflector analysis

Subreflector radiation patterns can be calculated using UTD or equivalent current methods. Since the main reflector is not close to any incident or reflection boundaries for oversized subreflectors and speed is a high priority UTD is a natural choice. In this section aspects of the subreflector analysis as implemented by the author are addressed.

2.2.1. Calculation of specular points

The UTD implementation on the subreflector consists of an evaluation of the reflected field and the edge diffracted field . The reflected field is calculated by finding the specular point on the subreflector using the known feed position and the known point on the main reflector where the reflected field needs to be evaluated. In the subreflector coordinate system as shown in Figure 2 let (x_s, y_s, z_s) be the specular point on the subreflector, (x_{fs}, y_{fs}, z_{fs}) the feed position and (x_{in}, y_{in}, z_{in}) the point on the main reflector where the reflected field needs to be calculated. The direction cosines for the incident and reflected rays are given by

$$L_o = \frac{\left(x_{fs} - x_s\right)}{R_o}$$

$$M_o = \frac{\left(y_{fs} - y_s\right)}{R_o} \quad \text{, and} \qquad (2.5\text{-}2.7)$$

$$N_o = \frac{\left(z_{fs} - z_s\right)}{R_o}$$

where

$$R_o = \sqrt{\left(x_{fs} - x_s\right)^2 + \left(y_{fs} - y_s\right)^2 + \left(z_{fs} - z_s\right)^2} \qquad (2.8)$$

and

$$L_1 = \frac{\left(x_s - x_{In}\right)}{R_1}$$

$$M_1 = \frac{\left(y_s - y_{In}\right)}{R_1} \qquad (2.9\text{-}2.11)$$

$$N_1 = \frac{\left(z_s - z_{In}\right)}{R_1}$$

where

$$R_1 = \sqrt{\left(x_s - x_{In}\right)^2 + \left(y_s - y_{in}\right)^2 + \left(z_s - z_{In}\right)^2} \qquad (2.12)$$

The normal to the subreflector surface is taken in the direction of the illumination and is given by

$$\bar{n} = \left[\frac{\partial f}{\partial x_s}\hat{x}_s + \frac{\partial f}{\partial y_s}\hat{y}_s + \frac{\partial f}{\partial z_s}\hat{z}_s\right] \qquad (2.13)$$

with f as given by (2.1). Let the direction cosine of the normal of the subreflector surface be given by

$$L = \frac{\partial f}{\partial x_s} / |\vec{n}|$$

$$M = \frac{\partial f}{\partial y_s} / |\vec{n}| \text{ , and} \qquad (2.14 - 2.16)$$

$$N = \frac{\partial f}{\partial z_s} / |\vec{n}|$$

The following three nonlinear equations governing the reflection on the subreflector is derived from Snell's law

$$F_1 = z_s(t, \psi) - \sum_n \sum_m (C_{nm} \cos n\psi + D_{nm} \sin n\psi) F_m^n(t) \qquad (2.17)$$

where

$$t = \frac{\sqrt{x_s^2 + y_s^2}}{AS} \text{ , and} \qquad (2.18)$$

$$\psi = \tan^{-1}\left(\frac{y_s}{x_s}\right) . \qquad (2.19)$$

with AS as shown in Figure 10.

In addition, one finds that

$$F_2 = L_1 - L_0 - 2BL \text{, and} \qquad (2.20)$$

$$F_3 = M_1 - M_0 - 2BN \qquad (2.21)$$

where

$$B = LL_1 + MM_1 + NN_1 . \qquad (2.22)$$

AS is the radius of the projected expansion of the surface as described above. Following the procedure outlined in [12] Equations (2.17), (2.20) and (2.21) are solved using a Newton first order method.

The Newton method is implemented as follows: Using an initial guess to a solution of (x_0, y_0, z_0) the three nonlinear equations gives the following first order approximation

$$\begin{bmatrix} \frac{\partial F_1}{\partial x} & \frac{\partial F_1}{\partial y} & \frac{\partial F_1}{\partial z} \\ \frac{\partial F_2}{\partial x} & \frac{\partial F_2}{\partial y} & \frac{\partial F_2}{\partial z} \\ \frac{\partial F_3}{\partial x} & \frac{\partial F_3}{\partial y} & \frac{\partial F_3}{\partial z} \end{bmatrix} \begin{bmatrix} x - x_0 \\ y - y_0 \\ z - z_0 \end{bmatrix} \cong -\begin{bmatrix} F_1 \\ F_2 \\ F_3 \end{bmatrix} . \qquad (2.23)$$

This set of equations is solved to get a new approximation for (x, y, z) using LU decomposition. The new derivative matrix and solution is calculated and the new

solutions is used as the next approximation. This iteration is repeated until the difference between the new solution and the solution for the previous iteration falls into the prescribed tolerance. For an initial guess the specular point is calculated for the undeformed surfaces following [13]. Even for severely deformed reflectors and subreflector the specular point is found within less than 10 iterations within a tolerance of 10^{-6} as long as there are no inflection areas (areas where the second derivative changes sign) on the reflector surfaces. An advantage of using the surface series expansion in terms of the modified Jacobi polynomials is the surface produce no inflection areas which result in multiple specular points.

With the specular point known the radii of curvature of the subreflector and the first and second derivatives of the surface are calculated following [14]. The local properties of the surface are determined as follows:

A surface can be represented by the vector

$$\vec{r}(u, v) = (x(u, v), y(u, v), z(u, v)) \tag{2.24}$$

where (u,v) are the curvilinear coordinates of a point on the surface or alternatively

$$\vec{r} = \vec{r}(x, y) = (x, y, f(x, y)). \tag{2.25}$$

with tangent vectors

$$\vec{r}_u = \frac{\partial \vec{r}}{\partial u} = \left(\frac{\partial x}{\partial u}, \frac{\partial y}{\partial u}, \frac{\partial z}{\partial u}\right) \tag{2.26}$$

$$\vec{r}_v = \frac{\partial r}{\partial v} = \left(\frac{\partial x}{\partial v}, \frac{\partial y}{\partial v}, \frac{\partial z}{\partial v}\right) \tag{2.27}$$

In the surface series expansion the following relationships are used

$$u = t \tag{2.28}$$

$$v = \psi \tag{2.29}$$

with t and ψ as defined in (2.18) and (2.19).

The local properties of the surface are determined by a linear operator called the curvature matrix $\overline{Q}$. On the surface there is a normal $\hat{N}$ at each point. The variation of $\hat{N}$ is determined by the curvature of the surface at that point. Since $\hat{N} \cdot \hat{N} = 1$ differentiation with respect to u and v will give

$$\hat{N}_u \cdot \hat{N} = 0; \quad \hat{N}_v \cdot \hat{N} = 0 \tag{2.30}$$

which means that $\left(\hat{N}_u,\ \hat{N}_v\right)$ lies in the tangential plane to the surface at the that point.

This allows $\left(\hat{N}_u,\ \hat{N}_v\right)$ to be expressed in terms of $\left(\hat{r}_u,\ \hat{r}_v\right)$ as

$$-\hat{N}_u = Q_{11}\hat{r}_u + Q_{12}\hat{r}_v \tag{2.31}$$

$$-\hat{N}_v = Q_{21}\hat{r}_u + Q_{22}\hat{r}_v \tag{2.32}$$

and the four parameters in (2.70) and (2.71) form a curvature matrix

$$\overline{Q} = \begin{bmatrix} Q_{11} & Q_{12} \\ Q_{21} & Q_{22} \end{bmatrix} \tag{2.33}$$

Equations 2.70 and 2.71 may be rewritten as

$$-\left[\hat{N}_u \quad \hat{N}_v\right]^T = \overline{Q}\left[\hat{r}_u \quad \hat{r}_v\right]^T \tag{2.34}$$

$\left[\hat{r}_u \quad \hat{r}_v\right]$ is a 3 x 2 matrix given by

$$\left[\hat{r}_u \quad \hat{r}_v\right] = \begin{bmatrix} \frac{\partial x}{\partial u} & \frac{\partial x}{\partial v} \\ \frac{\partial y}{\partial u} & \frac{\partial y}{\partial v} \\ \frac{\partial z}{\partial u} & \frac{\partial z}{\partial v} \end{bmatrix}. \tag{2.35}$$

Similarly $\left[\hat{N}_u \quad \hat{N}_v\right]$ is given by

$$\left[\hat{N}_u \quad \hat{N}_v\right] = \begin{bmatrix} \frac{\partial \hat{N}}{\partial u}\cdot\hat{x} & \frac{\partial \hat{N}}{\partial v}\cdot\hat{x} \\ \frac{\partial \hat{N}}{\partial u}\cdot\hat{y} & \frac{\partial \hat{N}}{\partial v}\cdot\hat{y} \\ \frac{\partial \hat{N}}{\partial u}\cdot\hat{z} & \frac{\partial \hat{N}}{\partial v}\cdot\hat{z} \end{bmatrix}. \tag{2.36}$$

A fundamental matrix is introduced such that

$$\overline{I} = \begin{bmatrix} E & F \\ F & G \end{bmatrix} = \begin{bmatrix} \hat{r}_u\cdot\hat{r}_u & \hat{r}_u\cdot\hat{r}_v \\ \hat{r}_v\cdot\hat{r}_u & \hat{r}_v\cdot\hat{r}_v \end{bmatrix} \tag{2.37}$$

Another fundamental matrix is

$$\begin{aligned} \overline{II} &= \begin{bmatrix} e & f \\ f & g \end{bmatrix} = -\begin{bmatrix} \hat{N}_u\cdot\hat{r}_u & \hat{N}_u\cdot\hat{r}_v \\ \hat{N}_v\cdot\hat{r}_u & \hat{N}_v\cdot\hat{r}_v \end{bmatrix} \\ &= -\left[\hat{N}_u \quad \hat{N}_v\right]^T\left[\hat{r}_u \quad \hat{r}_v\right] \end{aligned} \tag{2.38}$$

which yields

$$\overline{II} = \overline{Q}\,\overline{I}. \tag{2.39}$$

The curvature matrix therefore given by

$$\overline{Q} = \overline{II}\ \overline{I}^{-1} \tag{2.40}$$

with

$$Q_{11} = \frac{eG - fF}{EG - F^2} \tag{2.41a}$$

$$Q_{12} = \frac{fE - eF}{EG - F^2} \tag{2.41b}$$

$$Q_{21} = \frac{fG - gF}{EG - F^2} \tag{2.41c}$$

$$Q_{22} = \frac{gE - fF}{EG - F^2} \tag{2.41d}$$

Once $\overline{Q}$ if found at a point on the surface the principal curvature and directions are found from the eigenvalues and eigenvectors of $\overline{Q}$. The mean and Gaussian curvatures are determined from

$$\kappa_M = \frac{1}{2}\left(\kappa_1 + \kappa_2\right) \tag{2.42}$$

$$\kappa_G = \kappa_1 \kappa_2 \tag{2.43}$$

where κ_1 and κ_2 are the two eigenvalues of $\overline{Q}$. The matrix $\overline{Q}$ can be diagonalized following the following procedure

Let the two eigenvectors of $\overline{Q}$ be denoted by

$$\vec{d}_1 = \begin{bmatrix} d_{11} \\ d_{21} \end{bmatrix} \tag{2.44a}$$

$$\vec{d}_2 = \begin{bmatrix} d_{12} \\ d_{22} \end{bmatrix} \tag{2.44b}$$

which satisfy

$$\overline{Q}\vec{d}_n = \kappa_n \vec{d}_n \quad , \quad n = 1,2 \tag{2.45}$$

The solutions of (2.45) are given by

$$\frac{d_{21}}{d_{11}} = \frac{\kappa_1 - Q_{11}}{Q_{12}} = \frac{Q_{21}}{\kappa_1 - Q_{22}} \tag{2.46a}$$

$$\frac{d_{12}}{d_{22}} = \frac{\kappa_2 - Q_{22}}{Q_{21}} = \frac{Q_{12}}{\kappa_2 - Q_{11}} \tag{2.46b}$$

A matrix $\overline{D}$ is formed such that

$$\overline{D} = \left[\vec{d}_1 \quad \vec{d}_2\right] = \begin{bmatrix} d_{11} & d_{12} \\ d_{21} & d_{22} \end{bmatrix} \tag{2.47}$$

Then the matrix

$$\overline{D}^{-1}\overline{Q}\overline{D} = \begin{bmatrix} \kappa_1 & 0 \\ 0 & \kappa_2 \end{bmatrix} \tag{2.48}$$

is the diagonalized curvature matrix. The first and second rows of the 2 x 3 matrix

$$\overline{D}^{-1}\left[\vec{r}_u \quad \vec{r}_v\right]^T \tag{2.49}$$

give the principal directions. After normalization the unit principal directions in (2.49) are given by

$$\hat{e}_1 = \frac{1}{\gamma_1}\left(\vec{r}_u + \alpha\,\vec{r}_v\right) \tag{2.50a}$$

$$\hat{e}_2 = \frac{1}{\gamma_2}\left(\beta\,\vec{r}_u + \vec{r}_v\right) \tag{2.50b}$$

where

$$\alpha = -\frac{d_{12}}{d_{22}} = \frac{Q_{22}-\kappa_2}{Q_{21}} = \frac{Q_{12}}{Q_{11}-\kappa_2} \tag{2.51a}$$

$$\beta = -\frac{d_{21}}{d_{22}} = \frac{Q_{11}-\kappa_2}{Q_{12}} = \frac{Q_{21}}{Q_{22}-\kappa_2} \tag{2.51b}$$

$$\gamma_1 = \left(E + 2\alpha F + \alpha^2 G\right)^{1/2} \tag{2.51c}$$

$$\gamma_2 = \left(\beta^2 E + 2\beta F + G\right)^{1/2} \tag{2.51d}$$

The four vectors $\vec{r}_u$, $\vec{r}_v$, $\hat{e}_1$, $\hat{e}_2$ lie in the tangent plane to the point on the surface and once $\overline{Q}$ is determined it is a straightforward matter to determine the principal directions and curvature from (2.51). A simple test to verify the accuracy of the code can be made for circularly symmetric surfaces by ensuring that radius of curvature (inverse of principal direction curvature) for the dependent variable in the normal direction touches the symmetry axis.

2.2.2. Edge diffraction

The diffracted field is calculated following [9] using the diffraction terms for a perfectly conducting wedge such as shown in Figure 4 and is given by

$$D_h(\phi, \phi', \beta_o, n) = \frac{-e^{-j\pi/4}}{2n\sqrt{2\pi k}\sin\beta_o}\left[\cot\left(\frac{\pi+\beta^-}{2n}\right)F\left[kL^{ri}a^+(\beta^-)\right] + \cot\left(\frac{\pi-\beta^-}{2n}\right)F\left[kL^{ri}a^-(\beta^-)\right]\right.$$
$$\left. \mp\left\{\cot\left(\frac{\pi+\beta^+}{2n}\right)F\left[kL^{rr}a^+(\beta^+)\right] + \cot\left(\frac{\pi-\beta^+}{2n}\right)F\left[kL^{rr}a^-(\beta^+)\right]\right\}\right] \quad (2.52)$$

with

$$L^i = \frac{s(\rho_e^i + s)\rho_2^i\rho_1^i}{\rho_e^i(\rho_1^i + s)(\rho_2^i + s)}\sin^2\beta_o \quad (2.53)$$

Note that ρ_1^i ρ_2^i the principal radii of curvature for the incident wavefront and ρ_e^i is the incident radius of curvature in the plane containing the incident ray and the edge and

$$L^r = \frac{s(\rho_e^r + s)\rho_2^r\rho_1^r}{\rho_e^r(\rho_1^r + s)(\rho_2^r + s)}\sin^2\beta_o \quad (2.54)$$

ρ_1^r ρ_2^r are the principal radii of curvature for the reflected wavefront and ρ_e^r is the reflected radius of curvature in the plane containing the reflected ray and the edge such that

$$\frac{1}{\rho_e^r} = \frac{1}{\rho_e^i} - \frac{2(\hat{n}\cdot\hat{n}_e)(\hat{s}'\cdot\hat{n})}{a_e\sin^2\beta_o} \quad (2.55)$$

where

$\hat{n}$ = normal to the surface at the diffraction point

$\hat{n}_e$ = normal to the edge curvature

$\hat{s}'$ = incident ray direction, and

a_e = radius of curvature of the edge.

Finally the remainder of the terms are given by

$$F(X) = 2j\sqrt{X}e^{jX}\int_{\sqrt{X}}^{\infty} e^{-j\tau^2}d\tau^2 \quad (2.56)$$

$$a^{\pm}(\beta) = 2\cos^2\frac{2n\pi N^{\pm}-\beta}{2}, \text{ and} \quad (2.57)$$

$$\frac{1}{\rho} = \frac{1}{\rho_e} - \frac{\hat{n}_e\cdot(\hat{s}'-\hat{s})}{a_e\sin\beta_o} \quad (2.58)$$

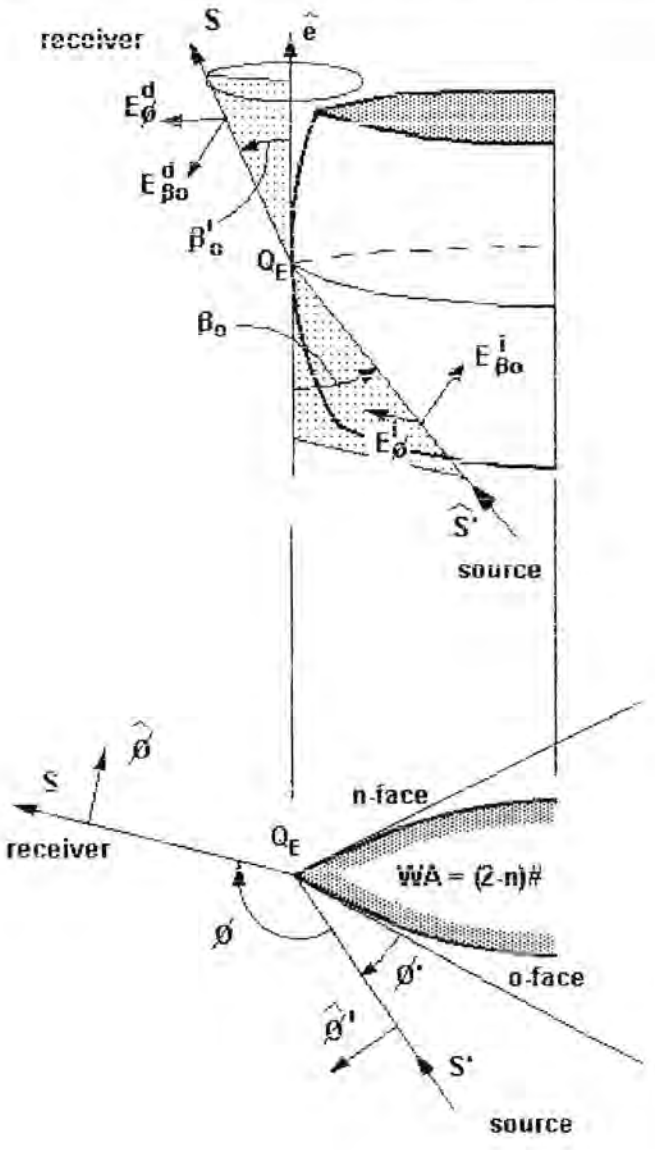

Figure 4. Perfectly conducting wedge for calculation of diffraction from subreflector edge.

For this particular problem only the diffracted field associated with the reflected shadow boundary (rn) was evaluated at points on the main reflector because the area subtended by the main reflector was sufficiently far out of the incident shadow boundary region. A rim search procedure is used on the subreflector to find the two extremes in the path length (points where $\beta_o = \pi/2$) and points along the rim in these two areas are used to find the required diffracted ray path to calculate the diffracted field.

2.3. Calculation of the far-field radiation pattern

As will be demonstrated in Chapter 3 a very efficient method to calculate the far-field radiation pattern of the main reflector is needed since it needs to be calculated so many times at many observation points during optimization. This paragraph discusses three methods that were evaluated for the purpose namely the p-series method, the Jacobi-Bessel method and the Gaussian beam method.

2.3.1. The p-series method

The far-field is calculated following [8] and [15]. In the coordinate systems of Figure 2, the main reflector surface is described by

$$z' = f(x', y') \tag{2.59}$$

and its unit normal is given by

$$\hat{n} = \bar{N} / |N| \tag{2.60}$$

where

$$\bar{N} = \left[\frac{\partial f}{\partial x} \hat{x}' - \frac{\partial f}{\partial y} \hat{y}' + \hat{z}' \right]. \tag{2.61}$$

The induced PO current on the reflector is given by

$$\bar{J} = 2\hat{n} \times \bar{H}_s(\vec{r}'). \tag{2.62}$$

The incident magnetic field is found by using GTD on the feed/subreflector combination described in the next section. The vector potential and the scattered fields from the main reflector is given by

$$\overline{A} = \iint_S \overline{J} \frac{e^{-jk|\vec{R}-\vec{r}'|}}{|\vec{R}-\vec{r}'|} dS \tag{2.63}$$

$$\overline{H} = \nabla \times \overline{A} \text{ , and} \tag{2.64}$$

$$\overline{E} = \frac{1}{j\omega\mu} \nabla \times \overline{H} \tag{2.65}$$

Substituting the far-field approximation $|\overline{R} - \vec{r}'| \approx \overline{R} - \overline{R} \cdot \vec{r}'$ into (2.63) allows the calculation of the required field quantities.

$$\overline{H} = jk \frac{e^{-jkR}}{4\pi R} \left(T_\phi \hat{\theta} - T_\theta \hat{\phi} \right), \text{ and} \tag{2.66}$$

$$\overline{E} = jk\eta \frac{e^{-jkR}}{4\pi R} \left(T_\theta \hat{\theta} + T_\phi \hat{\phi} \right) \tag{2.67}$$

where

$$\overline{T} = \iint_{S'} \overline{J}(\vec{r}) e^{jk\vec{R}\cdot\hat{r}'} dS' . \tag{2.68}$$

The integration in (2.14) is performed on the main reflector surface with the help of the surface Jacobian transformation given by

$$J_S = \sqrt{\left(\frac{\delta f}{\delta x'}\right)^2 + \left(\frac{\delta f}{\delta y'}\right)^2 + 1} \tag{2.69}$$

so that (2.68) is given by

$$\overline{T} = \iint_S \overline{J}(\vec{r}) e^{jk\vec{R}\cdot\hat{r}'} J_S dS \tag{2.70}$$

Equation (2.70) can be simplified by introducing the following definitions

$$\widetilde{J}(x', y') = \overline{J}(\vec{r}') J_S \tag{2.71}$$

and

$$\vec{r}'\cdot\hat{r} = z' \cos\theta + ux' + vy' \tag{2.72}$$

where

$$u = \sin\theta \cos\phi \quad , \quad \text{and} \tag{2.73}$$

$$v = \sin\theta \sin\phi \tag{2.74}$$

When (2.72) is substituted into (2.71) one obtains

$$T(u, v) = \iint_S \tilde{J}(x', y') e^{jkz' \cos\theta} e^{jk(ux'+vy')} dx' dy' \tag{2.75}$$

Equation (2.75) is rewritten as

$$T(u, v) = \iint_S \tilde{J}(x', y') e^{jkz'} \left[e^{-jkz'(1-\cos\theta)}\right] e^{jk(ux'+vy')} dx' dy' \tag{2.76}$$

so that a Taylor series expansion can be made for small values of θ

$$T(u, v) = \sum_{p=0}^{p \to \infty} \frac{1}{p!} \left[-jk(1 - \cos\theta)^p T_p\right] \tag{2.77}$$

where

$$T_p = \iint_S z'^p \tilde{J}(x', y') e^{jkz'} e^{jk(ux'+vy')} dx' dy' \tag{2.78}$$

Equation (2.77) is now expressed as a sum of Fourier transforms. The higher order terms only become significant for wide-angle observations. This form of the equation was implemented using an FFT algorithm and resulted in very fast evaluation of the radiation pattern with reasonable accuracy for the main beam and first few sidelobes.

2.3.2. The Jacobi-Bessel series expansion method

For a well focussed reflector system Equation (2.77) can be rearranged in a form for reflectors with elliptical apertures (circular apertures are a special case of these) that allows the Jacobi-Bessel series to be used the evaluate the Fourier transforms very rapidly. This was implemented following [8].

$$T_p = \iint_S \tilde{J}(x', y') e^{jkr' \cos\theta' \cos\theta} \{e^{jk\rho' \sin\theta \cos(\phi' - \phi)}\} \rho' d\rho' d\phi' \tag{2.79}$$

The factor in brackets in Equation (2.79) is the polar form of the Fourier kernel. This kernel is recast in the following form to have its center coincide with the pencil beam direction (θ_B , ϕ_B).

$$\left\{e^{jk\rho' \sin\theta \cos(\phi'-\phi)}\right\} = e^{jk\rho' \sin\theta \cos(\phi'-\phi)} e^{jk\rho'(C_u \cos\phi' + C_v \sin\phi')} \cdot e^{-jk\rho'(C_u \cos\phi' + C_v \sin\phi')} \quad (2.80)$$

where C_u and C_v are constants yet to be determined.

The following functionals are obtained by combining the first two terms on the right-hand side of (2.80), such that

$$B \cos\Phi = \sin\theta \cos\phi + C_u, \text{ and} \quad (2.81)$$

$$B \sin\Phi = \sin\theta \sin\phi + C_v. \quad (2.82)$$

B and Φ can be solved and the shifted kernel is obtained as

$$e^{-jk\rho'(C_u \cos\phi' + C_v \sin\phi')} e^{jk\rho' B \cos(\phi'-\Phi)} \quad (2.83)$$

Again using a Taylor expansion, the radiation pattern can be written as

$$\overline{T}_p = \frac{1}{p!}(jk)^p e^{jk(L_w - L_{wo})}(\cos\theta - \cos\theta_o)^p \cdot \int_0^{2\pi}\int_0^{D/2} \{\tilde{J}(\rho', \phi') e^{-jk\rho'(C_u \cos\phi' + C_v \sin\phi')} e^{jkL_o}[\tilde{f}(\rho', \phi') - \tilde{f}(\rho'_w, \phi'_w)]^p \cdot e^{jk\rho' B \cos(\phi'-\Phi)}\} \rho' \, d\rho' \, d\phi' \quad (2.84)$$

where L_o, L_w, L_{wo} functionals given by

$$L_o = L(\rho', \phi', \theta_o) = \tilde{f}(\rho', \phi') \cos\theta_o = z' \cos\theta_o$$
$$L_w = L(\rho'_w, \phi'_w; \theta_o) = \tilde{f}(\rho'_w, \phi'_w) \cos\theta_o = z'_w \cos\theta. \quad (2.85 \text{ a b c})$$
$$L_{wo} = L(\rho_w', \phi'_w; \theta) = \tilde{f}(\rho'_w, \phi'_w) \cos\theta_o = z'_w \cos\theta_o$$

The Fourier series basis functions can then be integrated against the Fourier transform kernel such that one obtains

$$\int_0^{2\pi} \begin{Bmatrix}\cos n\phi' \\ \sin n\phi'\end{Bmatrix} e^{j\xi\cos(\phi'-\Phi)} d\phi' = 2\pi j^n \begin{Bmatrix}\cos n\Phi \\ \sin n\Phi\end{Bmatrix} J_n(\xi) \quad (2.86)$$

where J_n is the n^{th} order Bessel function.

The modified Jacobi polynomials are defined as

$$F_m^{\alpha}(s) = \sqrt{2(\alpha + 2m + 1)} P_m^{(\alpha,0)}(1 - 2s^2) s^{\alpha} \quad (2.87)$$

where α is a real number and P is the Jacobi polynomial. This can be calculated from using the recurrence relationship. Figure 4 shows the modified Jacobi polynomials for m = 0, 1 and 2.

The first term under the integral in Equation (2.84) before the square brackets can be expanded as

$$\vec{Q}_p(\tfrac{D}{2}\,s',\,\phi) \;=\; \sum_{n=0}^{N\to\infty}\sum_{m=0}^{M\to\infty}[{}_p\vec{C}_{nm}\,\cos n\phi' + {}_pD_{nm}\,\sin n\phi'\,]F_m^n(s') \tag{2.88}$$

where

$$\rho' = \tfrac{D}{2}\,s' \tag{2.89}$$

and ${}_pC_{nm}$ and ${}_pD_{nm}$ are constant vector coefficients constructed by using the orthogonality of the expansion functions.

These constants are obtained from

$$\begin{Bmatrix} {}_p\vec{C}_{nm} \\ {}_p\vec{D}_{nm} \end{Bmatrix} \;=\; \tfrac{\varepsilon_n}{2\pi}\int_0^{2\pi}\int_0^{1}\vec{Q}_p(\tfrac{D}{2}\,s',\,\phi')\begin{Bmatrix}\cos n\phi' \\ \sin n\phi'\end{Bmatrix}F_m^n(s')s'\,d\phi'\,ds \tag{2.90}$$

where ε_n takes on the value of 1 for n=0 and 2 for n≠0.

The expression for the radiation integral is finally given by

$$\begin{aligned}\vec{T}(\theta,\,\phi) \;=\; & 2\pi a^2 e^{jk(L_w - L_{w\phi})}\sum_{p=0}^{P\to\infty}\frac{1}{p\,!}\,(jk)^p(\cos\theta - \cos\theta_o)^p \\ & \cdot\sum_{n=0}^{N\to\infty}\sum_{m=0}^{M\to\infty} j^n[{}_p\vec{C}_{nm}\,\cos n\Phi + {}_p\vec{D}_{nm}\,\sin n\Phi] \\ & \cdot\sqrt{2(n\,+\,2m\,+\,1)}\;\tfrac{J_{n+2m+1}(kaB)}{kaB}\end{aligned} \tag{2.91}$$

where a=D/2.

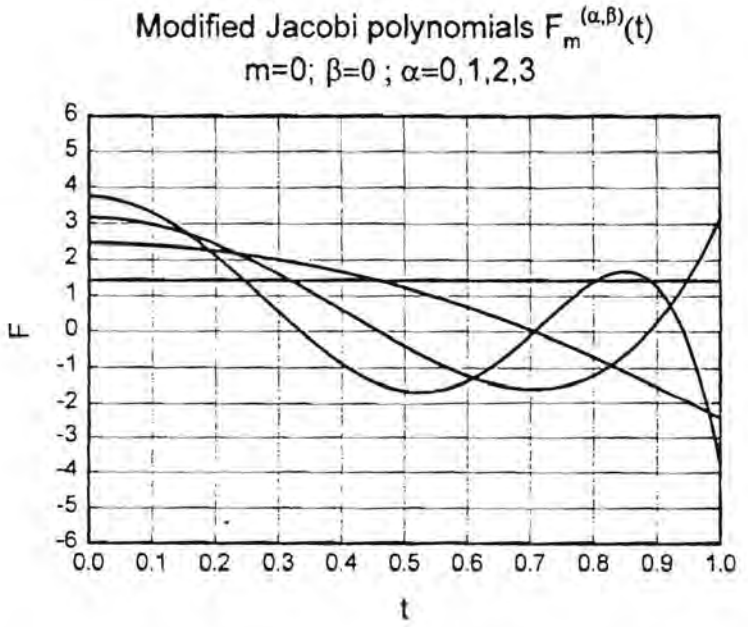

Figure 5 (a) Modified Jacobi polynomial for m=0.

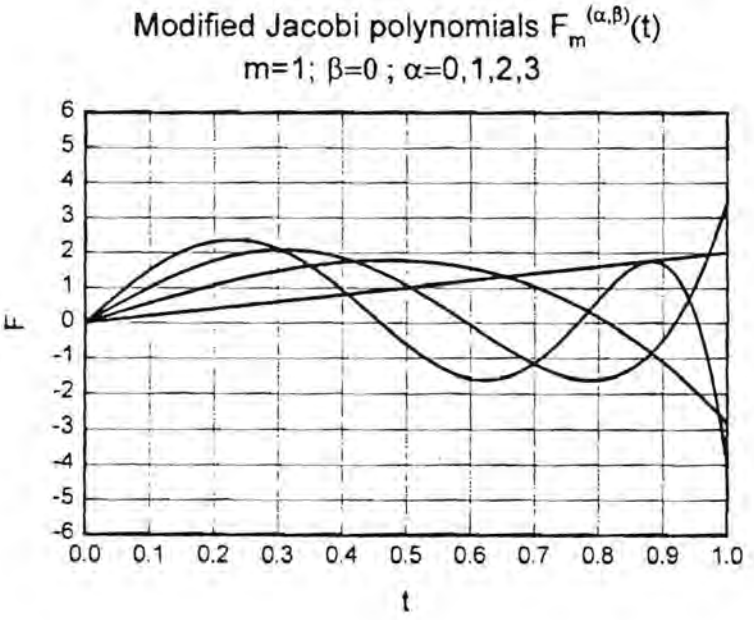

Figure 5 (b) Modified Jacobi polynomials for m=1

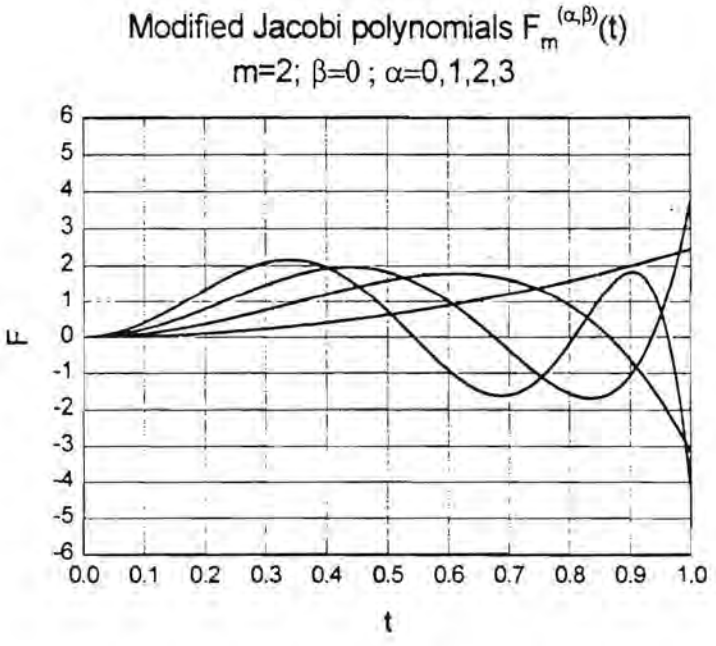

Figure 5 (c). Modified Jacobi polynomial for m=2.

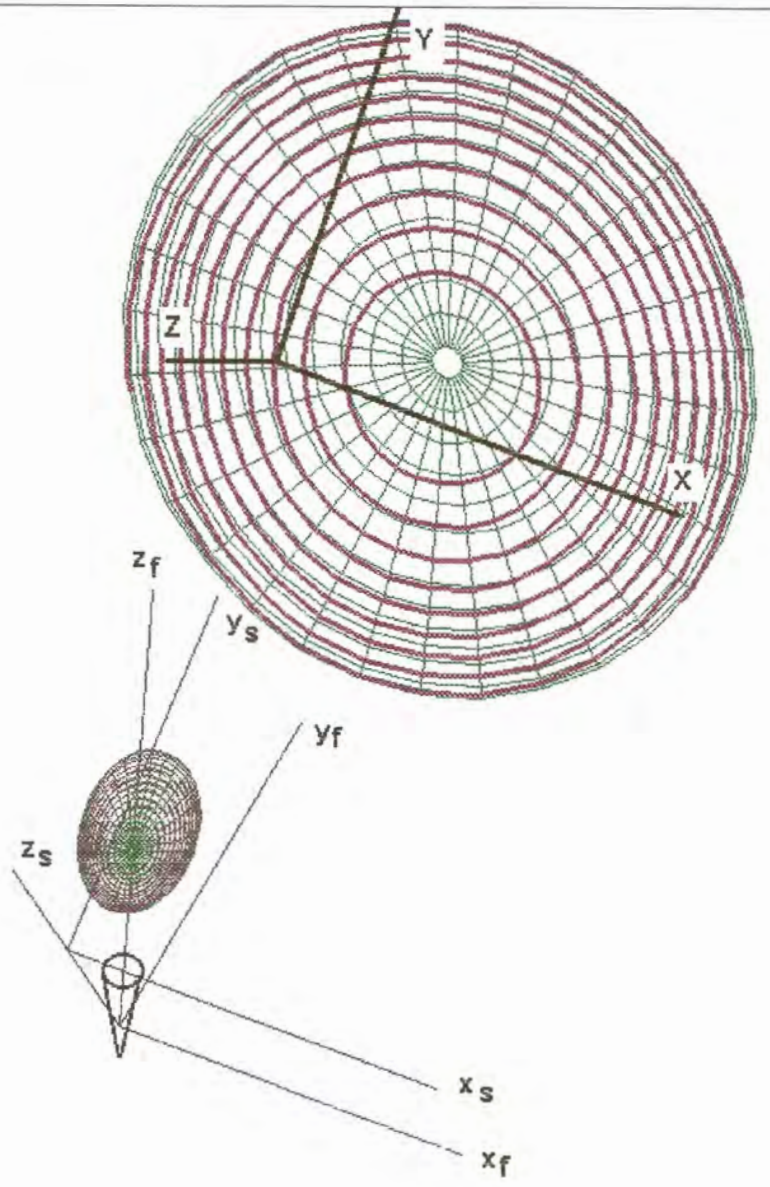

Figure 6. Co-polarized surface current density contours for a Cassegrain type dual offset reflector antenna. The current density contour interval is 1 dB.

Equation (2.91) was used to calculate the radiation pattern for the geometry shown in Figure 6. Note that once the ${}_pC_{nm}$ and ${}_pD_{nm}$ coefficients are determined, they can be used for all observation angles. Thus the numerical evaluation of the integral needs to be performed only once and not at every point in the far-field. The dominant behavior in the vicinity of B=0 is the Airy disc function $J_1(\xi)/\xi$.

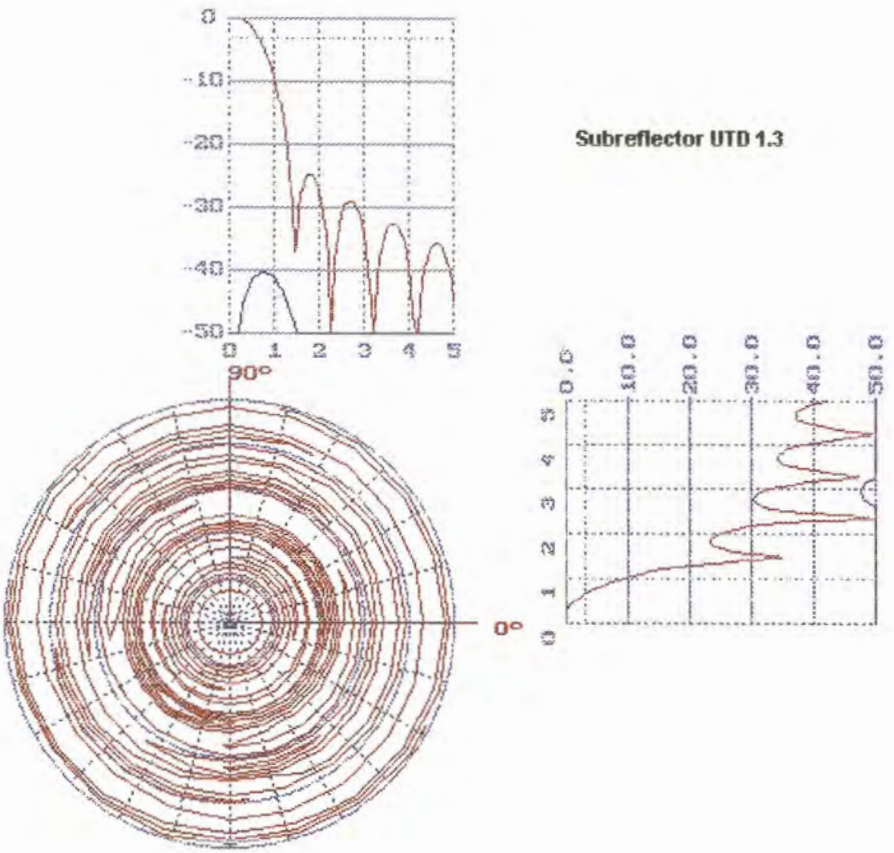

Figure 7. Far-field radiation pattern for the Cassegrain DOSR geometry shown in Figure 6.

Figure 6 shows the surface current density contour on the reflector surfaces for a focussed 60 wavelength aperture Cassegrain dual offset reflector antenna and Figure 6 shows the radiation pattern calculated using the technique outlined above. The number of terms used in the series were determined by comparison of the single reflector results given in [8].

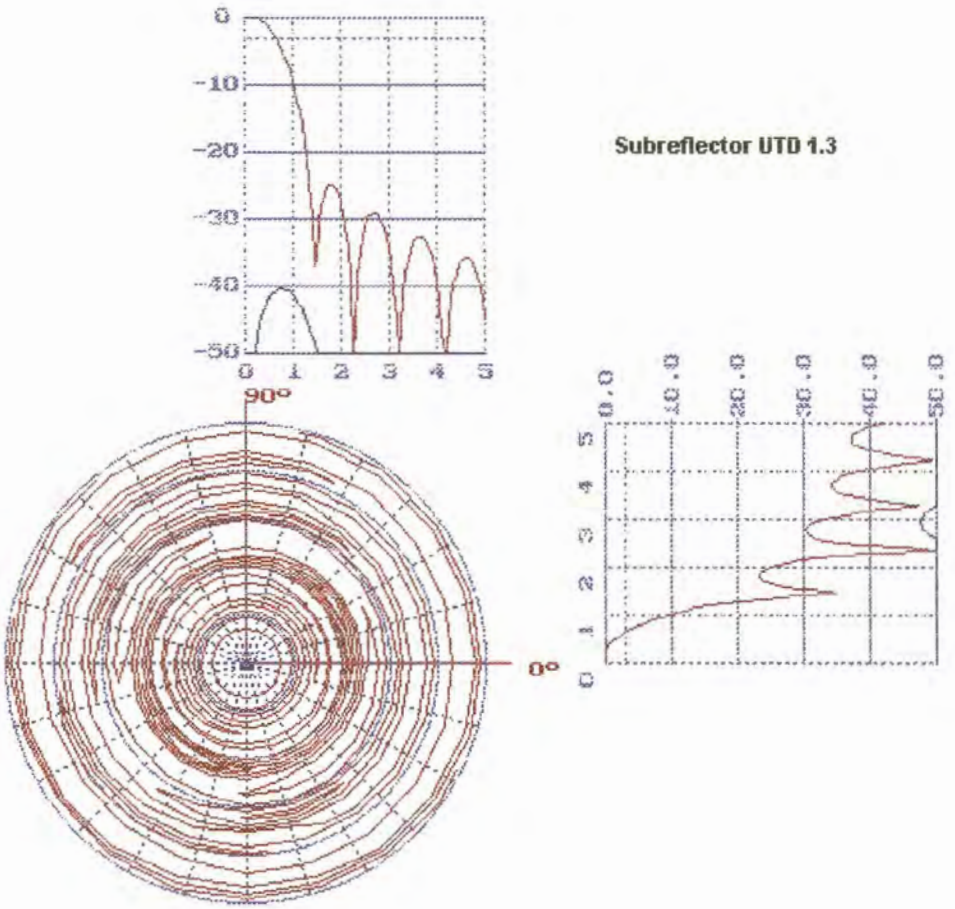

Figure 8(a). Calculated far-field for a dual offset reflector antenna showing the subreflector edge diffraction effect for an oversized subreflector.

Figure 8 shows the effect of oversizing the subreflector to minimize the subreflector edge diffraction effects on the radiation pattern of the dual offset reflector antenna. In *Figure 8(b) no oversizing on the subreflector is made. A significant effect can be seen* in the radiation pattern especially associated with the cross polarization levels. In Figure 8(a) a factor of 1.15 or 15% oversizing is used.

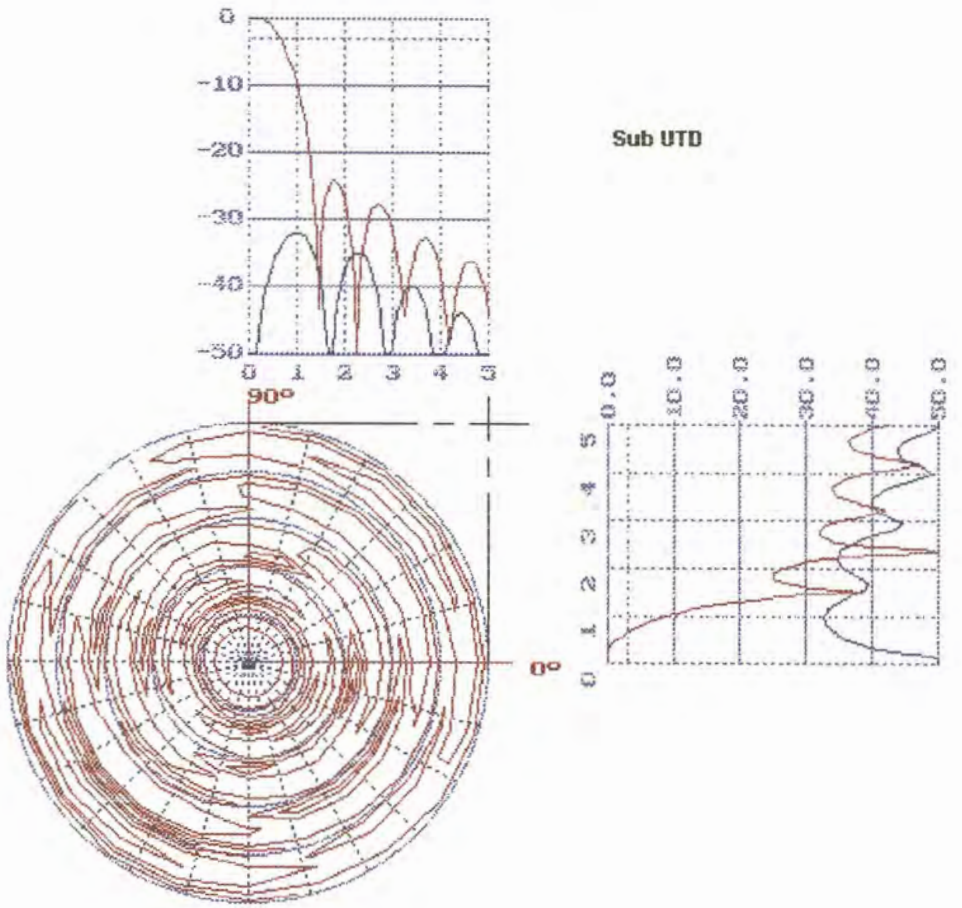

Figure 8(b). Subreflector edge diffraction effect on the radiation pattern of a dual offset reflector antenna.

The Jacobi-Bessel series expansion method is very fast and efficient for well focussed reflector antennas because of the dominant Airy type behaviour in the vicinity of the boresight direction. This method did not give accurate results when the shaping of the reflector surfaces causes severe defocussing of the reflector, even when many terms were used in the series. For a lot of terms in the series the Jacobi-Bessel method also gets inefficient. A p-series technique (sometimes called the pseudo sampling technique)

exploiting the efficiency of the FFT was eventually used [8]. This involves using (2.77) and sampling the surface current density distribution to calculate the far-field at the required vectors. The sampling interval determines the u-v space sampling interval as shown in Figure 9 where

$$\Delta k_x \Delta k_y = \frac{2k_1}{N_x}\frac{2k_1}{N_y} = \frac{4\pi^2}{N_x \Delta x N_y \Delta y} \quad (2.92)$$

The sampling intervals have to be chosen keeping the k-space band limit in mind. To get the u-v space data at any other interval a resampling technique described by Papoulis [16] is used.

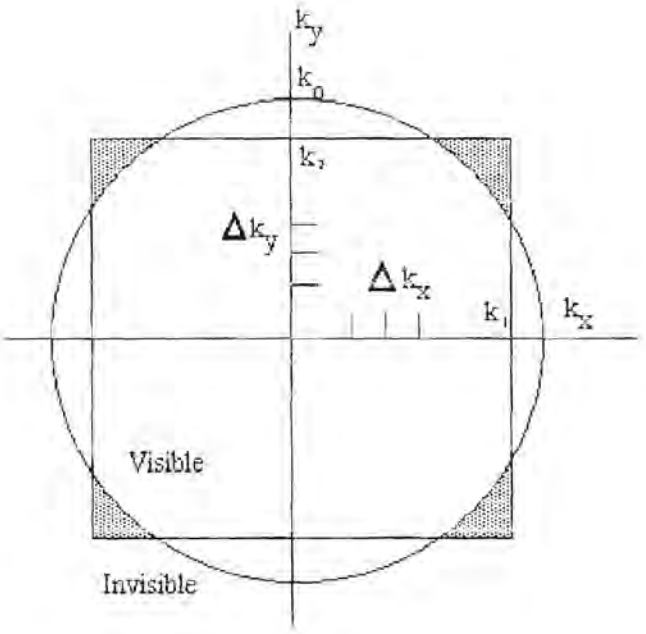

Figure 9. Diagram to determine sampling interval effect on the visible k-space spectrum.

2.3.3. The Gaussian beam technique

A closed form asymptotic solution was developed at the ElectroScience Laboratory, OSU by Chou and Pathak [4] for predicting the reflection and diffraction of an arbitrary Gaussian beam (GB) by a general finite curved surface. This solution can be seen as analogous to the ray solution based on the uniform asymptotic theory of diffraction (UAT) but the uniform solution for the GB's remain valid in the regions of ray caustics. All PO and aperture integration techniques become costly in terms of time and memory requirements and inefficient for very large antennas because the integration has to be performed numerically. The GB method avoids this integration because the GB reflection and diffraction solution are acquired in closed form and offer a significant advantage in terms of the synthesis time required for very large antennas. Analyses were made on synthesized surfaces and a version of the synthesis code using the GB technique was reported on in [5].

The general astigmatic GB is a projection in real space of a ray field with the source located in complex space. In real space the GB is a field whose amplitude tapers away exponentially with a Gaussian taper in the transverse direction to the propagation direction. Numerical results have shown that a GB is produced in the paraxial region upon reflection from an infinite surface of an incident GB and in particular the reflected field of a GB incident on a parabolic surface behaves as a GB within the paraxial region. The reflection of a GB from an infinite three dimensional surface will be discussed briefly. A method to do an expansion of a feed radiation pattern in terms of GB's will be shown and some results demonstrating the use of the GB method to synthesize an offset parabolic reflector will be shown.

A rotationally symmetric scalar GB is used for the basis function and can be written as

$$U(x_g, y_g, z_g) = \frac{jb}{z_i^{in} + jb} e^{-jk\left[z_g + \frac{1}{2}\frac{z_g}{z_g^2 + b^2}\left(x_g^2 + y_g^2\right)\right]} e^{-\frac{1}{2}kb\left[\frac{\left(x_g^2 + y_g^2\right)}{z_g^2 + b^2}\right]} \qquad (2.93)$$

where the coordinate system of the beam aligns with the beam axis in the z_g direction. In Equation (2.93) the variable b is the GB waist. In the far-field form of the GB (z_g >>b) Equation (2.93) can be written in spherical coordinates as

$$U(\bar{r}_g) = \frac{jb}{r_g} e^{-jk\left[z_g + \frac{1}{2}\frac{z_g}{z_g^2+b^2}\left(x_g^2+y_g^2\right)\right]} e^{-\frac{1}{2}kb\tan^3\theta_g} . \quad (2.94)$$

The GB in the far-field form also has a Gaussian taper in angle everywhere in the paraxial region with an angular beamwidth defined as the 1/e angular width of the beam in the far-zone. This is given by

$$BW_\theta = 2\sqrt{\frac{2}{kb}} . \quad (2.95)$$

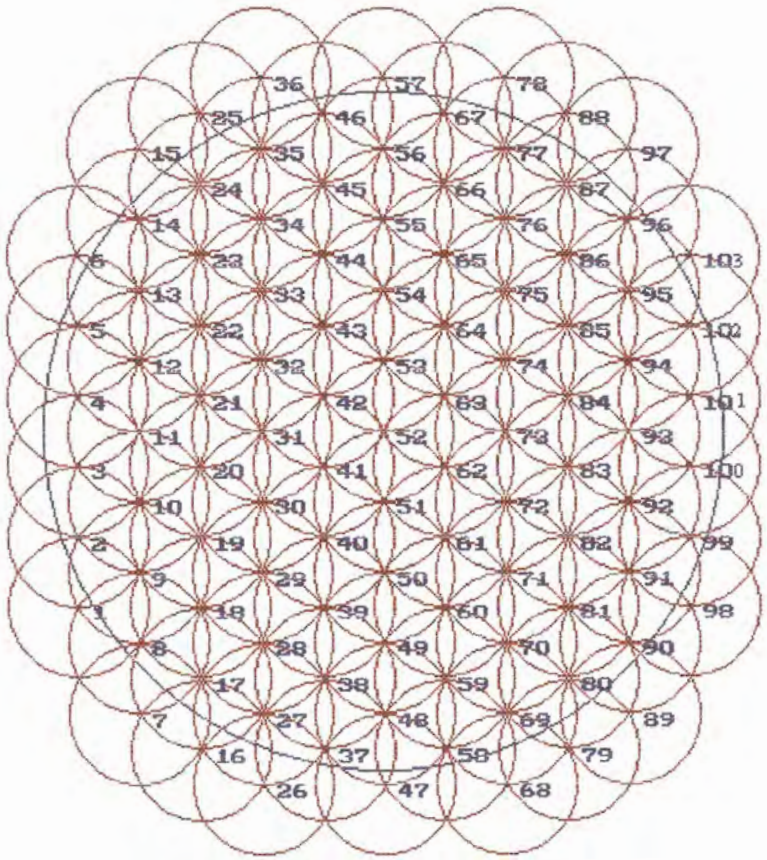

Figure 10. Mapping of GB's onto the solid angle subtended at the feed by the reflector rim.

Thus the beam waist is the width of the beam at the origin and varies as $\sqrt{b}$ and the angular beamwidth varies as $\sqrt{\frac{1}{b}}$.

The field expansion can be made in terms of the electric or magnetic fields. The magnetic far-field radiated by the feed antenna is denoted by

$$\overline{H}(\overline{r}_f) = \frac{e^{-jkr_f}}{r_f}\left\{\hat{\theta}_f F_\theta(\hat{r}_f) + \hat{\phi}_f F_\phi(\hat{r}_f)\right\} \tag{2.96}$$

The magnetic field of a feed pattern can be written in terms of a set of rotated GB's as

$$\overline{H}(\overline{r}_f) \cong \sum_{m=1}^{M} C_m \overline{H}_m^i(\overline{r}_i^m) \tag{2.97}$$

where C_m the expansion coefficient of the m^{th} GB basis function $\overline{H}_m^i$ denoted by

$$\overline{H}_m^i\left(\overline{r}_i^m\right) = \overline{e}_m \frac{jb}{z_i^m + jb} e^{-jk\left[z_i^m + \frac{1}{2}\frac{(x_i^m)^2 + (y_i^m)^2}{z_i^m + jb}\right]} \tag{2.98}$$

with the polarization vector $\overline{e}_m$ chosen to be

$$\overline{e}_m = \left[\hat{\theta}_f F_\theta\left(\hat{r}_f\right) + \hat{\phi}_f F_\phi\left(\hat{r}_f\right)\right] \tag{2.99}$$

In this form the GB is normalized to the feed pattern in the beam axis direction. Figure 10 shows a representation of the feed pattern expanded in a set of GB's in using the beamwaist values as indicated . Figure 11 shows the real coordinate system used for a few launched beams and the real part of the saddle point for a 10° offset angle from boresight going around in 36° increments.

The reflection of a three-dimensional Gaussian beam from a slowly varying surface will be summarized. This also follows [4] where a full treatment of GB reflection from a double curved surface containing an edge is made using an asymptotic technique on the PO radiation integral of the scattered GB.

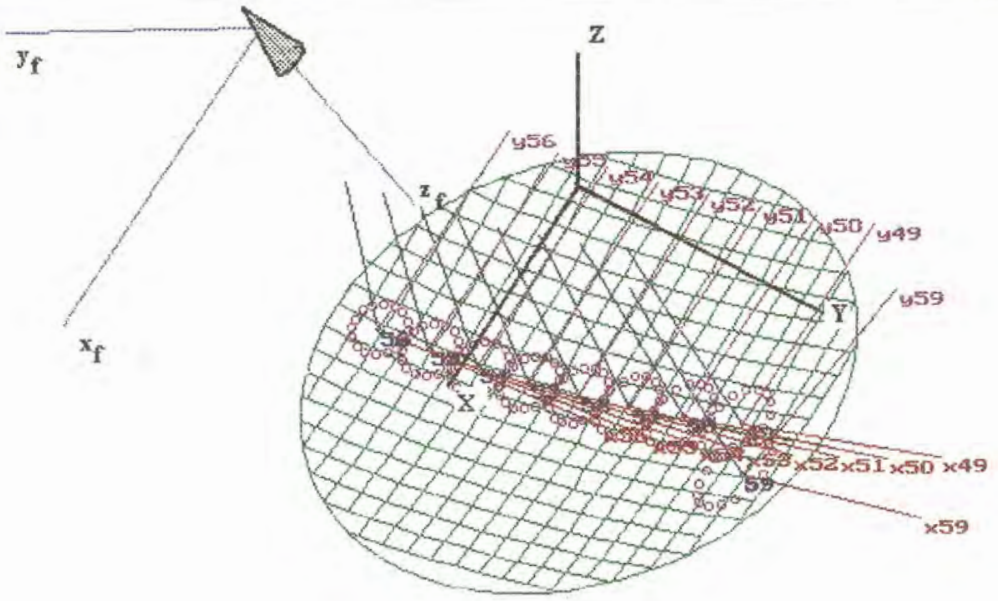

Figure 11. Samples of coordinate systems used for launched beams showing location of the real part of the saddle point (magenta circles) for a 10° offset angle from boresight going around in 36° increments.

It is assumed that the scattering surface may be locally approximated by a paraboloid in the neighborhood of the reflection point where the beam axis intersects the surface. A local coordinate system is defined with the reflection point at its origin and with the local parabolic surface defined as

$$z = -\frac{1}{2}\left[\frac{x^2}{R_1} + \frac{y^2}{R_2}\right] \tag{2.100}$$

where R_1 and R_2 are the local principal radii of curvature in the $\hat{x}$ and $\hat{y}$ directions respectively. In [4] its is assumed that the surface contains an edge where the plane containing the edge may or may not be parallel to the surface normal at the beam reflection point.

The geometry for the local i-coordinate system is shown in Figure 11. The incident magnetic field is given by

$$\overline{H}^{i}(\overline{r}_i) = \overline{H}^{i}(0)\sqrt{\frac{Det\left[Q^{i}(z_i)\right]}{Det\left[Q^{i}(0)\right]}}e^{-jk\left[z_i+\frac{1}{2}[\xi_i]^T Q^{i}(z_i)[\xi_i]\right]}; \quad [\xi_i] = \begin{bmatrix} x_i \\ y_i \end{bmatrix}$$

where $\overline{H}(0)$ is the incident magnetic field at the origin O.

The curvature matrix Q^i is complex for a GB and is given by

$$Q^{i}(O) = \begin{bmatrix} Q^{i}_{11} & Q^{i}_{12} \\ Q^{i}_{21} & Q^{i}_{22} \end{bmatrix} \tag{2.102}$$

and the GB propagation rule is given by

$$\left[Q^{i}(z_i)\right]^{-1} = \left[Q^{i}(0)\right]^{-1} + z_i I \tag{2.103}$$

where I is the unit matrix.

The transformation relating the parabolic surface coordinates to the incident GB coordinates is given by

$$\begin{bmatrix} x_i \\ y_i \\ z_i \end{bmatrix} = \begin{bmatrix} c_{11} & c_{12} & c_{13} \\ c_{21} & c_{22} & c_{23} \\ c_{31} & c_{32} & c_{33} \end{bmatrix}\begin{bmatrix} x \\ y \\ z \end{bmatrix}. \tag{2.104}$$

Depending on the terms in the curvature matrix the GB can be a rotationally symmetric - , elliptical - or a general astigmatic GB. The incident GB strongly illuminates the reflecting surface in the spot area around O. The PO radiation integral for the electric and magnetic scattered fields from the surface are respectively given by

$$\overline{E}^{s}(\overline{r}) \cong \frac{jkZ_0}{4\pi}\iint_S \left[\hat{R} \times \hat{R} \times \overline{J}_{eq}(\overline{r}')\right]\frac{e^{-jkR}}{R}\,dS \tag{2.105}$$

$$\overline{H}^{s}(\overline{r}) \cong \frac{jk}{4\pi}\iint_S \left[\hat{R} \times \overline{J}_{eq}(\overline{r}')\right]\frac{e^{-jkR}}{R}\,dS \tag{2.106}$$

where S denotes the part of the surface which is directly illuminated by the GB and Z_0 is the impedance of free space. R is given by the usual paraxial approximation namely

$$\overline{R} = \overline{r} - \overline{r}'; \qquad R = |\overline{R}| \tag{2.107}$$

with

$$\overline{r} = x\hat{x} + y\hat{y} + z\hat{z} \quad and \quad \overline{r}' = x'\,\hat{x} + y'\,\hat{y} + z'\,\hat{z} \tag{2.108}$$

where $\overline{r}$ is the vector to the observation point and $\overline{r}'$ the vector to any point on the surface.

The PO base equivalent current is given by the expression

$$\bar{J}_{eq}(\bar{r}') = 2\hat{n} \times \bar{H}^i(\bar{r}') \tag{2.109}$$

where the unit vector normal to the surface is given by

$$\hat{n} = \frac{\hat{z} + \hat{x}\frac{x'}{R_1} + \hat{y}\frac{y'}{R_2}}{\sqrt{1 + \left(\frac{x'}{R_1}\right)^2 + \left(\frac{y'}{R_2}\right)^2}} \tag{2.110}$$

The integration is difficult to perform over a surface coordinate system and the surface Jacobian is used to obtain the integration over a projection on the z=0 plane. The surface Jacobian is given by

$$dS' = \sqrt{1 + \left(\frac{x'}{R_1}\right)^2 + \left(\frac{y'}{R_2}\right)^2}\, dx'\, dy' \tag{2.111}$$

and the differential current element can be written as

$$\bar{J}_{eq}(\bar{r}')dS' = 2\left[\hat{z} + \hat{x}\frac{x'}{R_1} + \hat{y}\frac{y'}{R_2}\right] \times \bar{H}^i(\bar{r}')dx'\, dy' \tag{2.112}$$

where it follows from Equation (2.109) that the incident magnetic field in the neighborhood of the reflection point can be approximated by

$$\bar{H}^i(\bar{r}') \cong \bar{H}^i_m(\bar{r}')e^{jkq(r')} \tag{2.113}$$

with

$$\bar{H}^i_m(\bar{r}') = \bar{H}^i(0)\sqrt{\frac{Det\left[Q^i(z_i)\right]}{Det\left[Q^i(0)\right]}} \tag{2.114}$$

and

$$q(\bar{r}') = -\left[z_i + \frac{1}{2}\left(Q^i_{11}x_i^2 + 2Q^i_{12}x_iy_i + Q^i_{22}y_i^2\right)\right] \tag{2.115}$$

The scattered electric and magnetic field can now be written as

$$\bar{E}^s(\bar{r}) \cong \frac{jkZ_0}{4\pi}\iint_S 2\left[\hat{R} \times \hat{R} \times \left(\hat{z} + \hat{x}\frac{x'}{R_1} + \hat{y}\frac{y'}{R_2}\right) \times \bar{H}^i_m(\bar{r}')\right]\frac{e^{-jk[R - q(\bar{r}')]}}{R}\, dS$$

and

$$\bar{H}^s(\bar{r}) \cong \frac{jk}{4\pi}\iint_S \left[\hat{R} \times \left(\hat{z} + \hat{x}\frac{x'}{R_1} + \hat{y}\frac{y'}{R_2}\right) \times \bar{H}^i_m(\bar{r}')\right]\frac{e^{-jk[R - q(\bar{r}')]}}{R}\, dS \tag{2.117}$$

Equation (2.116) and (2.117) have the same general form as

$$\bar{P}^s(\bar{r}) = \iint_S \bar{F}(x', y')e^{jkf(x', y')}dx'\, dy' \tag{2.118}$$

where f(x',y') denotes the phase term of the integrand and is defined by

$$f(x', y') = -R + q(x', y') \tag{2.119}$$

$\overline{P}^s(\bar{r})$ represents either the scattered electric or the scattered magnetic field.

In this analysis the observer can be in the Fresnel region of the reflecting surface. In the Fresnel region R can be expanded in terms of a Taylor series about the GB reflection point O retaining up to the quadratic terms in x' and y'. Using the approximation the phase term f(x',y') can be expressed as

$$f(x',y') = -r - a_0x'^2 + b_0x' - a_1y'^2 + b_1y' - 2cx'y' \quad (2.120)$$

where the coefficients a_0, a_1, b_0, b_1 and c are defined as

$$a_0 = \frac{1}{2}\left\{\frac{1}{R_1}\left(\frac{z}{r} - c_{33}\right) + \frac{1}{r}\left(1 - \frac{x^2}{r^2}\right) + c_{11}^2Q_{11}^i + c_{21}^2Q_{22}^i + 2c_{11}c_{21}Q_{12}^i\right\} \quad (2.121)$$

$$b_0 = \left(\frac{x}{r} - c_{31}\right) \quad (2.122)$$

$$a_1 = \frac{1}{2}\left\{\frac{1}{R_2}\left(\frac{z}{r} - c_{33}\right) + \frac{1}{r}\left(1 - \frac{y^2}{r^2}\right) + c_{12}^2Q_{11}^i + c_{22}^2Q_{22}^i + 2c_{11}c_{21}Q_{12}^i\right\} \quad (2.123)$$

$$b_1 = \left(\frac{y}{r} - c_{32}\right) \quad (2.124)$$

$$c = \frac{1}{2}\left\{c_{11}c_{12}Q_{11}^i + c_{21}c_{22}Q_{22}^i + \left(c_{11}c_{22} + c_{21}c_{12}\right)Q_{12}^i - \frac{xy}{r^3}\right\}. \quad (2.125)$$

Note that f(x',y') can be written as

$$f(x',y') = f(x_s, y_s) - a_0(x'-x_s)^2 - a_1(y'-y_s)^2 - 2c(x'-x_s)(y'-y_s) \quad (2.126)$$

where

$$x_s = \frac{a_1b_0 - b_1c}{a\left(a_0a_1 - c^2\right)} \quad (2.127)$$

$$y_s = \frac{a_0b_1 - b_0c}{a\left(a_0a_1 - c^2\right)} \quad (2.128)$$

and

$$f(x_s, y_s) = -r + \frac{a_1b_0^2 + a_0b_1^2 - 2b_1b_0c}{4\left(a_0a_1 - c^2\right)}. \quad (2.129)$$

It is shown in [4] that (x_s ,y_s) constitutes the complex stationary phase point in (x',y') and f (x_s ,y_s) is the value of the complex exponential term in the integrand of (2.118) when it is evaluated at this stationary point. For large k an asymptotic approximation

for (2.118) is derived in [4] leading to a closed form result for the double integral. In [4] the total reflected field for the GB is derived in the presence of an edge and is given by

$$\overline{P}^{s}(\bar{r}) \cong \overline{P}_r(\bar{r}) \cdot T(S_a) + \overline{P}_d(\bar{r}) \tag{2.130}$$

where

$$\overline{P}_r(\bar{r}) \equiv \overline{F}_x(x'_{s1}) \sqrt{\frac{-2\pi}{jkf''(x'_{s1})}} e^{jkf_x(x'_{s1})} \tag{2.131}$$

$$T(S_a) \equiv 1 - \frac{1}{2}\left[1 - erf(S_a)\right] + \frac{e^{-S_a^2}}{2\sqrt{\pi}S_a} \tag{2.132}$$

$$\overline{P}_d(\bar{r}) \equiv \overline{F}_x(x_e) \frac{1}{jkf'_x(x_e)} e^{jkf_x(x_e)} \tag{2.133}$$

$\overline{P}_r(\bar{r})$ is the contribution from the saddle point which is the asymptotic contribution from the integral without the edge so that $\overline{P}_r(\bar{r})$ is referred to as the reflected field of the GB. The other term $\overline{P}_d(\bar{r})$ is the contribution from the edge and is determined by the complex distance of the edge point from the saddle point so that $\overline{P}_d(\bar{r})$ is referred to as the edge diffracted field. T is the transition function and depends on the complex phase difference of between the saddle point and the edge point.

2.4. Surface expansion in terms of the Modified Jacobi polynomials

The surface of the main reflector is given by

$$z(t, \psi) = \sum_{n} \sum_{m} (C_{nm} \cos n\psi + D_{nm} \sin n\psi) F_m^n(t) \qquad (2.134)$$

where C_{nm} and D_{nm} are the expansion coefficients and $F_m^n(t)$ are the modified Jacobi polynomials. These polynomials are related to the Zernike circle polynomials that are often used in the study of optical aberrations [11]. Combinations of the modified Jacobi polynomials and the Fourier harmonics form a complete set of orthogonal basis functions in the unit circle. Figure 12 shows a projection of the unit area used for the surface series expansion for the subreflector.

The main reflector surface expansion coefficients and those of the subreflector surface are adjusted during synthesis. The synthesis process produces a continuous surface with continuous first and second derivatives. The first two terms of the infinite set of Fourier transforms will be used and have been shown to be sufficient when the synthesized pattern for the CONUS beam case was compared using an accurate PO reflector analysis software package developed at OSU [7]. This method has the disadvantage that the far-field spectrum is calculated in intervals determined by the sampling interval of the surface current density. To find the gain at a point not falling on the interval resampling of the u-v space must be performed. The far-field template for different geographical regions of coverage can then be set up and compared.

Following [11] the main and the subreflector surfaces can be described by a series expansion in terms of the modified Jacobi polynomials. The aperture is defined by the superquadric function:

$$\left[\left(\frac{x}{a}\right)^2\right]^v + \left[\left(\frac{y}{b}\right)^2\right]^v = 1 \qquad (2.135)$$

where a and b are the semi-major axes of the projected aperture.

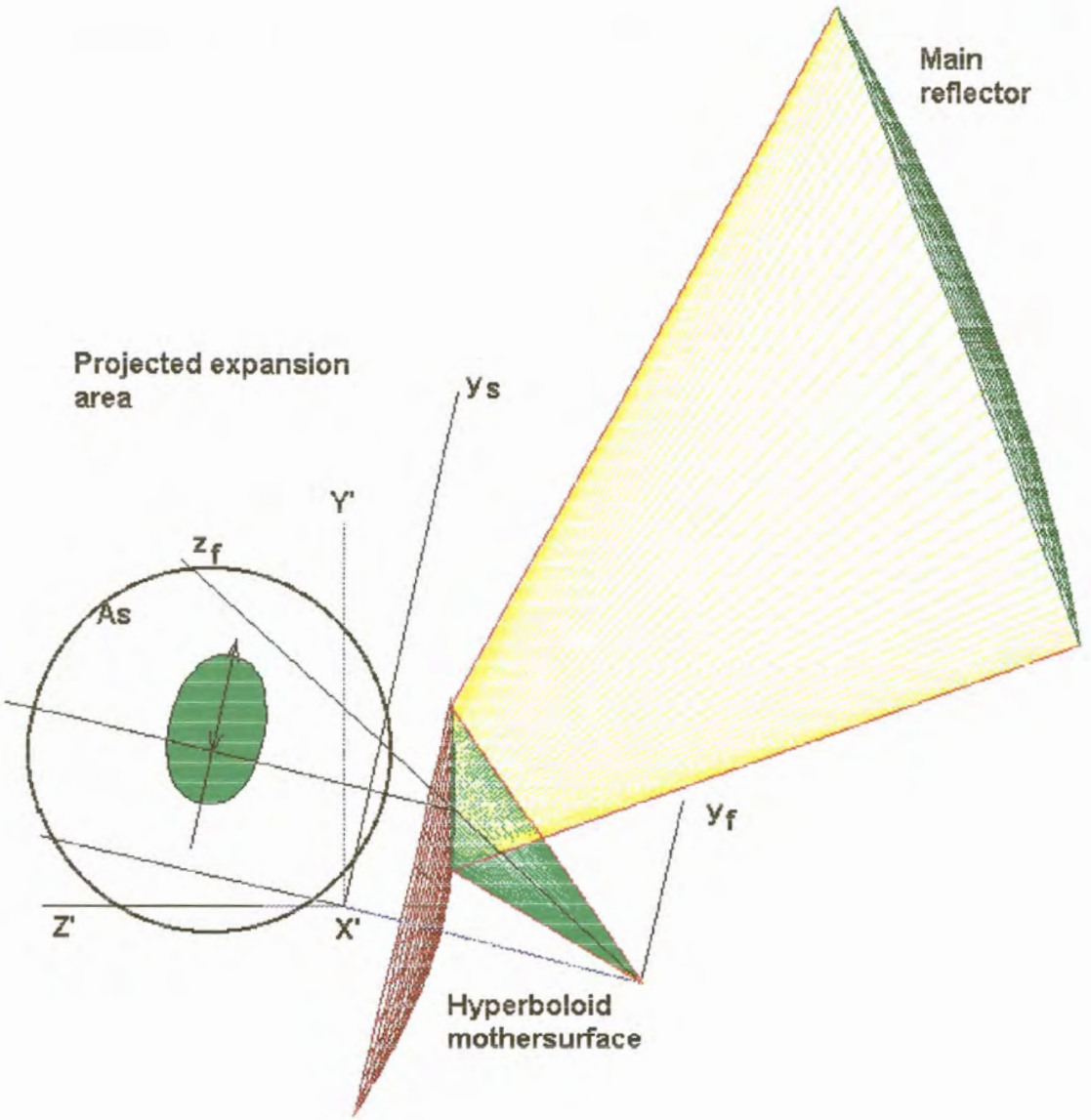

Figure 12. Projection showing unit circle used for surface series expansion of the subreflector in terms of the modified Jacobi polynomials.

These aperture functions can be used to described apertures with circular, elliptical and rounded corner boundaries using the parametric representation

$$x'(t, \psi) = at \cos\psi \cdot r(\psi) \text{ , and} \quad (2.136)$$

$$y'(t, \psi) = at \sin\psi \cdot r(\psi) \quad (2.137)$$

where r(ψ) is given by

$$r(\psi) = \frac{1}{\left(|\cos\psi|^{2v} + |\sin\psi|^{2v}\right)^{1/2v}} \quad (2.138)$$

The superquadric boundary is exactly represented by the parametric curve t=1. This is important when diffraction from the edge of the reflector surfaces are calculated using UTD.

2.5. Verification of the accuracy of the developed codes

2.5.1. The p-series method

Several tests were performed to establish the accuracy of the reflector synthesis code. At The Ohio State University a very accurate code that uses physical optics on both the main and the subreflector was developed by Lee and Ruddick [7]. This code was used to compare the beam synthesis accuracy for a CONUS beam example. The synthesized surfaces and feed illumination functions were used in the OSU NECREF Version 3.0 code. Comparisons were also made with the Gaussian beam technique for defocussed reflector antennas. These radiation patterns were overlayed to determine the wide angle performance of the code. Excellent agreement is obtained up to more than 30° off boresight for a sampling interval of 0.9 wavelengths even though only two terms of the p-series are used.

Figure 13(a) and (b) show the co-polarized and cross polarized radiation pattern for a CONUS beam synthesized with the developed code. The same synthesized surfaces were analyzed using the OSU NECREF Version 3.0 code and the co-polarized and cross polarized radiation pattern are shown in Figure 14 (a) and (b) for comparison.

The code shows excellent agreement in the main beam area for both the co-polarized field In the cross-polarized field there is an expected difference but the field shape and maximum cross-polarized signal level in the main beam region shows good agreement. These results establish confidence in the accuracy of the far-field prediction of the diffraction synthesis software.

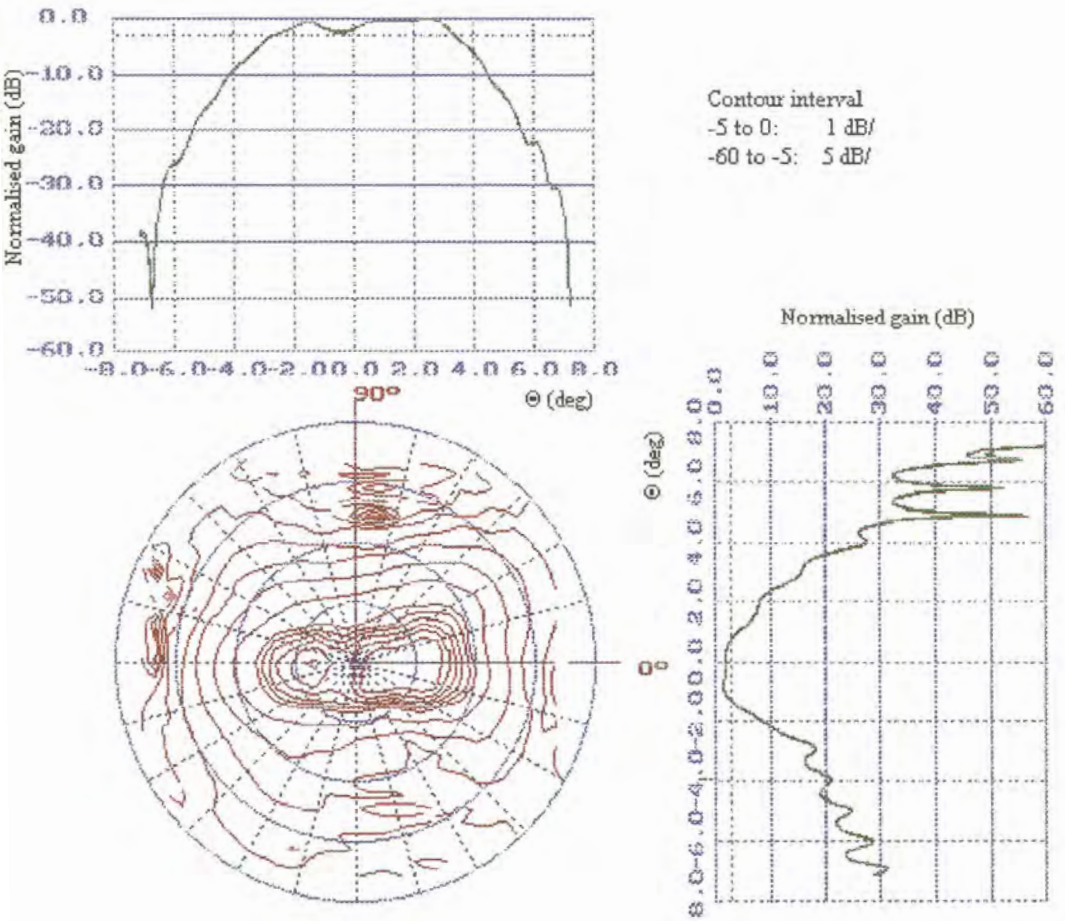

Figure 13 (a). Co-polarized far-field calculated using the developed p-series code. The main plane radiation pattern cuts of Figure 14 (a) are added in green for comparison.

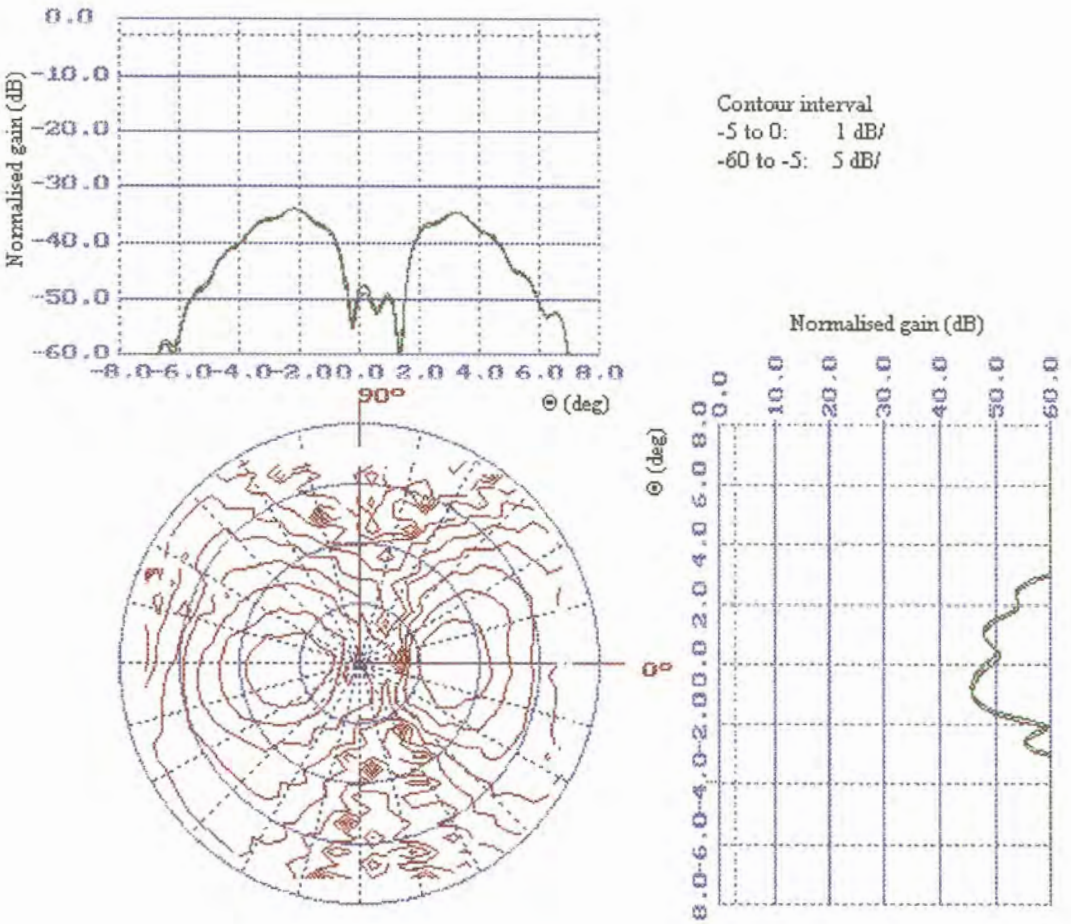

Figure 13 (b). Cross-polarized far-field calculated using the developed p-series code. The main plane radiation pattern cuts of Figure 14 (b) are added in green for comparison.

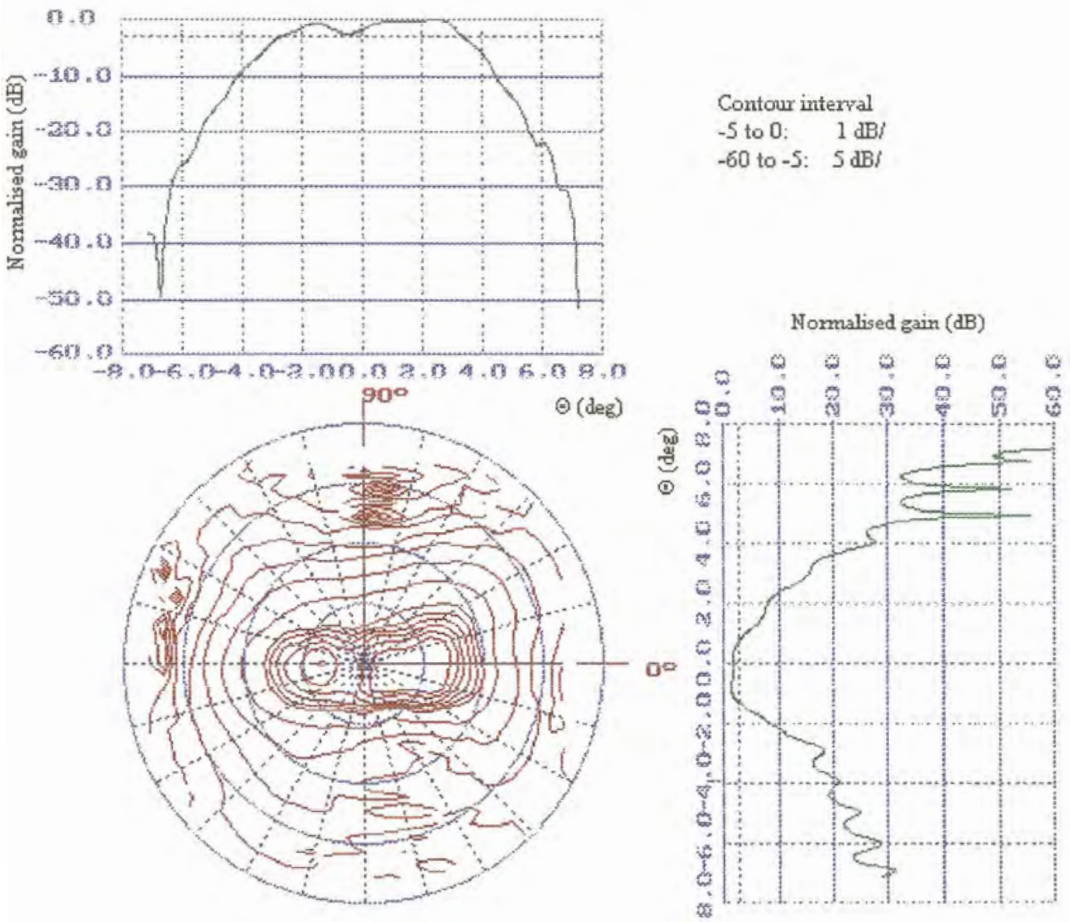

Figure 14 (a). Co-polarized far-field calculated using OSU NECREF Version 3.0 code [11]

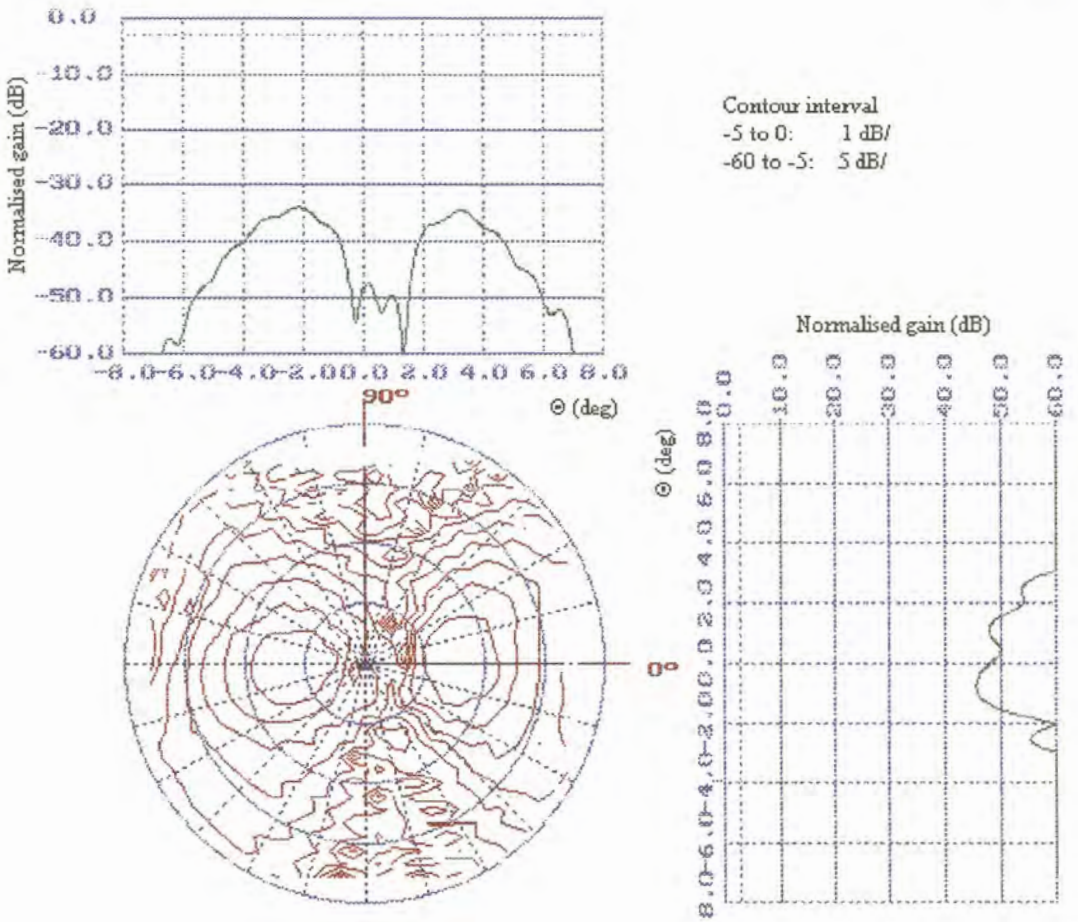

Figure 14 (b). Cross-polarized far-field calculated using OSU NECREF Version 3.0 code [11]

2.5.2. The Gaussian beam technique

The synthesis procedure using the GB method is implemented using only the reflected GB component because the edge contributions are small in the narrow angular extend over which the synthesis will be performed. In the latest implementation only single offset examples are synthesized but the feed-subreflector combination radiation pattern can be calculated using a GB expansion such that one can do main reflector synthesis. The significant speed advantage makes this a very worthwhile technique to pursue, although this has not been done as part of the work reported on in this dissertation. Figure 15 (a) shows the far-field calculated using PO and should be compared with the calculation using the GB technique in Figure 15(b).

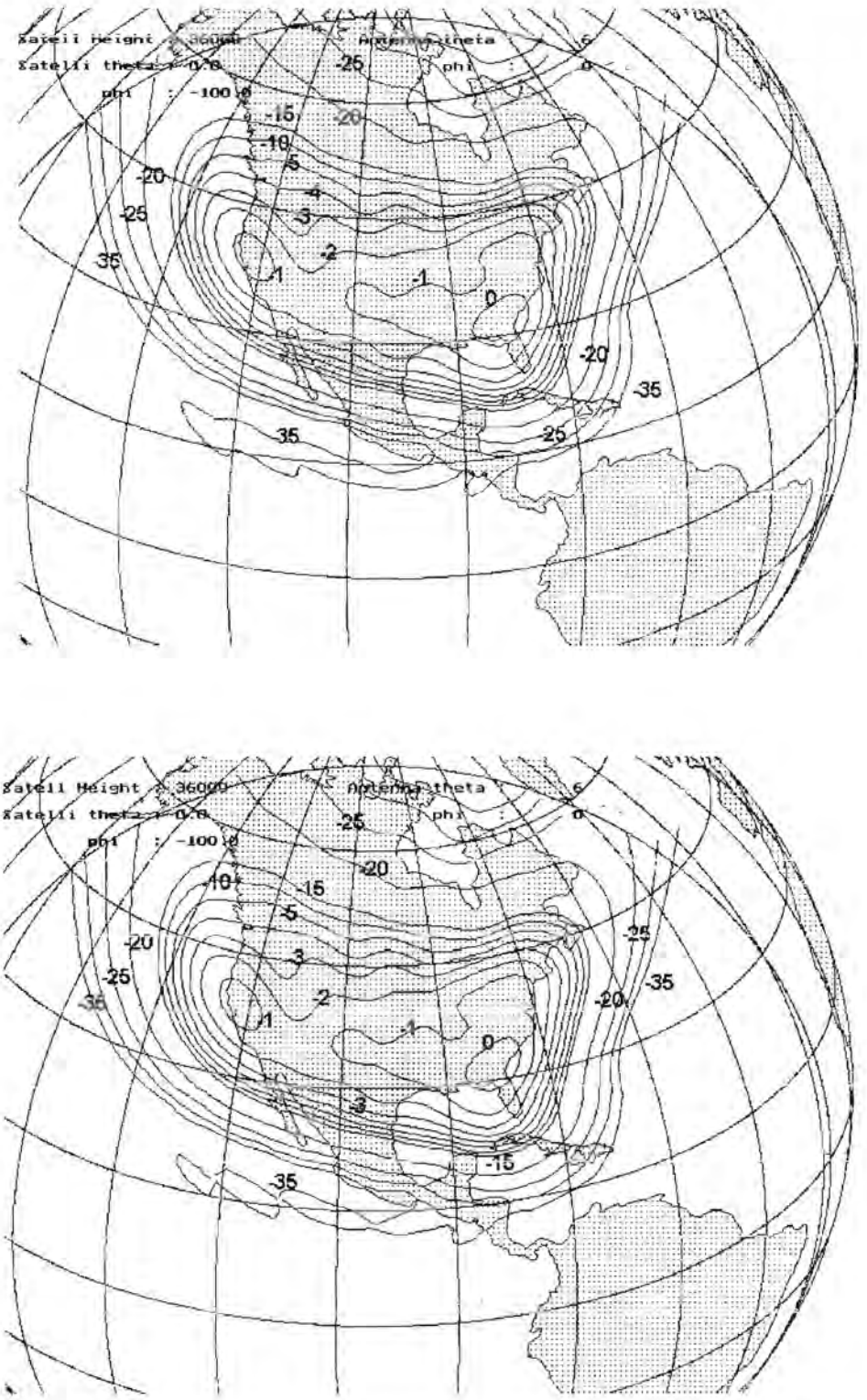

Figure 15 (a) and (b). Far-field calculated using PO and the GB technique for a front fed offset parabolic reflector shaped using the modified Jacobi polynomial expansion.

2.6. Calculating the antenna footprint

The various radiation footprints of the antennas are calculated by using 4 coordinate systems namely the antenna-, satellite-, geocentric- and observer coordinate systems. Translation and rotation of the coordinate systems are handled using matrix operations where the matrix elements are derived from spherical trigonometry. The contour algorithm is implemented by calculating the points where vectors in the antenna coordinate system intersect the geocentric surface and using linear interpolation to draw the required contour levels on each quadrilateral. This is described in [27]. Figure 16 shows how the u-v space test grid maps onto the geocentric surface for the case of the CONUS beam synthesis. The values of the illuminating electric field are calculated on the corner points of each quadrangle taking into account the range spread factor. These values are used in a linear interpolating algorithm that draws the contours at preselected intervals between preselected bounds.

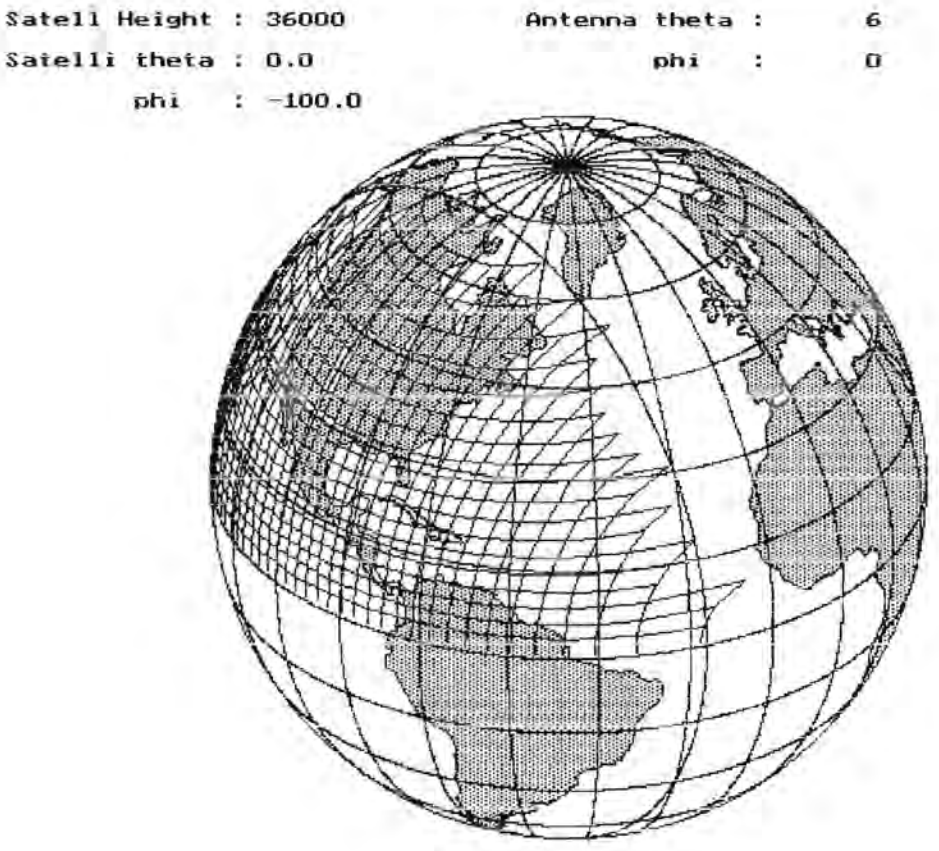

Figure 16. The u-v-space test grid is shown mapped onto geocentric surface. These test points are used to calculate the cost function during synthesis.

Chapter 3: Optimization of the contour beam gain cost function

The method of optimization of the far-field by changing the reflector surfaces of the DOSR will be dealt with in Chapter 3. The calculation of the cost function, that is the function that gets minimized during synthesis, is described in paragraph 3.1. The global and local search techniques used to minimize this function are introduced in paragraph 3.2. In this paragraph the advantages and disadvantages of global and local search techniques for this application are also discussed. The two methods used to implement the global and local search are the genetic algorithm and the steepest gradient solver. The steepest gradient solver is implemented following [11] but the genetic algorithm has been implemented for the first time in this particular reflector synthesis problem. Both were used individually in some beam syntheses and also used in combination in other syntheses. The synthesis example shown in paragraph 3.3 is an example where the genetic algoritm is used to find an approximate solution and the steepest gradient solver is then used to 'smooth' the contour coverage.

3.1. Cost function

In the diffraction synthesis procedure the objective is to minimize a cost function of the form

$$\Psi = \sum_{j=1}^{M} \left| G_j - GD_j \right|^2 \tag{3.1}$$

where G_j is the actual antenna gain in the j direction and GD_j the desired gain. The actual gain is found from the calculation of the far-field using the methods discussed in Chapter 2 at a specific vector using Equation (2.67) and (2.75) for the p-series method. The desired gain is found from a u-v-space gain template described in paragraph 3.3. To search for this minimum several local and global optimization techniques were examined during the course of this study.

3.2. Optimization methods

The distinction between local and global search techniques is that the local techniques produce results that are dependent on the starting point or initial guess while global methods are largely independent of the initial conditions. In addition, local techniques tend to be tightly coupled to the solution domain. This tight coupling enables the local methods to take advantage of the solution space characteristics resulting in relatively fast convergence to a local maximum [17].

The global techniques, on the other hand, are largely independent of the solution domain. Global techniques are much better at dealing with solution spaces having discontinuous or non-differentiable cost functions, constrained parameters, and/or a large number of dimensions with many potential local maxima.

The genetic algorithm (GA) is classified as a Global or Stochastic technique [18]. GA's are much less likely to get stuck on local minimums. The GA is robust and has a better chance of yielding the global optimum although no optimization technique can guarantee this [11]. The disadvantage to the global method's general independence from the solution space is that it does not use information on local solution space characteristics such as gradients during the search process resulting in generally slower convergence than the local techniques.

3.2.1. The Steepest Gradient Solver

A steepest gradient solver was used to minimize the cost function Ψ in Equation (3.1). When Ψ is minimized the mean square difference between the gain desired and the gain achieved is minimized.

Following [20] the set of surface expansion coefficients CD_i that minimizes Ψ in Equation (3.1) were found by considering

$$\begin{bmatrix} CD_1(k+1) \\ CD_2(k+1) \\ \vdots \\ CD_N(k+1) \end{bmatrix} = \begin{bmatrix} CD_1(k) \\ CD_2(k) \\ \vdots \\ CD_N(k) \end{bmatrix} - \mu \begin{bmatrix} \frac{\partial \psi}{\partial CD_1}\Big|_{CD_1 = CD_1(k)} \\ \frac{\partial \psi}{\partial CD_2}\Big|_{CD_2 = CD_2(k)} \\ \vdots \\ \frac{\partial \psi}{\partial CD_N}\Big|_{CD_N = CD_N(k)} \end{bmatrix} \tag{3.2}$$

where μ is a scale factor. By properly choosing μ , Ψ is minimized since the gradient term on the right hand side in Equation (3.2) gives the direction in the M-dimensional space that results in the greatest increase in Ψ. In practice μ is initially set equal to the inverse of the magnitude of the gradient in Equation (3.2) and is reduced by a factor of 0.9 each time the cost function increases.

The obvious disadvantage of the steepest gradient solver is the required differentiation of the cost function in terms of the surface expansion coefficients. This was done numerically such that a very fast algorithm is needed for the calculation of far-field at the desired vectors or the synthesis process would be extremely slow. During the synthesis process the steepest gradient method was used after the genetic algorithm found a relatively good solution. The final 'smoothing' of the contours over the service area is done using a steepest gradient solver.

3.2.2. The Genetic Algorithm Solver

A GA is a stochastic search procedures modeled on the Darwinian concepts of natural selection and evolution. A set or population of potential solutions is caused to evolve toward a global optimal solution. Simple recombination and mutation of existing solution characteristics. Evolution is the result of selective pressure exerted by fitness based selection [18].

When implementing a GA, a population set of trial solutions is first set up. The chromosome of each solution is consists of a string of genes each coded to form a trial solution vector. Each gene represents a parameter of the fitness. Chromosomes can be entirely encoded (usually binary), floating point or mixed binary and floating point. The following are examples of a chromosomes containing 6 genes in binary coded, and 7 genes in floating point vector form respectively.

{101001,01110,110101,011010,011,10101}

{425,-0.179,120,-537,4652,11.433,0.067}

A generation is a successively created population or a GA iteration. Each current generation contains parents or members of the current generation. A child is member of the generation following on the current generation. To each parent a positive fitness

number is assigned representing a measure of goodness. A reproduction scheme is implemented where genetic material of pairs chromosomes is mixed. This can be performed at crossover points randomly generated for each gene. A mutation is performed on the population where a random changeover of bits (in the case of a binary encoding scheme) is made throughout the population. After this a fitness evaluation is performed on each member of the next generation and a ranking of the total population is made. Based on the ranking some members of the population are discarded. This process is repeated until a cost function level is achieved or a certain number of iterations is exceeded. Certain variations on the basic GA can be implemented, for example tournament selection, where "N" individuals at randomly selected from the population and the individual with highest fitness value in group is then selected. This is different from the proportionate selection that was described earlier. Another variation in the basic GA is the use of elitism. In a simple GA the most fit individual may not survive. Elitism saves the fittest individual and places it in next generation. Simple GA is generational; that is the new generation completely replaces old generation. Steady-state GA has overlapping generations. In a steady state GA a percentage of current generation gets replaced with newly created individuals. There are various methods of choosing which individuals to replace for example worst individuals, random replacement or parents. The steady-state GA can in some cases increase convergence.

Many factors influence convergence but the number of trial solutions and the percentage random mutation were the most important. Rapid convergence didn't always lead to the best solution.

The genetic algorithm is a domain independent, global optimization method that is simple to implement and very good results were achieved using these kind of optimizers.

During the synthesis process a genetic algorithm is used on the logarithm of the surface expansion coefficients. Restrictions are placed on the initial generation and further mutation of the chromosomes of the solution to prevent inflection areas (areas where the second derivative changes sign) on the subreflector. For this specific example the subreflector surface expansion is made on a surface with a projected circular aperture of 20 wavelengths as shown in Figure 12. The diameter of the projected aperture of

surface of the subreflector expansion is determined by ray tracing the main reflector edge rays from the maximum required scanned positions of the beam footprint to the focal region and choosing a diameter that overlaps the furthest subreflector rim points. The subreflector size and the projected area on which the expansion is made is therefore determined by the required scan width. For the example in Chapter 5 where the surface is described in terms of a mechanical finite element matrix the optimization parameters are the actuator amplitudes (or control voltages) and the Modified Jacobi polynomial description of the surface is only used to get initial values for the actuator amplitudes.

3.3. Design of a CONUS beam

A CONUS beam was designed using a Cassegrain dual offset reflector antenna with the following parameters for the unshaped surfaces:

Wavelength: 0.025

Main reflector focal length F : 72.639 wavelengths

Main reflector aperture D : 60 wavelengths

Main reflector offset y_c : 55.76 wavelengths

Subreflector tilt angle β_s : 14.32°

Subreflector eccentricity e : 2.879

Subreflector half interfocal distance c : 14.596 wavelengths

Feed tilt angle α : -29.07 °

Subreflector orientation α_s : 0°

β_s : -14.32 °

γ_s : 0°

Subreflector offset from main coordinate origin S_x : 0 wavelengths

S_y : -55.76 wavelengths

S_z : 0 wavelengths

Feed offset from unshaped focal point x_f : 0 wavelengths

y_f : 0 wavelengths

z_f : 0 wavelengths

Feed orientation α_f : 0°

β_f : -29.07 °

γ_f : 0°

Feed edge illumination level : -10 dB

Feed edge illumination angle: 12°

Subreflector oversizing factor: 1.2

Figure 17 shows the required surface deviation contours from the unshaped surfaces to produce a CONUS beam. Figure 18 shows the u-v space template and Figure 19 shows the achieved normalized coverage for the CONUS beam. The peak co-polarized gain was 34.57 dBi with a peak cross-polarized gain of 0.61 dBi.

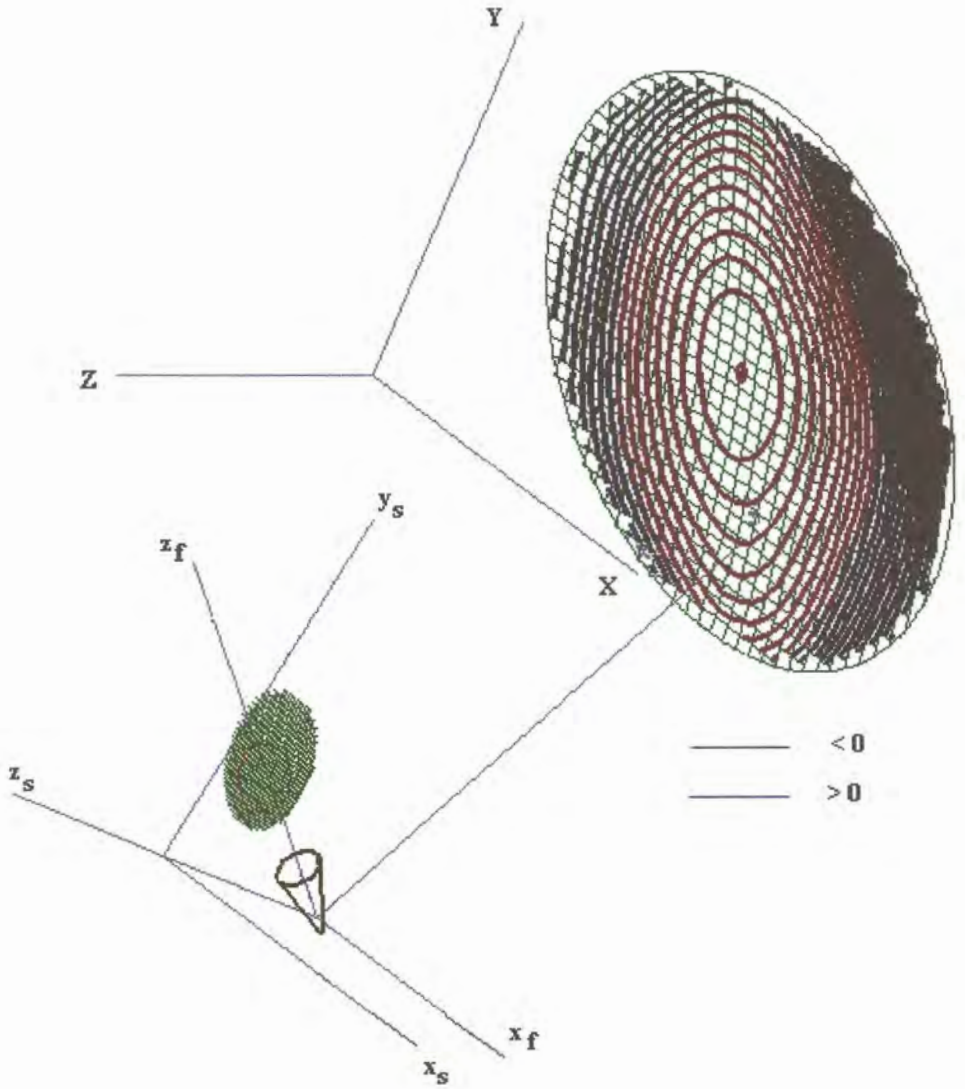

Figure 17. Required main and subreflector surface deviation in 1mm contour intervals for CONUS type contour beam.

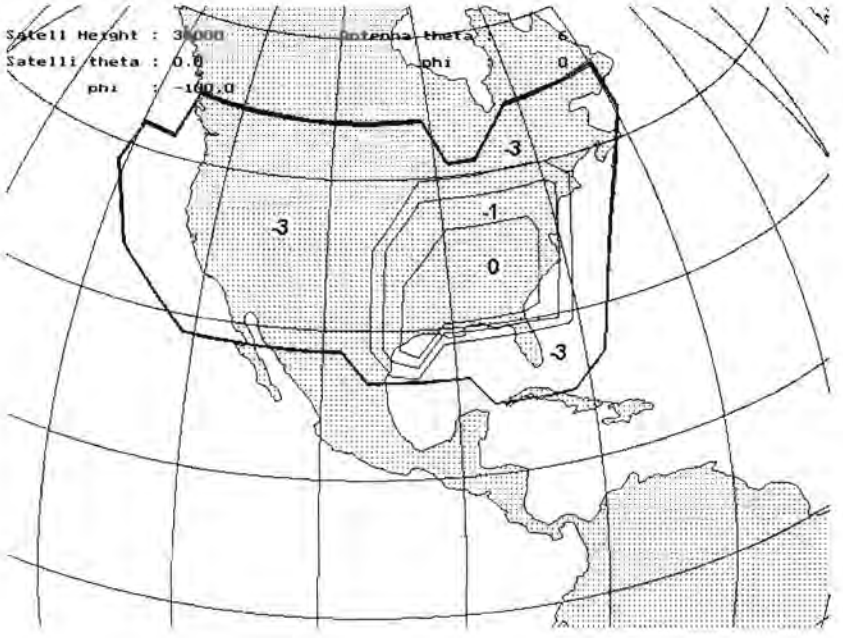

Figure 18. Template used to calculate cost function during synthesis of the CONUS beam.

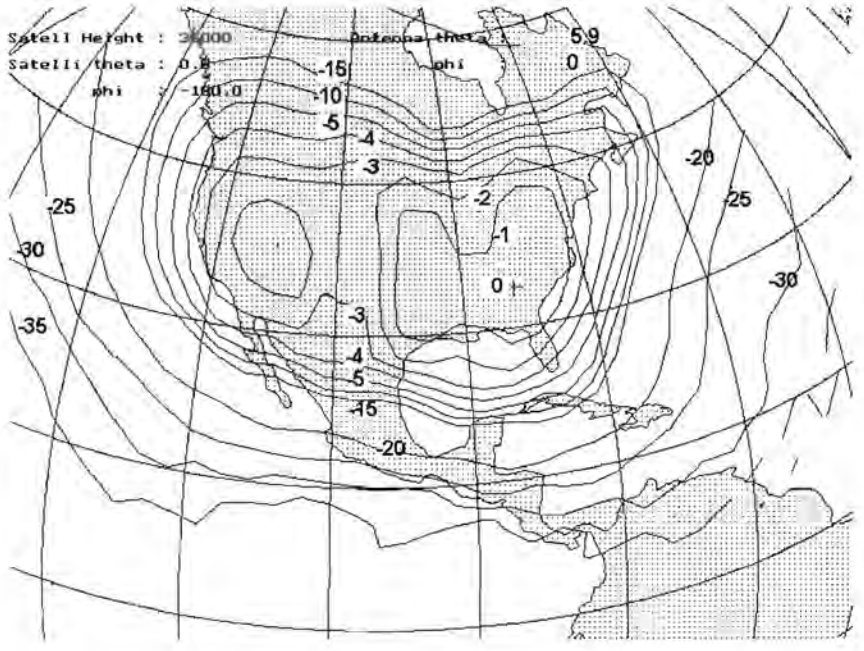

Figure 19. CONUS beam generated using combination of genetic and steepest gradient solvers in synthesis algorithm.

From Figure 19 the gain for the different gain regions can be seen to be achieved satisfactorily and comparison with the results in [11] also shows good agreement in terms of gain and cross polarization performance. This and other examples give confidence that the optimization routines are behaving as expected. The solutions obtained using steepest gradient solver are not always optimum and sometimes 'get stuck' in a local minimum. Operator intervention is required to get the coefficients in the Modified Jacobi polynomial series to the approximate values to ensure convergence and this seems to be acquired only through experience and the knowledge of what coefficients control what characteristics on the surface. Setting the lowest mode coefficients (C_{01}, C_{02}, C_{10} and D_{01} , D_{02} in Equation 2.134) to particular initial values seems to ensure a faster and better convergence. The genetic solver gives a good approximate solution within a reasonable time but seems to be unable to do a final convergence on the particular minimum. In the example shown a genetic solver is used to get an approximate solution and the steepest gradient solver is used to 'smooth' the footprint contours. In the following chapters the implementation of the mechanical finite element description of the surfaces into the diffraction synthesis code will be shown.

Chapter 4: Mechanical design of the dual reflector antenna

In Chapter 4 the mechanical properties of thin sheets are discussed and the set of differential equations governing their shape under different forces is shown. The first part of this dissertation simply examined the electromagnetic performance for a reconfigurable DCBR antenna. Next, the mechanical aspects of the design will be included. The feasibility of this antenna has been demonstrated by a practical mechanical design using piezoelectric adjustable linear actuators. This design is based on a mechanical finite element analysis of four prototype surfaces and a subsequent actuator placement study. In this study, the main reflector was assumed to be fixed and an adjustable subreflector surface was designed using a flexible material called Lexan. An actuator placement study was performed on materials with various stiffnesses to determine the suitability for this application by the smart structures division of the mechanical engineering department of The Ohio State University. A design was done using diffraction synthesis (shaping) on the main reflector and subreflector to produce a contiguous United States (CONUS) beam from a geostationary satellite position in its normal or undeformed mode. In this design, the main reflector and subreflector were shaped to produce the contour beam as was previously shown. A set of other coverage samples were chosen to study the ability to achieve coverage by mechanically unconstrained adjustment of the subreflector surface. A geographical area with comparable size but different shape was used first. Next a case requiring a smaller coverage area was evaluated. Brazil and South Africa were used as examples for these two studies. These subreflector surfaces were assumed as typical in terms of amplitude and size and an actuator placement study was performed using commercially available mechanical finite element code. The actual achievable mechanical surfaces were then used to evaluate the subsequent radiation pattern performance.

4.1. Mechanical description of surfaces using shell elements

Mechanically, the shape of the antenna is governed by a set of differential equations given by

$$\frac{\partial}{\partial\xi}\{\alpha_\eta N_\xi\}+\frac{\partial}{\partial\eta}\{\alpha_\xi N_{\eta\xi}\}+\frac{\partial\alpha_\xi}{\partial\eta}N_{\xi\eta}-\frac{\partial\alpha_\eta}{\partial\xi}N_\eta+\alpha_\xi\alpha_\eta\left(\frac{O_\xi}{R_\xi}+q_\xi\right)=0 \quad , (4.1)$$

$$\frac{\partial}{\partial\xi}\{\alpha_\eta N_{\xi\eta}\}+\frac{\partial}{\partial\eta}\{\alpha_\xi N_\eta\}+\frac{\partial\alpha_\eta}{\partial\xi}N_{\eta\xi}-\frac{\partial\alpha_\xi}{\partial\eta}N_\xi+\alpha_\xi\alpha_\eta(\frac{Q_\eta}{R_\eta}+q_\eta)=0\,, \quad (4.2)$$

$$\frac{\partial}{\partial\xi}\{\alpha_\eta Q_\xi\}+\frac{\partial}{\partial\eta}\{\alpha_\xi Q_\eta\}-\alpha_\xi\alpha_\eta\{\frac{N_\xi}{R_\xi}+\frac{N_\eta}{R_\eta})+\alpha_\xi\alpha_\eta q_\zeta=0 \quad , \quad (4.3)$$

$$\frac{\partial}{\partial\xi}\{\alpha_\eta M_\xi\}+\frac{\partial}{\partial\eta}\{\alpha_\xi M_{\eta\xi}\}+\frac{\partial\alpha_\xi}{\partial\eta}M_{\xi\eta}-\frac{\partial\alpha_\eta}{\partial\xi}M_\eta-\alpha_\xi\alpha_\eta(Q_\xi-m_\xi)=0\,, \quad (4.4)$$

$$\frac{\partial}{\partial\xi}\{\alpha_\eta M_{\xi\eta}\}+\frac{\partial}{\partial\eta}\{\alpha_\xi M_\eta\}+\frac{\partial\alpha_\eta}{\partial\xi}M_{\eta\xi}-\frac{\partial\alpha_\xi}{\partial\eta}M_\xi-\alpha_\xi\alpha_\eta(Q_\eta-m_\eta)=0 \quad (4.5)$$

where the α's are defined as the scaling factor, M is defined as the stress couple, N is the stress resultant, Q is the transverse shear stress resultant m is the moment load and q is the surface load. For certain shell shapes and actuation strategies equations (19-23) can be solved in closed form [20]. In this study, however, the solution was found by employing finite element analysis on the curved structure. In order to accomplish this task, 3600 (8 node) shell elements were used to discretize the reflector. The shell elements were configured to form the subreflector shape needed for the initial required geographical coverage area. Whenever a different shape is needed, high deflection piezoelectric actuators are utilized to force a new shape. In this case twenty three high deflection actuators were mounted at various points on the structure as shown in Figure 20. Note that the black dots represent actuator attachment locations on the internal surface. They were divided into 16 on the internal surface and 7 located at discrete points along the perimeter. Each actuator is made up of a stack of high deflection piezoelectric wafers called Rainbows as shown in Figure 21. A single wafer is dome shaped and capable of a deflection of about 0.5 mm. The equations that were utilized in modeling the deflection emanating from the Rainbows can be found in Reference [21]. To increase the deflection of an actuator comprised of these wafers, the wafers were placed in a clamshell configuration as shown in Figure 22. The actuator that is utilized in this study consists of a stack of 40 Rainbow actuators with a 2 inch diameter. This means that a clamshell stack of 40 is capable of about 2.0 cm of deflection.

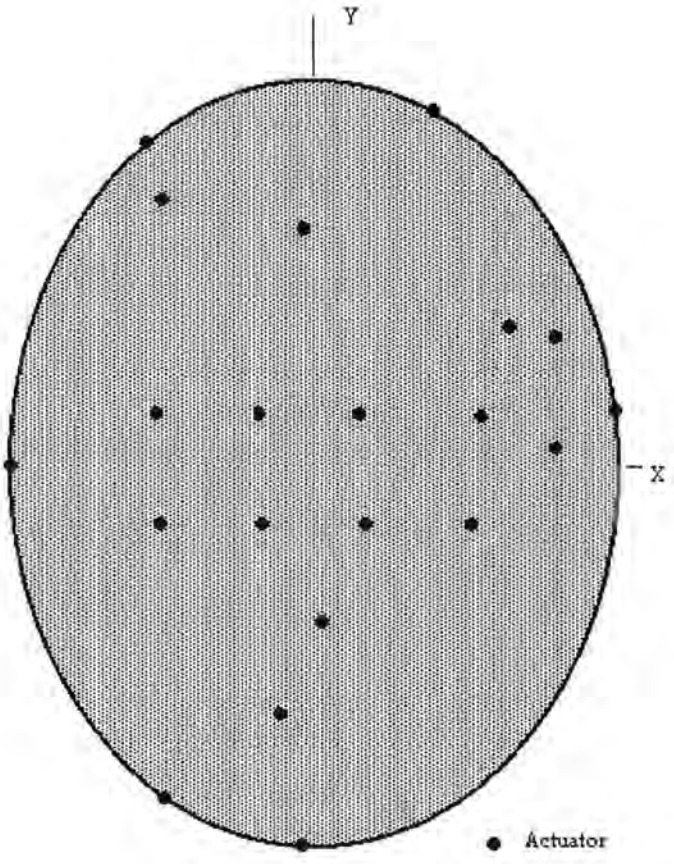

Figure 20. Actuator positions projected on the x_s-y_s plane.

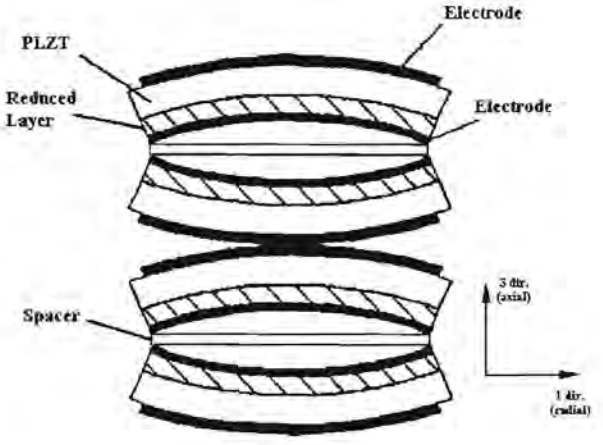

Figure 21. Showing individual stack showing clamshell configuration

The actuators are mounted to a rigid back surface. The flexible reflector is then draped over the actuators and the actuator ends are attached to the surface via epoxy. Spacers are used between the back surface and the actuator to ensure the proper height.

Actuator placement was done by examining a family of possible shapes and placing the actuators in locations that will produce these desired shapes. While this methodology is fast and effective, there are some shapes that a finite amount of actuators will not be able to achieve. This was not a major concern for two reasons: First, most required geographical coverage can be achieved using simple elliptically shaped beams oriented as needed. This eliminates some antenna shapes and some actuators. Second, the antenna can be designed based on all possible footprints that will likely be needed in the forseeable future. In addition, having too many actuators increases surface control complexity and thereby increases cost.

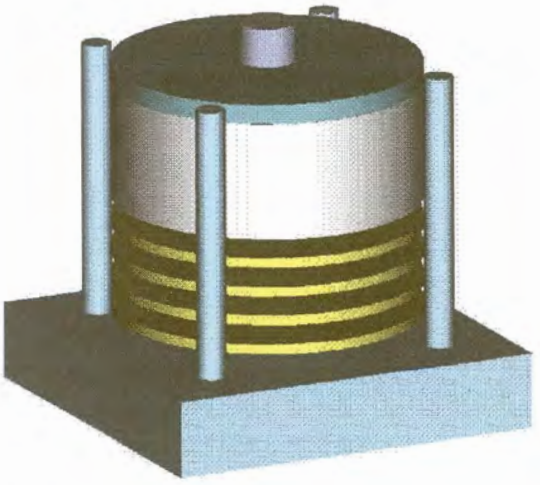

Figure 22. Rainbow actuators in stacked clam configuration.

4.2. Diffraction synthesis results and mechanical design performance

Three examples have been implemented to test the achievable accuracy of the surface after the mechanical design was completed. In the first example, a CONUS beam is synthesized for a geostationary position at 100°W. This done by optimizing 54 main- and subreflector surface expansion coefficients and three quantities associated with the feed position. A steepest gradient solver in combination with a genetic solver was used and achieved comparable results. Different designs were implemented to study the relation between beam scan angle, the required subreflector size and the ease of synthesis. A Cassegrain DCBR antenna with an aperture of 60 wavelengths was used. After the optimization for the CONUS beam, the main reflector surface is assumed to be fixed and all other beams were generated by only adjusting the surface of the subreflector. In this case no feed adjustment was made. This simulates a realistic implementation for an actual satellite antenna where it may not be easy to have an adjustable feed due to rigid RF components. Figure 18 shows the u-v space template and Figure 19 the achieved normalized coverage for the CONUS beam. The peak co-polarized gain was 34.57 dBi with a peak cross-polarized gain of 0.61 dBi. Figure 25 shows the achievable subreflector surface and the resulting co-polarized radiation footprint.

Next, the subreflector surface was adjusted to achieve a beam covering a geographical region of comparable size but of different shape and required gain. Brazil was selected from a geostationary position of 50°W. Figure 23 shows the antenna radiation footprint and the required deviation from the initial hyperboloid surface in 2 mm contour intervals. In this case no feed adjustment was made. Figure 26 shows the mechanically achievable surface and the calculated co-polarized radiation footprint for the adjusted actuators.

As a third test the subreflector surface was adjusted to achieve a beam covering Southern Africa from a geostationary position at 5°E. Figure 24 shows the antenna radiation footprint and the required deviation from the initial hyperboloid surface in 2

mm contour intervals. Figure 27 shows the mechanically achievable surface and the calculated co-polarized radiation pattern.

For the mechanical design a stationary feed constriction was assumed but two further diffraction syntheses were made adjusting the feed in the subreflector mother surface symmetry axis direction (z_s) and in the (x_s -y_s) plane. This reduced the required maximum surface deviation from 22mm to 12mm. The ability to adjust the feed gives a large degree of freedom in contour beam synthesis but may not be practical in many cases due to the rigidity of the feed network elements.

The feasibility of a practical reconfigurable contour beam antenna using a dual offset reflector configuration with an adjustable subreflector surface has been showed by a practical design of an adjustable surface. The next and most important step is to develop synthesis procedure incorporating a mechanical finite element (FEM) model using shell elements. This will be shown in the next section.

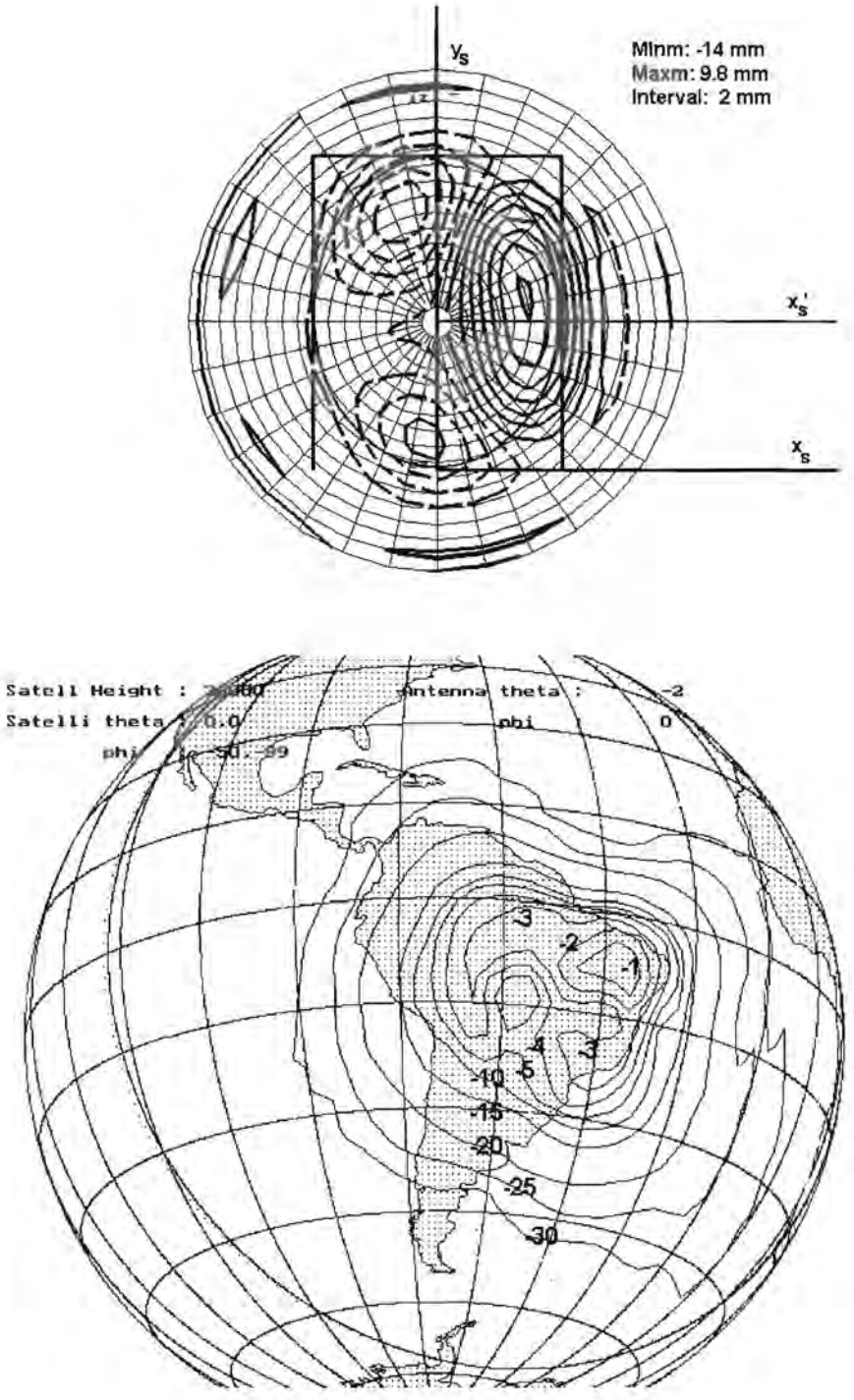

Figure 23. Required deviation from the initial hyperboloid surface in 2 mm contour intervals and the calculated co-polarized antenna radiation footprint for case 2.

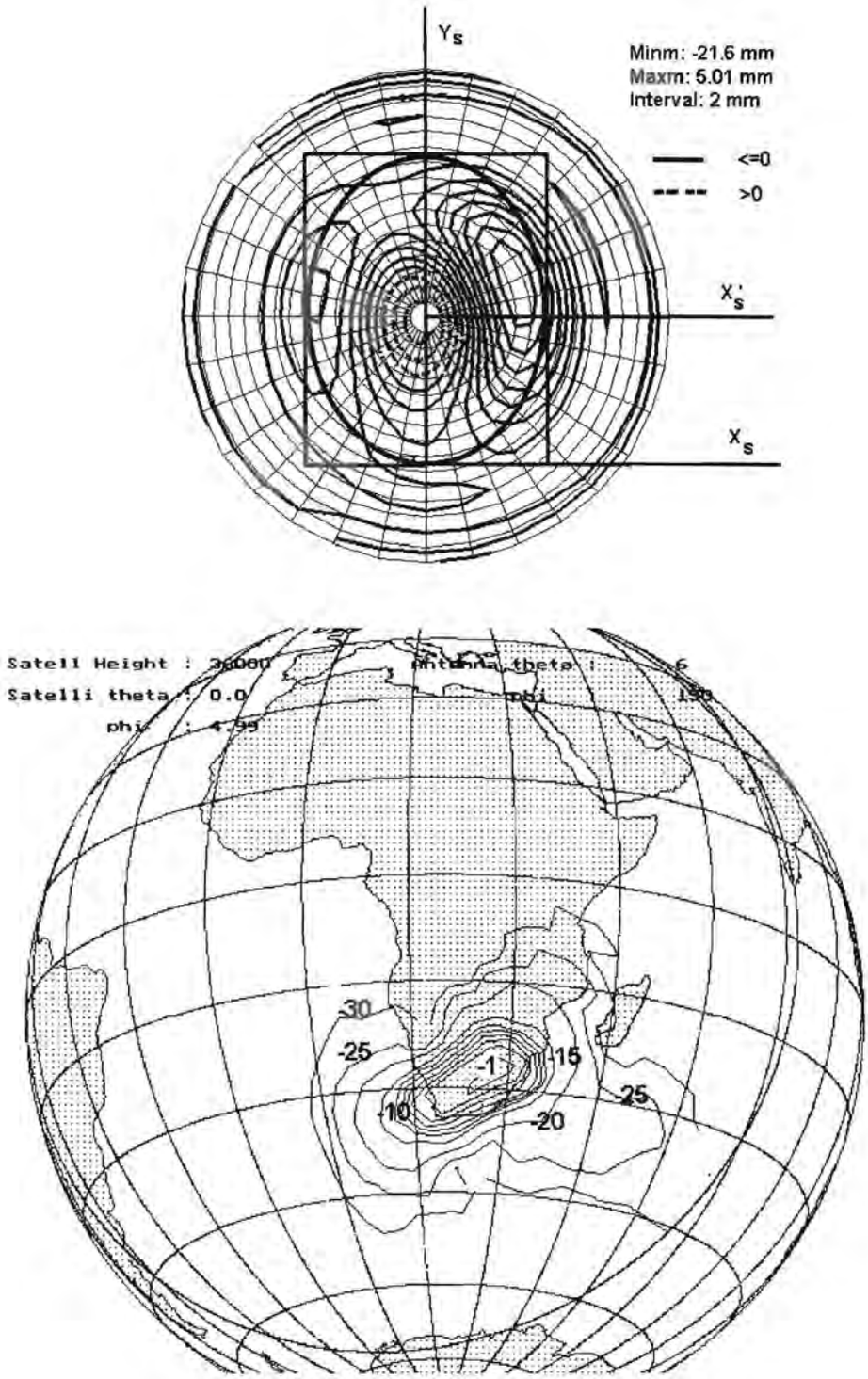

Figure 24. Required deviation from the initial hyperboloid surface in 2 mm contour intervals and the calculated co-polarized antenna radiation footprint for case 3.

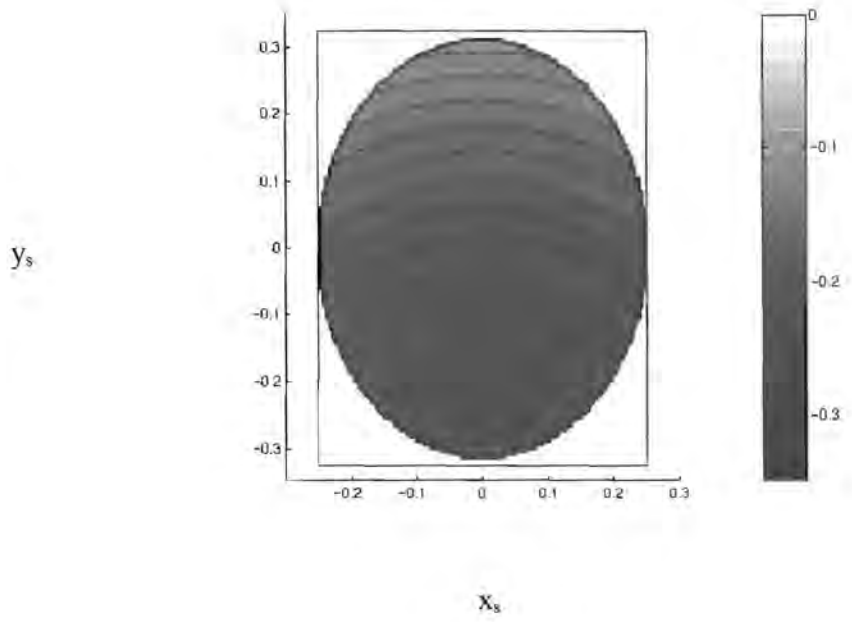

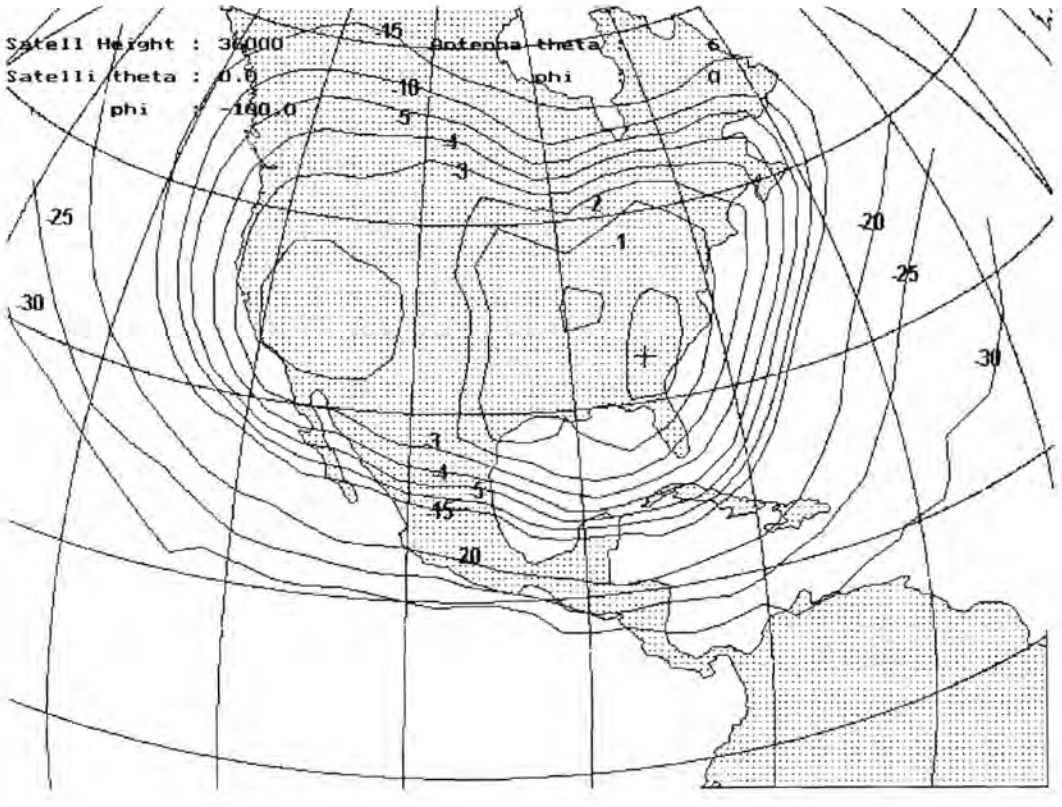

Figure 25. The achievable subreflector surface with no actuator adjustment and the resulting co-polarized radiation footprint.

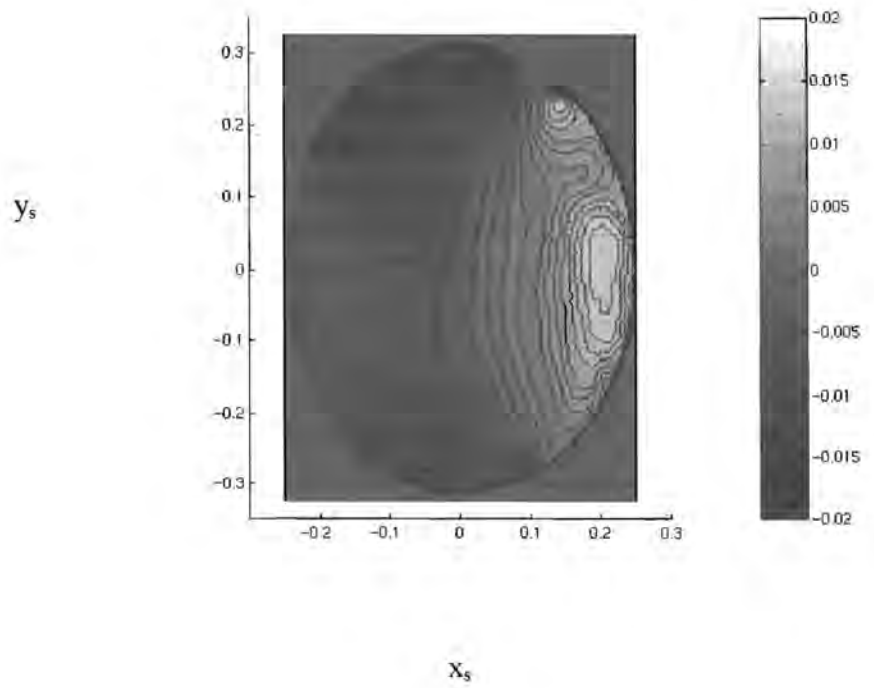

Figure 26. Mechanically achievable surface and the calculated co-polarized radiation pattern for case 2.

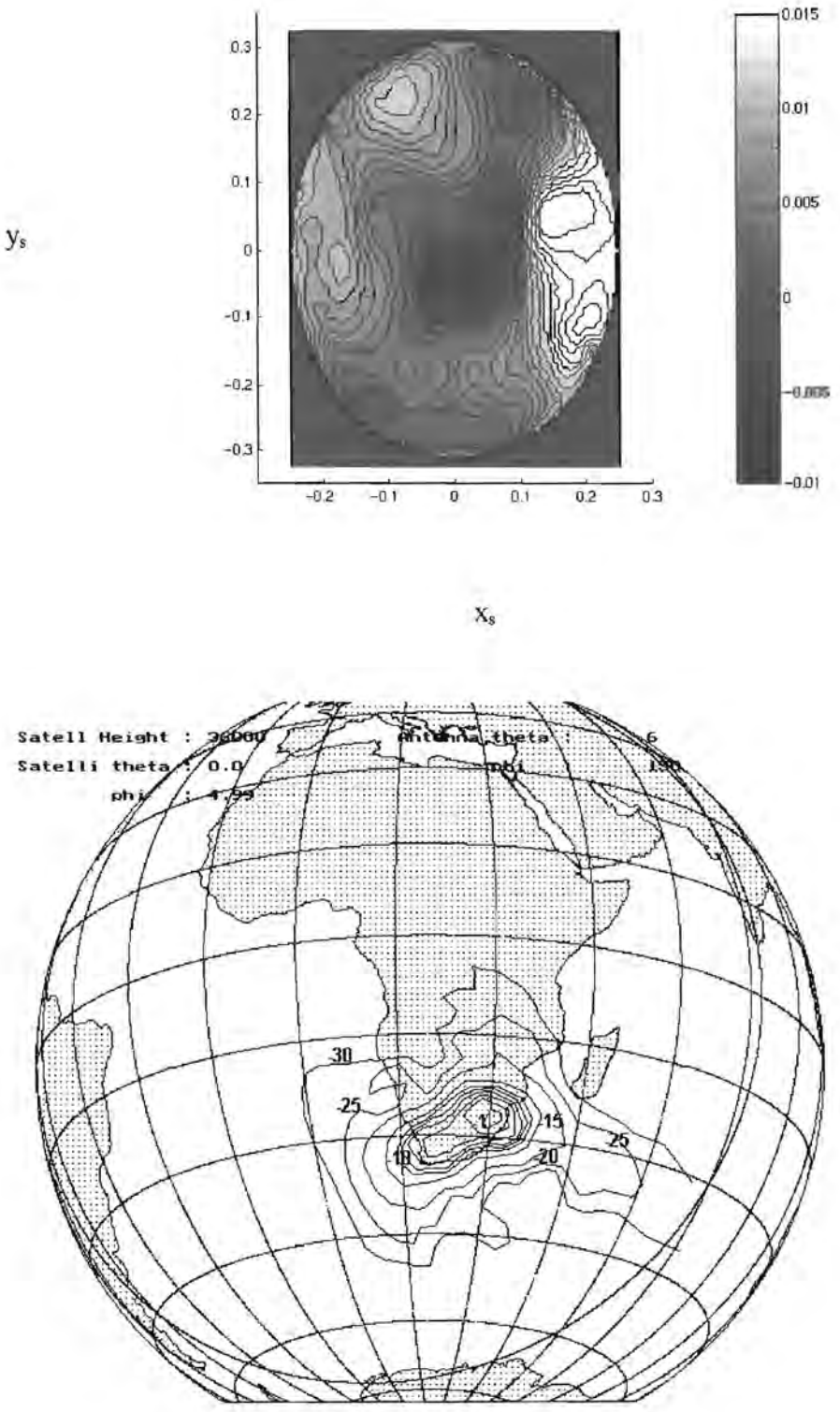

Figure 27. Mechanically achievable surface and the calculated co-polarized radiation pattern for case 4.

Chapter 5: Contour beam synthesis using the mechanical FEM surface description

The diffraction synthesis procedure written by the author was modified to incorporate a mechanical finite element description of the surfaces of the dual reflector antenna. The mechanical FEM unit developed by the Smart Materials and Structures division of the Department of Mechanical Engineering of The Ohio State University by Yoon and Washington, was designed to be compatible with the contour beam synthesis software. The resulting code enables direct synthesis in terms of the exerted actuator forces on a surface with a predefined stiffness matrix as described in the following paragraph.

The code also eliminates the second step of the FEM analysis described in Chapter 4 because the synthesis is now done on mechanically realistic surfaces using the actual actuator positions and displacements. In addition, many iterations can be performed much faster and more conveniently, as opposed to the examples in the previous chapter where essentially only one iteration was done on the mechanical surface. The result is a very useful tool to create a suitable design and predict the performance of the antenna taking into consideration the mechanical properties of the surface materials and the actuators used to reconfigure the antenna.
A new way of adjusting a reflector by bonding piezoelectric strips to a deformable surface was also studied [6] using this software.

5.1. Mechanical FEM diffraction synthesis

The FEM solver, developed in the Delphi RAD object oriented Pascal language by Yoon, was incorporated into to the synthesis software that was described previously in Chapter 2, also developed in Delphi by the author. The surface description of the reflectors (in this case the subreflector) is now made in terms of the actuator amplitudes instead of the modified Jacobi polynomial expansion coefficients used

previously for the examples in Chapter 3. The synthesis software reads the following set of data files:

a. Geometry file: Contains the unshaped main and subreflector parameters and the feed illumination function or feed data file.

b. Node file: Contains the node coordinates of the surfaces.

c. Connectivity file: Contains the connectivity table of the FEM elements.

d. Boundary condition file: Contains the boundary condition vector. This file gets updated at each iteration during the synthesis process.

The FEM code first sets up the global stiffness matrix from the material parameters and the node and connectivity data files. The material parameters are the Young's modulus, the Poison ratio relating form shape change and thickness of the shell elements.

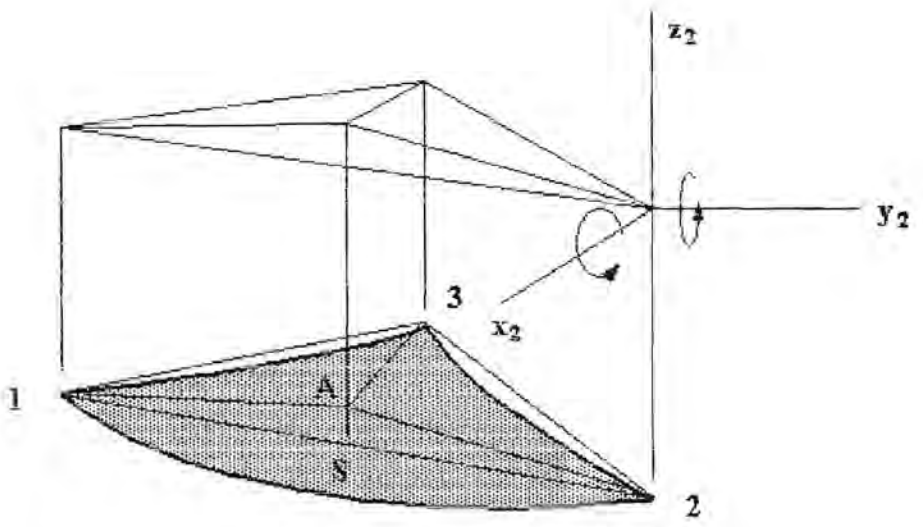

Figure 28. FEM shell element geometry

The stiffness matrix is now used together with the boundary condition file (containing initial actuator displacement values at certain node positions) and solved using a 'forward elimination and back substitution' method. The resultant vector gives the new node positions of the surface. Each element has three nodes as shown in Figure 28. Each node has 5 degrees of freedom namely a node position coordinate and two node rotations due to applied moments at the node.

The position S in Figure 28 is determined by finding position A first. To fall in the plane of points 1,2 and 3 within the area 123 the sum of areas 1A2, 2A3 and 3A1 must

be equal to the area of 123. This fact is used as a test to determine which element contains the specular point. Using the known rotation around any node and the distance 2A the position of S and the normal at S can be found.

The specular point on the subreflector is found as before using the known integration point and feed position and the Newton method with the LU solver. Figure 29 shows the subreflector projection in the x_s - y_s plane and the FEM node- and element positions.

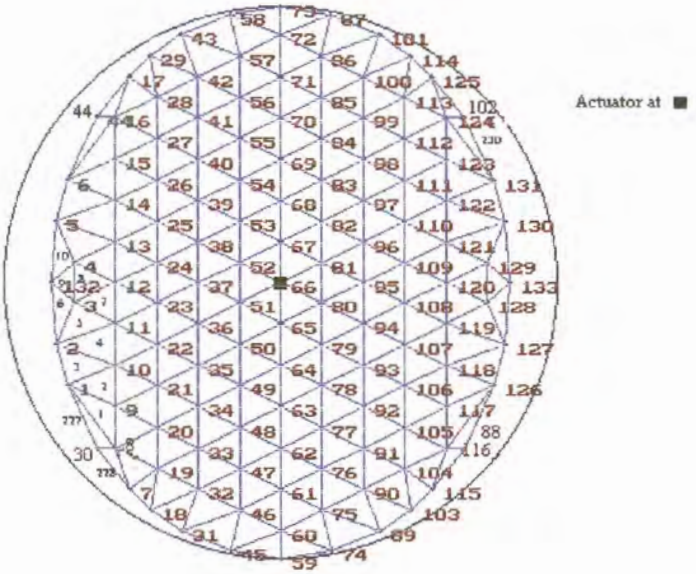

Figure 29. Subreflector projection in the x_s - y_s plane showing the FEM node- and element positions.

Figure 30 shows the surface deviation contours with the actuators at the positions indicated and actuator 66 adjusted to 10 mm for a typical flexible plastic surface 0.05" thick. It can clearly be seen from the contour levels (blue contours are positive and magenta contours are negative) that actuator placement is critical to prevent undesired "buckling" in thin, stiff materials.

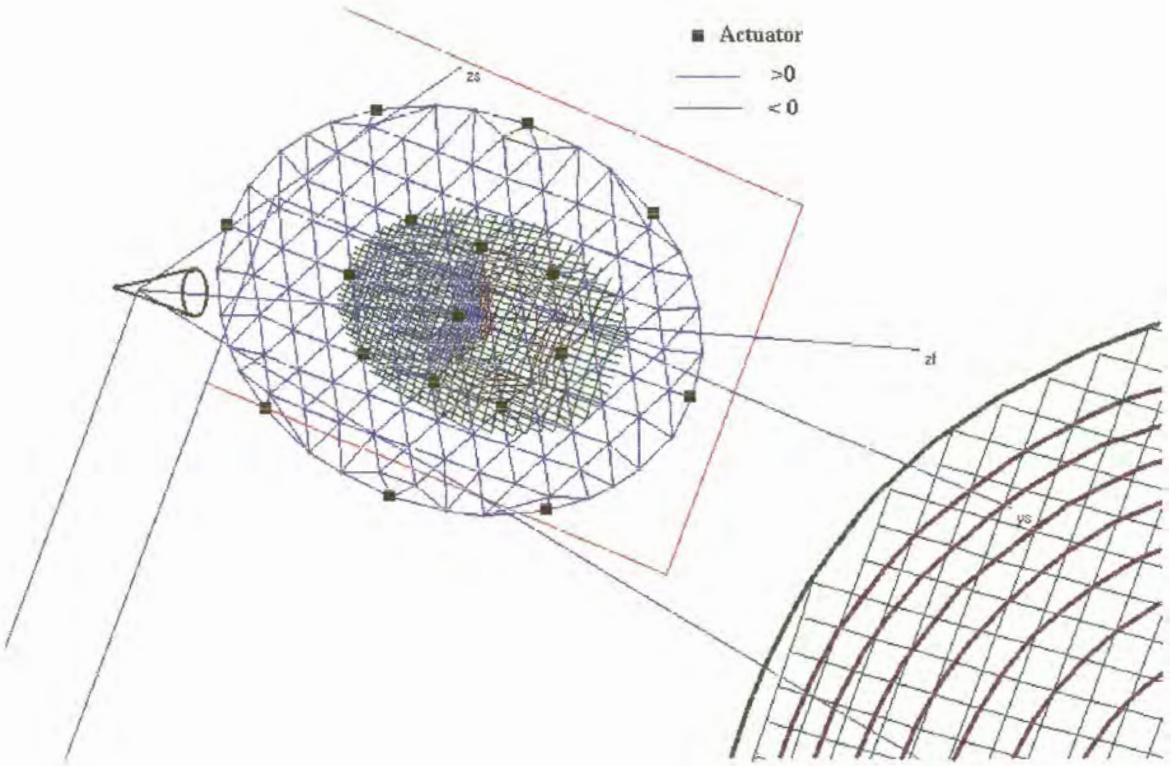

Figure 30. Subreflector surface deviation due to displacement of actuator 66 by 10mm.

This example illustrates that real mechanical implementation issues, for example buckling of the adjustable reflector antenna surface, can now be addressed.

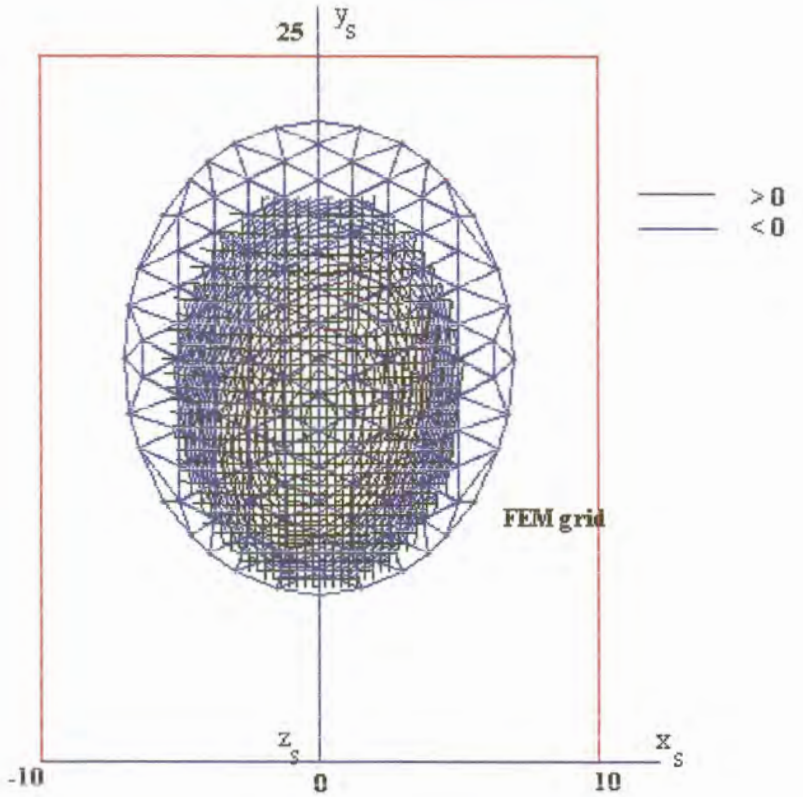

Figure 31. Required surface deviation contours in 1 mm contour intervals for the subreflector surface with an unshaped main reflector giving a cost function of 59.5 units on an elliptical contour beam case.

5.2. The effect of mechanical surface properties on actuator number and placement

In order to determine the minimum number of actuators and where they should be placed a simple elliptical beam shape was synthesized changing the thickness and stiffness of the surface each time for three actuator arrangement patterns. The actuators were placed in equispaced triangular pattern first, then in a rectangular pattern and finally in a radial pattern. These patterns were chosen to make a general study of actuator placement effects as opposed to the case specific placements done before. The following reflector material properties were adjusted: Young's modulus

and material thickness. The Poisson ratio was kept constant at 0.334 which is a typical value for stiff polymers.

As a case study a 7° x 4.5° elliptical beam with the main semi-major axis tilted 45° was used to study the effect of surface material thickness on the required number of actuators. This study determined the minimum number of actuators for a given surface to guarantee a given cost function value. The unshaped cost function value ψ from Equation 3.1 is 149.5 units. Figure 31 shows the required surface deviation for the subreflector with no main reflector shaping that produce a cost function value of 59.5 units. A minimum of 65 is deemed acceptable and the minimum number of actuators that can achieve this value are determined. Figures 32 (a)-(c) show the triangular actuator pattern for three cases with different material thickness with 14, 21 and 39 actuators respectively. In each case the surface material stiffness is kept at a typical constant value for sheet plastic. Figures 33 (a)-(c) show the rectangular actuator pattern for the three material thickness cases with 14, 21 and 39 actuators respectively and Figures 34 (a)-(c) show the actuator arranged along a radial pattern with 8 radials for the three cases with 14, 21 and 39 actuators respectively. The number of actuators are not equal for each of the cases of each example but they are almost the same and for the lower actuator numbers a greater portion of actuators lie in the rim region that do not contribute significantly to the radiation pattern shape.

Table 1 shows the three actuator arrangement patterns and the cost function for each of the surface material thickness. From Table 1 it can be seen that the 0.05" surface needs many actuators to give acceptable performance. Another case is run with 65 actuators arranged in the triangular pattern that achieves the required cost but the actuators have to be spaced with their center lines 3.5 cm apart. In the case of the Rainbow piezoelectric stack this arrangement is impossible but alternative linear actuators may be considered. More control over the surface is achieved in the 0.1" surface thickness case but the best performance for each case is for the 0.3" surface. This use of this surface may be impractical due to the force that the actuators must be able to exert on the surface.

The radial arrangement of the actuators does not make the minimum cost for any case because 8 radial 'spokes' are used. This leaves large areas uncontrollable. This is an issue that needs to be addressed in a design of bonded piezoelectric surfaces to the back of a reflector as proposed in [6].

The performance of the triangular and rectangular actuator arrangements is almost the same with the triangular arrangement slightly better.

Thickness (inch)	Triangular		Rectangular		Radial	
	Number	Cost	Number	Cost	Number	Cost
0.05	16	109.6	15	102.1	14	104.7
	22	93.6	21	96.8	21	93.1
	38	82.1	40	88.1	39	71.8
0.1	16	86.2	15	87.6	14	94.5
	22	74.6	21	79.2	21	73.1
	38	62.2	40	64.2	39	70.1
0.3	16	77.5	15	76.3	14	92.1
	22	64.2	21	67.7	21	69.2
	38	60.1	40	61.6	39	66.1

Table 1. Cost function comparison of actuator number and arrangement for different surface thickness.

This study gives an understanding of the required surface thickness and the number of actuators required to achieve a desired shape. The same procedure needs to be applied if a material of a different stiffness is used. In the next section the experience gained from this study is applied to generate arbitrary antenna radiation footprints.

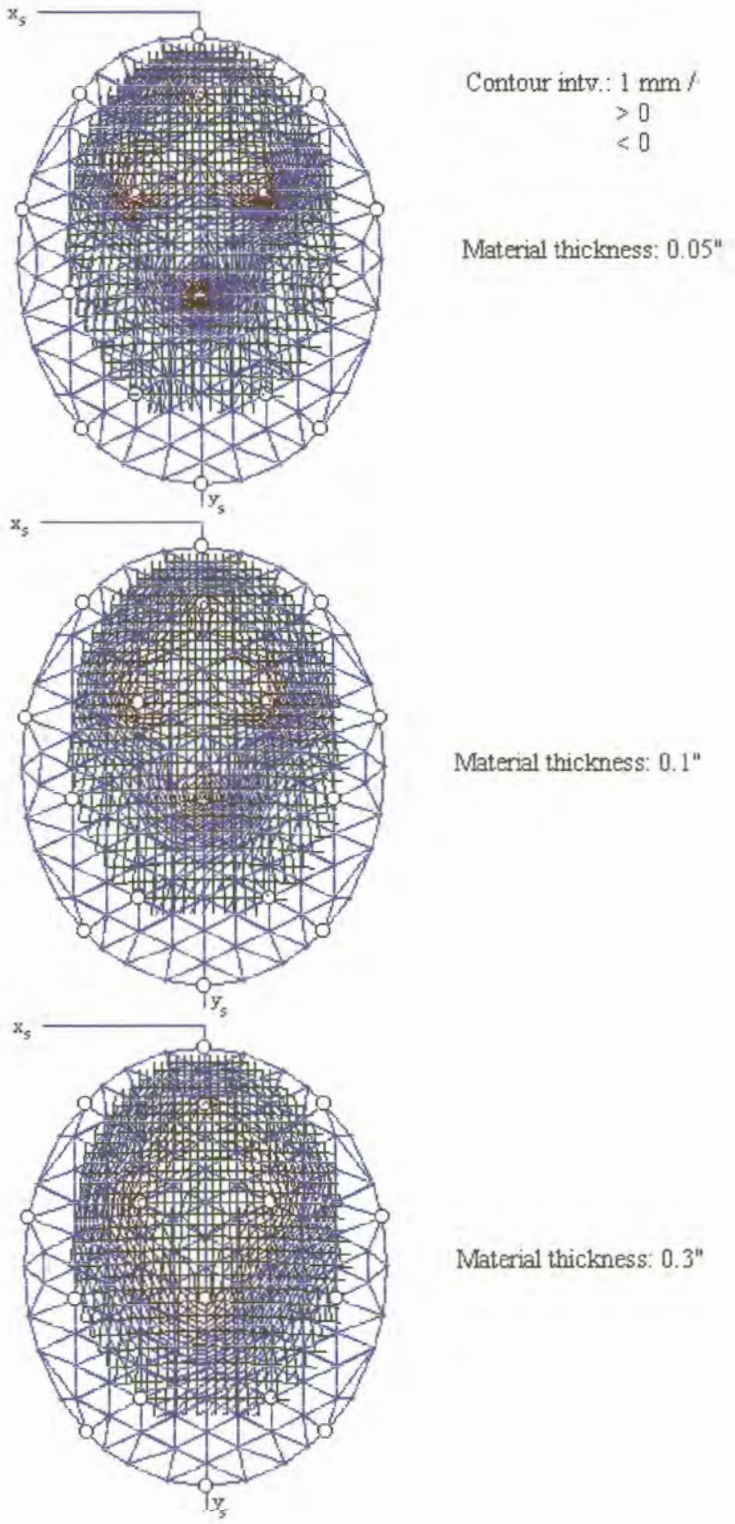

Figure 32 (a) Surface deviation contours for 16 actuators arranged in a triangular pattern and bonded to different surface material thickness of 0.05", 0.1" and 0.3" respectively.

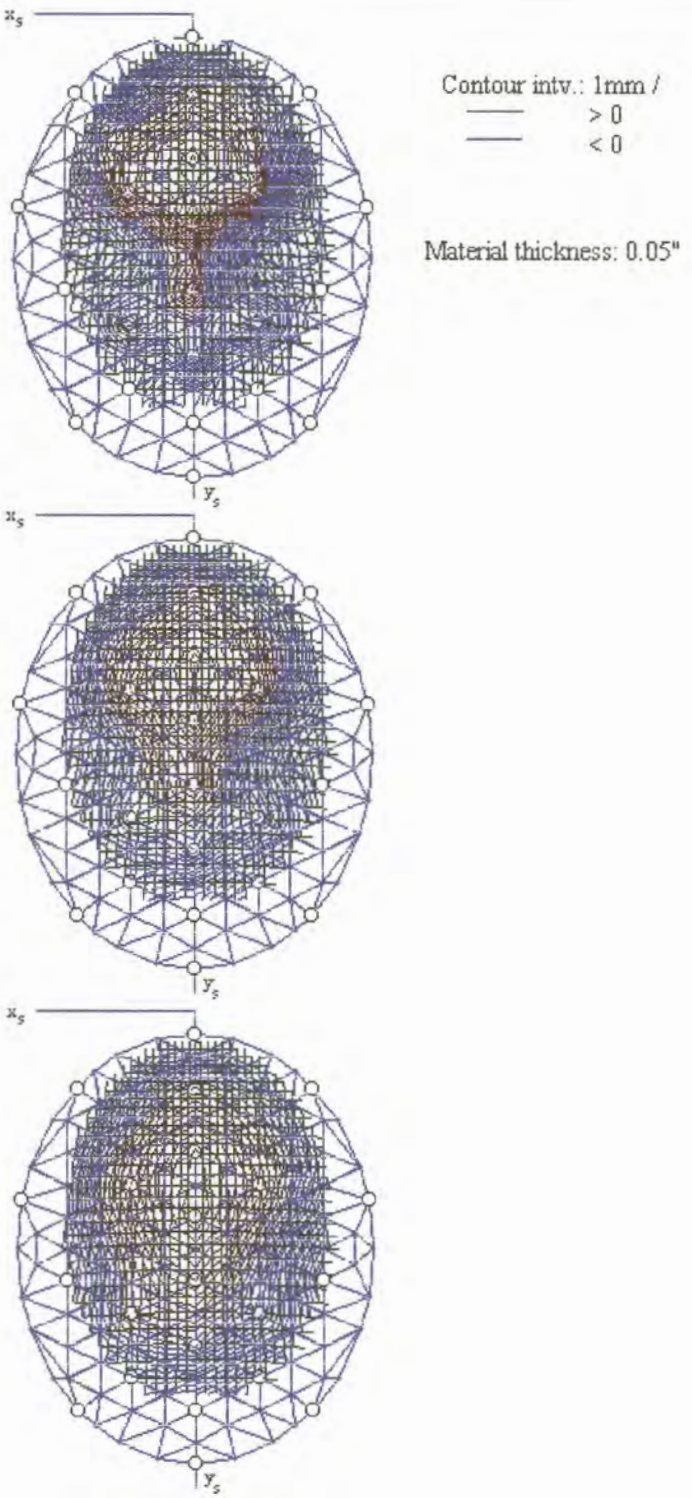

Figure 32 (b) Surface deviation contours for 22 actuators arranged in a triangular pattern and bonded to different surface material thickness of 0.05", 0.1" and 0.3" respectively.

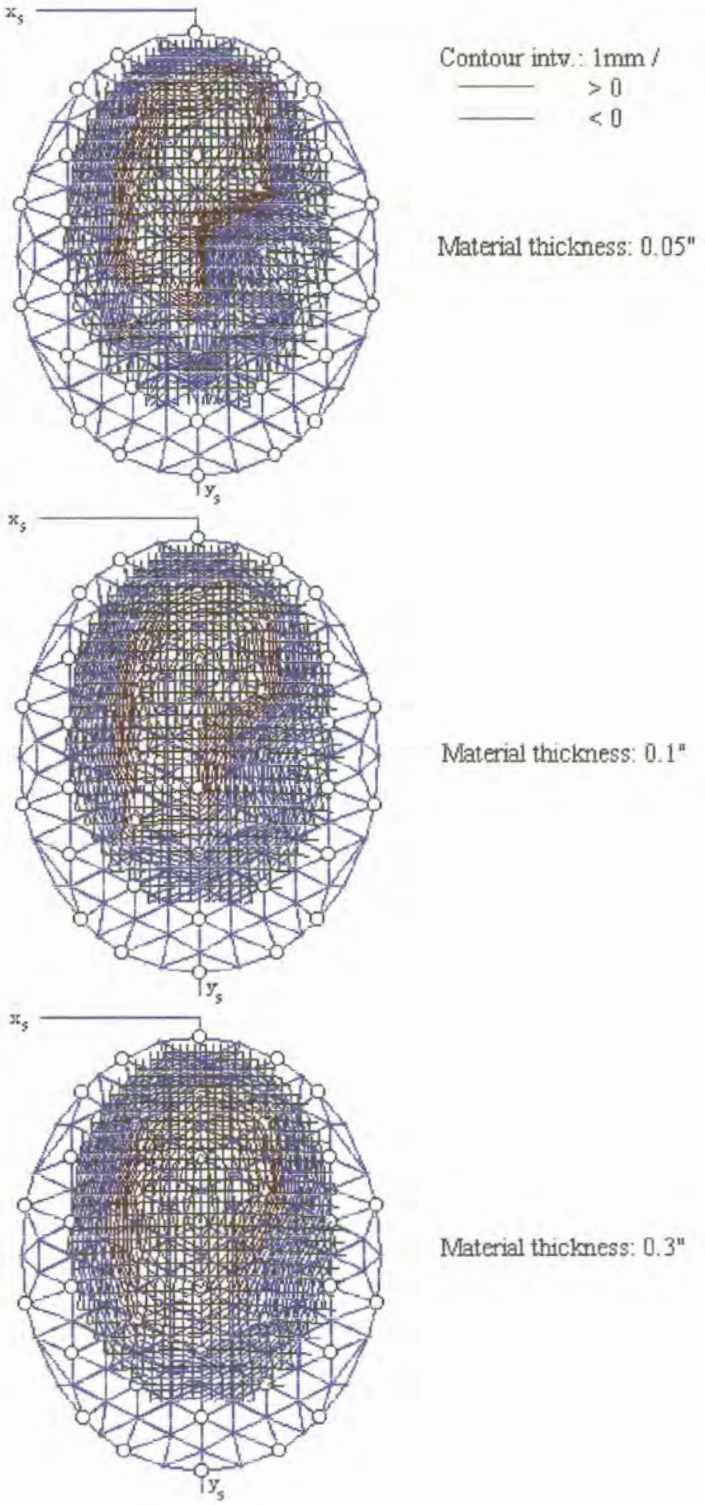

Figure 32 (c) Surface deviation contours for 38 actuators arranged in a triangular pattern and bonded to different surface material thickness of 0.05", 0.1" and 0.3" respectively.

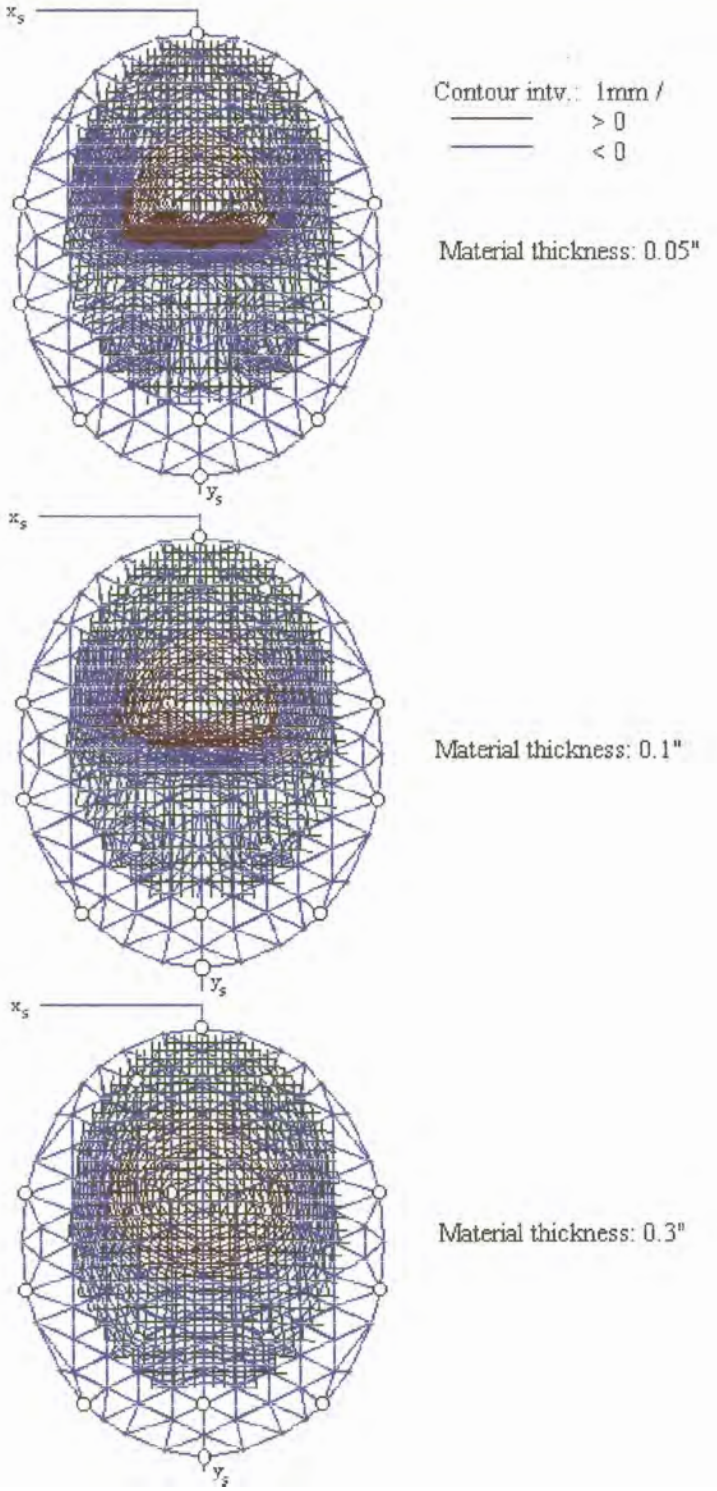

Figure 33 (a) Surface deviation contours for 15 actuators arranged in a rectangular pattern and bonded to different surface material thickness of 0.05", 0.1" and 0.3" respectively.

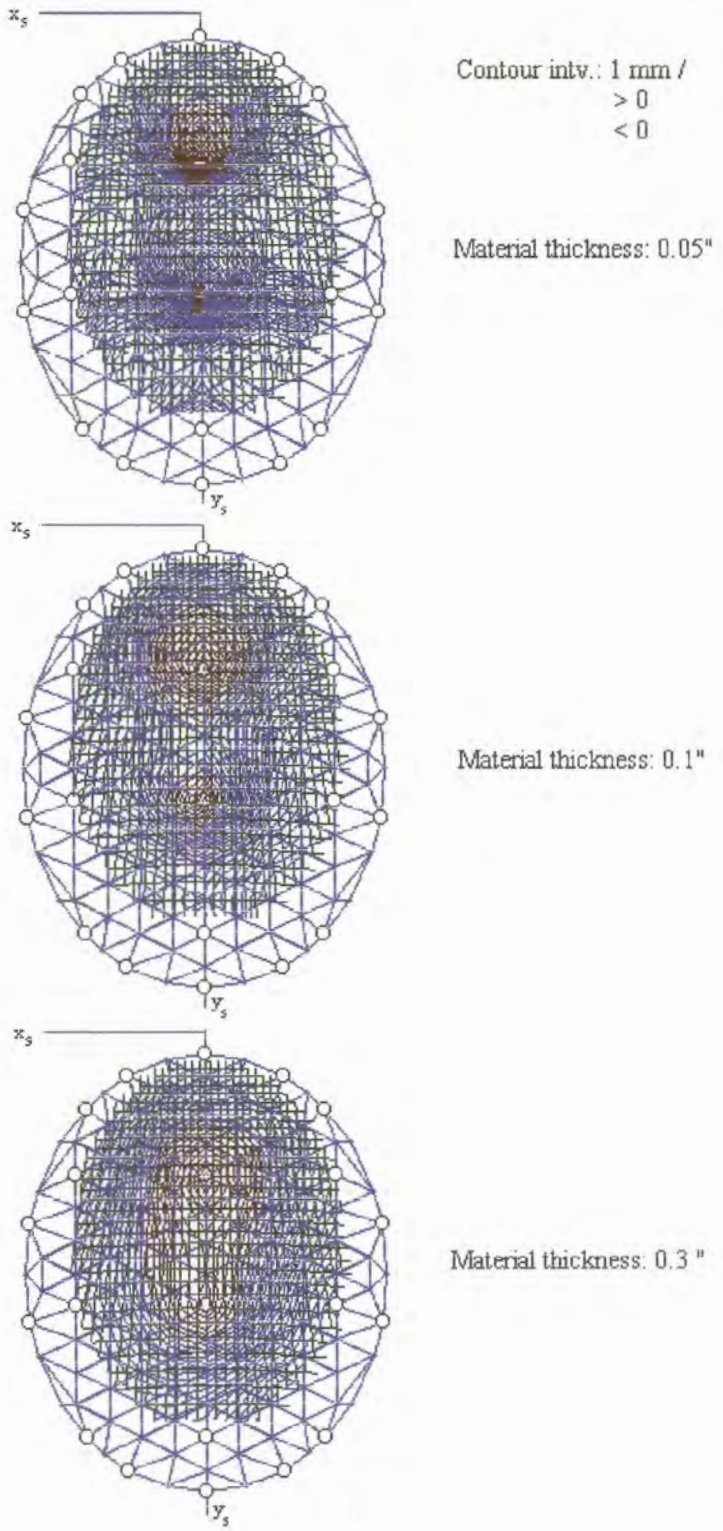

Figure 33 (b) Surface deviation contours for 21 actuators arranged in a rectangular pattern and bonded to different surface material thickness of 0.05", 0.1" and 0.3" respectively.

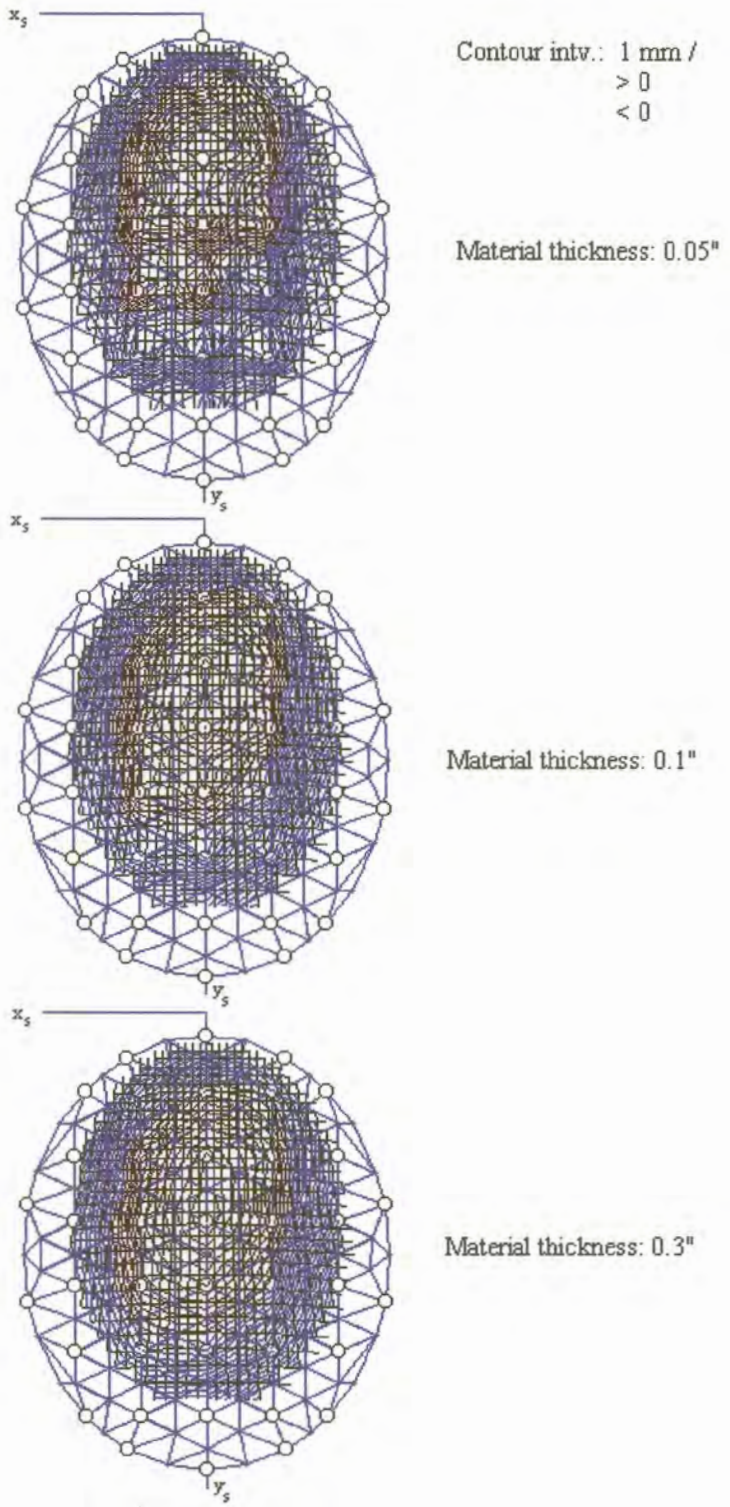

Figure 33 (c) Surface deviation contours for 40 actuators arranged in a rectangular pattern and bonded to different surface material thickness of 0.05", 0.1" and 0.3" respectively.

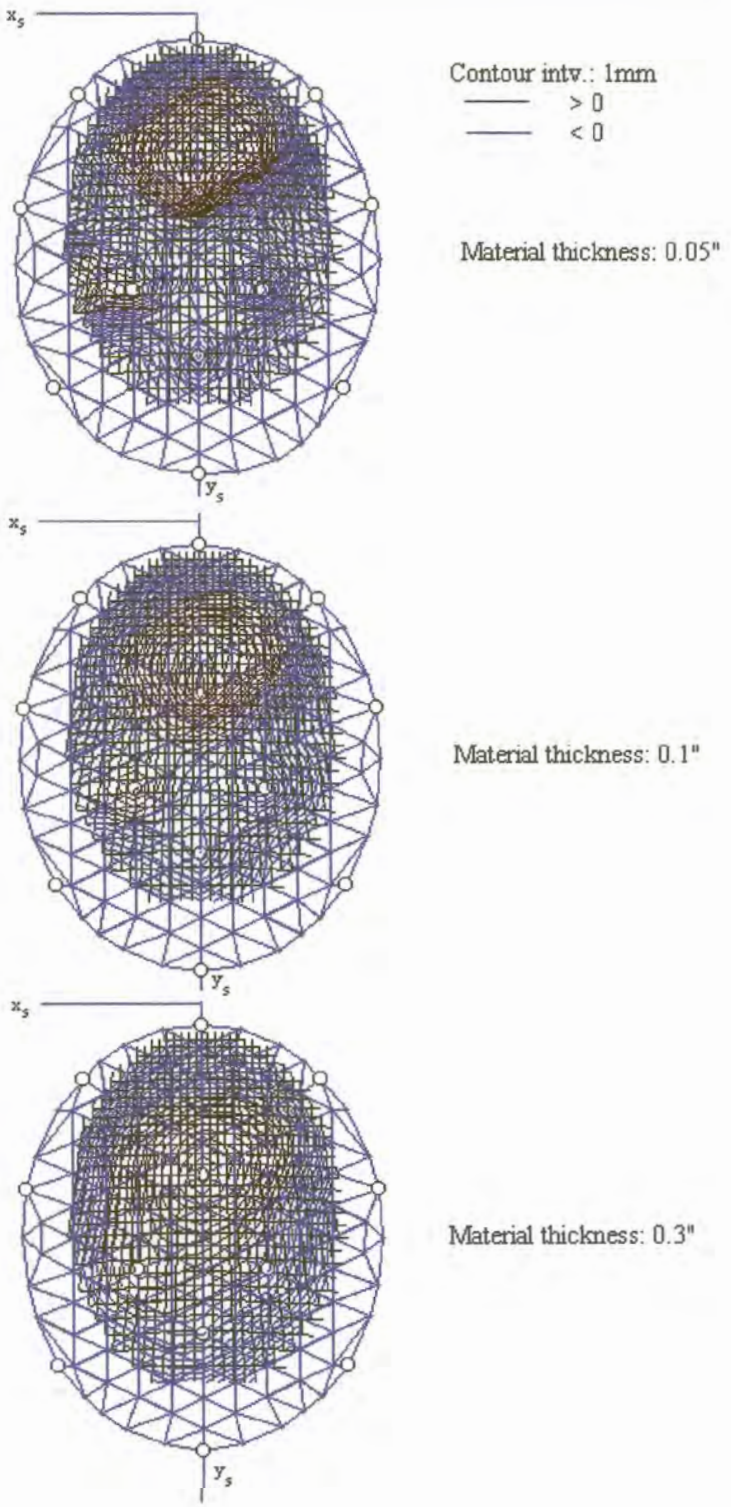

Figure 34 (a) Surface deviation contours for 14 actuators arranged in a radial pattern and bonded to different surface material thickness of 0.05", 0.1" and 0.3" respectively.

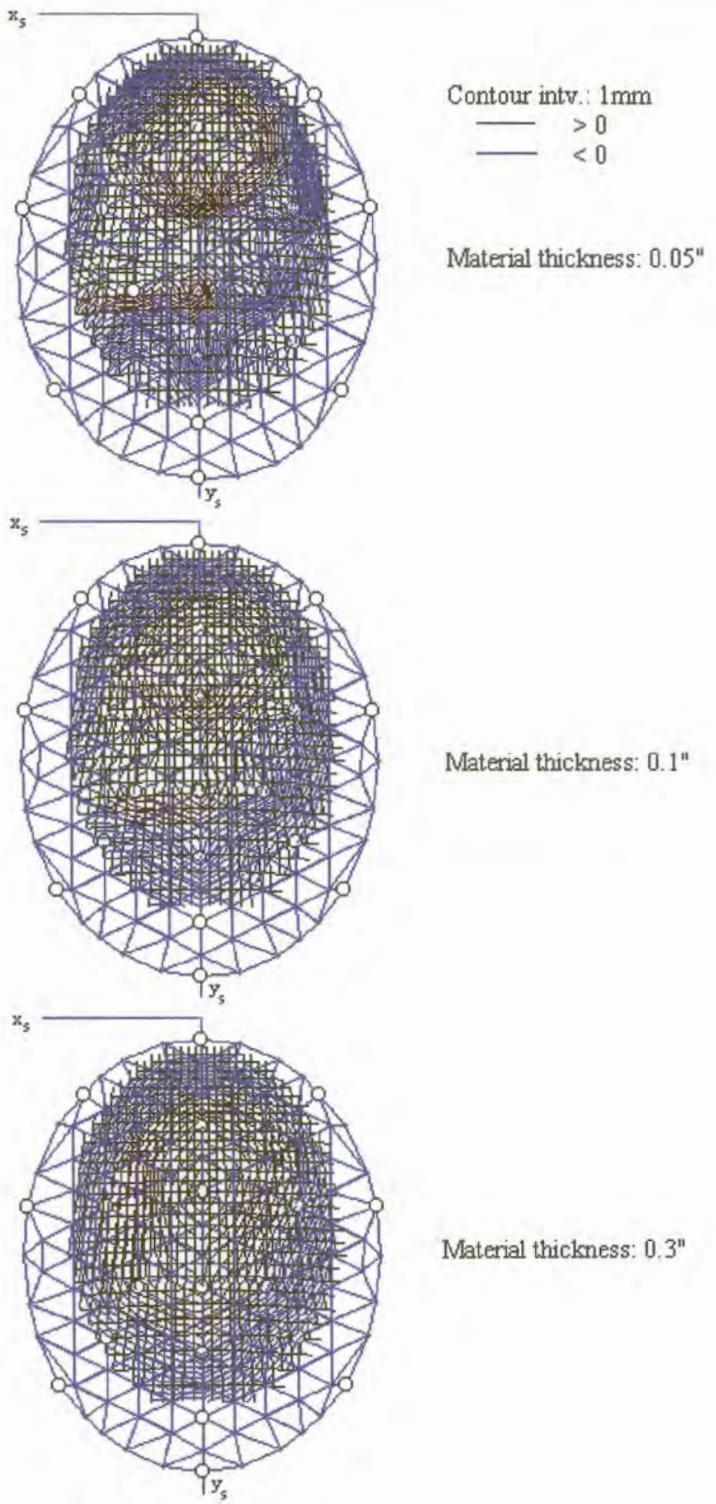

Figure 34 (b) Surface deviation contours for 21 actuators arranged in a radial pattern and bonded to different surface material thickness of 0.05", 0.1" and 0.3" respectively.

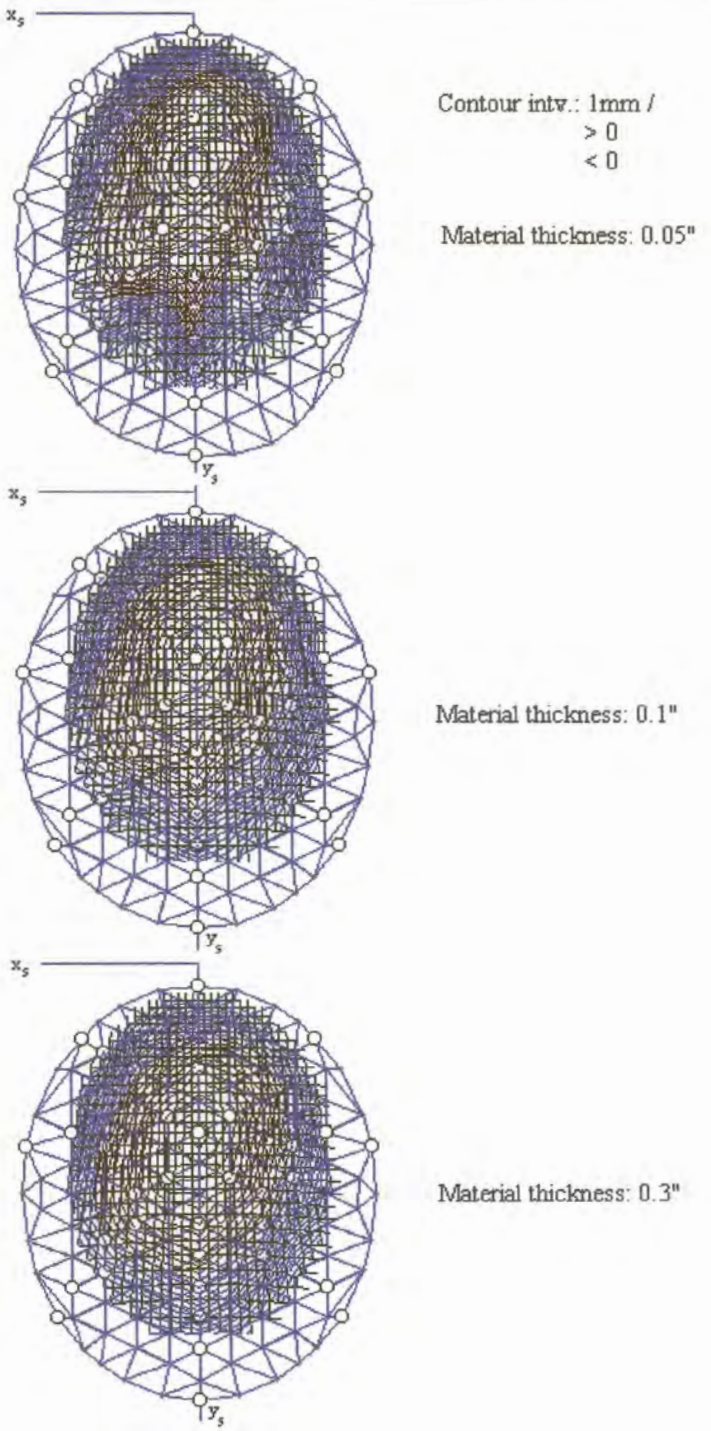

Figure 34 (c) Surface deviation contours for 39 actuators arranged in a radial pattern and bonded to different surface material thickness of 0.05", 0.1" and 0.3" respectively.

5.3. Synthesis of an adjustable elliptical beam using the mechanical FEM surface description

As an example application an adjustable elliptical beam was generated using 38 actuators in the positions shown in figure 31(c) on the subreflector of a dual offset reflector antenna with an unshaped main reflector. In each of the syntheses performed Lexan was used as subreflector material with the following properties

Young's modulus: 0.2×10^{10}

Poisson ratio: 0.334

thickness: 0.2×0.00254m

Figure 31(c) shows the subreflector surface deviation for the 45° case. The co-polarized far-field for 0°, 45° and 90° cases are shown in Figure 35, 36 and 37 respectively. A surface synthesis was first performed on a modified Jacobi polynomial surface expansion to get approximate values for the actuators. After this the FEM diffraction synthesis procedure is applied. This is done because the FEM diffraction synthesis procedure is much slower and the approximate actuator values ensures that a faster convergence is obtained the final solution is found within a few iterations.

This example illustrates the reconfigurability of the antenna system using the adjustable subreflector. This example also shows a practical advantage of the method since a lot of geographical coverage requirements can be satisfied by simple elliptical contour beams [22].

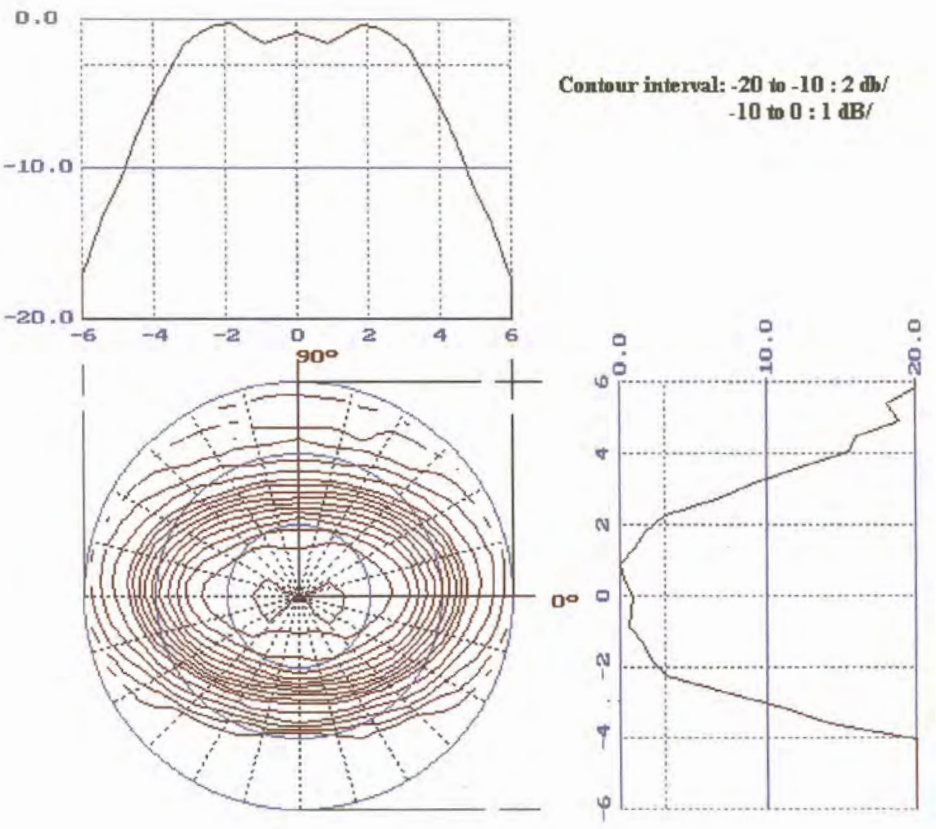

Figure 35. Co-polarized far-field for the 0° elliptical beam case.

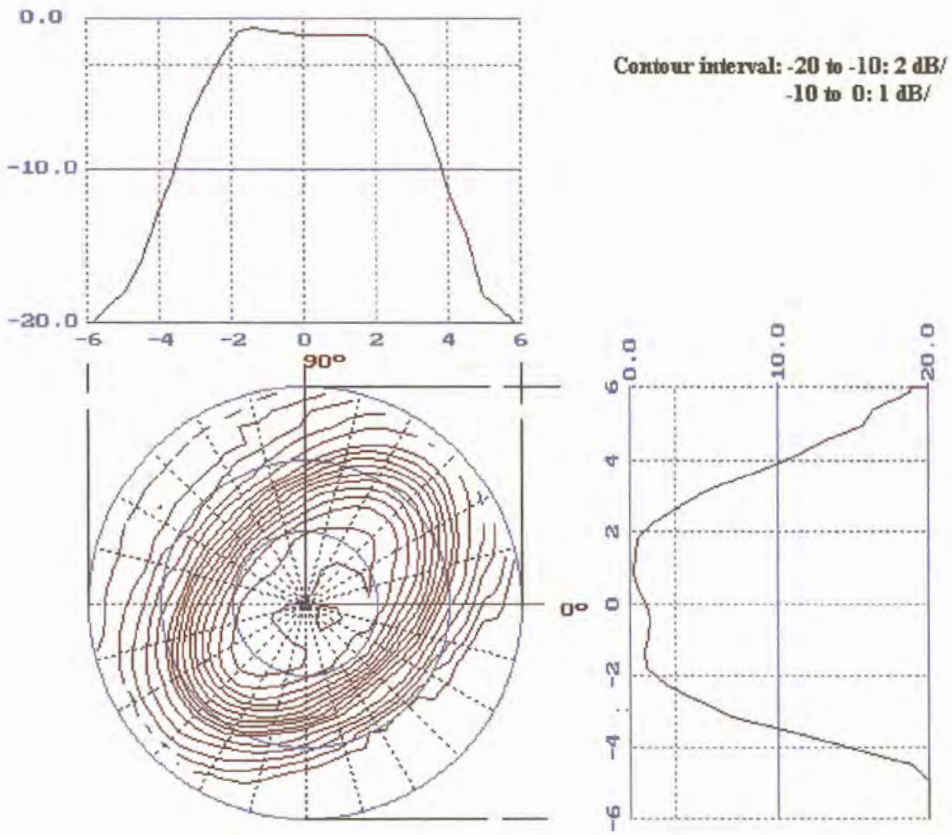

Figure 36. Co-polarized far-field for the 45° elliptical beam case.

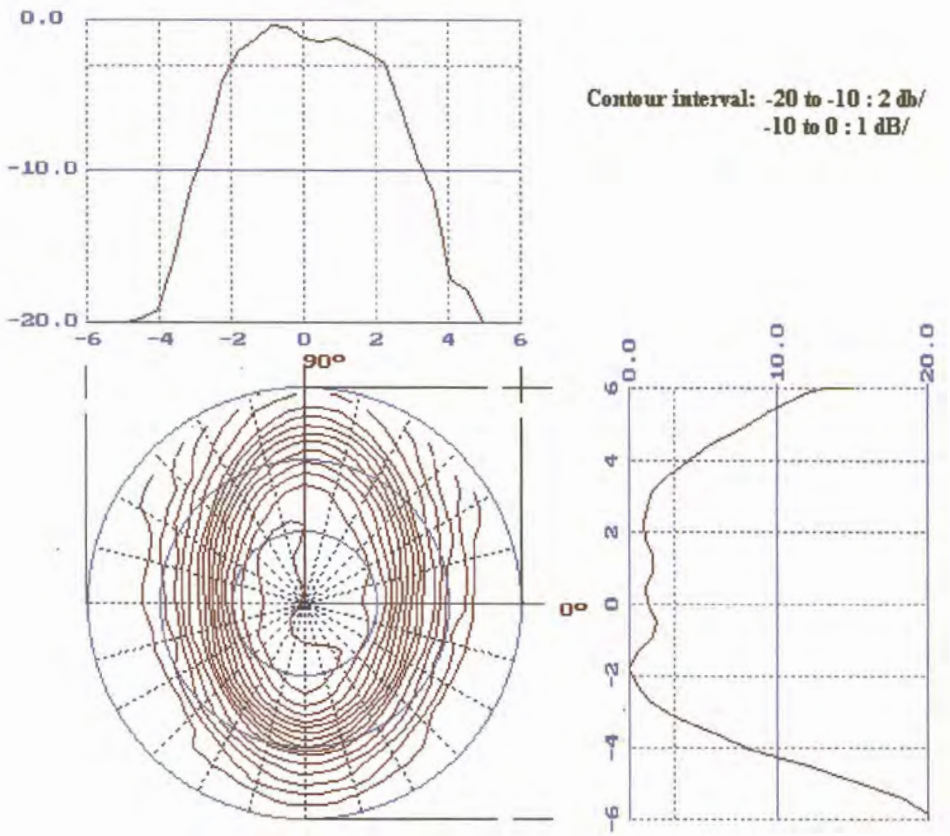

Figure 37. Co-polarized far-field for the 90° elliptical beam case.

5.4. Synthesis of an reconfigurable beam using the mechanical FEM surface description

The FEM diffraction synthesis code is finally re-applied to the three examples described in Chapter 4. In Chapter 4 the actuator placement study is done to determine actuator positions that can achieve the required pattern within a certain cost for the three cases. In the following examples a more general triangular actuator arrangement pattern is used. A reconfigurable beam was generated using 38 actuators in the positions shown in figure 31(c) on the subreflector and the same shaped main reflector as before. As an additional case the same configuration was used to generate an Australian beam.

In each of the syntheses performed Lexan was used as reflector material with the following properties

Young's modulus: 0.2×10^{10}

Poisson ratio: 0.334

thickness: 0.2×0.00254m

The co-polarized far-field for the Brazilian, Southern Africa and Australian beams are shown in Figure 38, 39 and 40 respectively. A surface synthesis was first performed on a modified Jacobi polynomial surface expansion to get approximate initial values for the actuators.

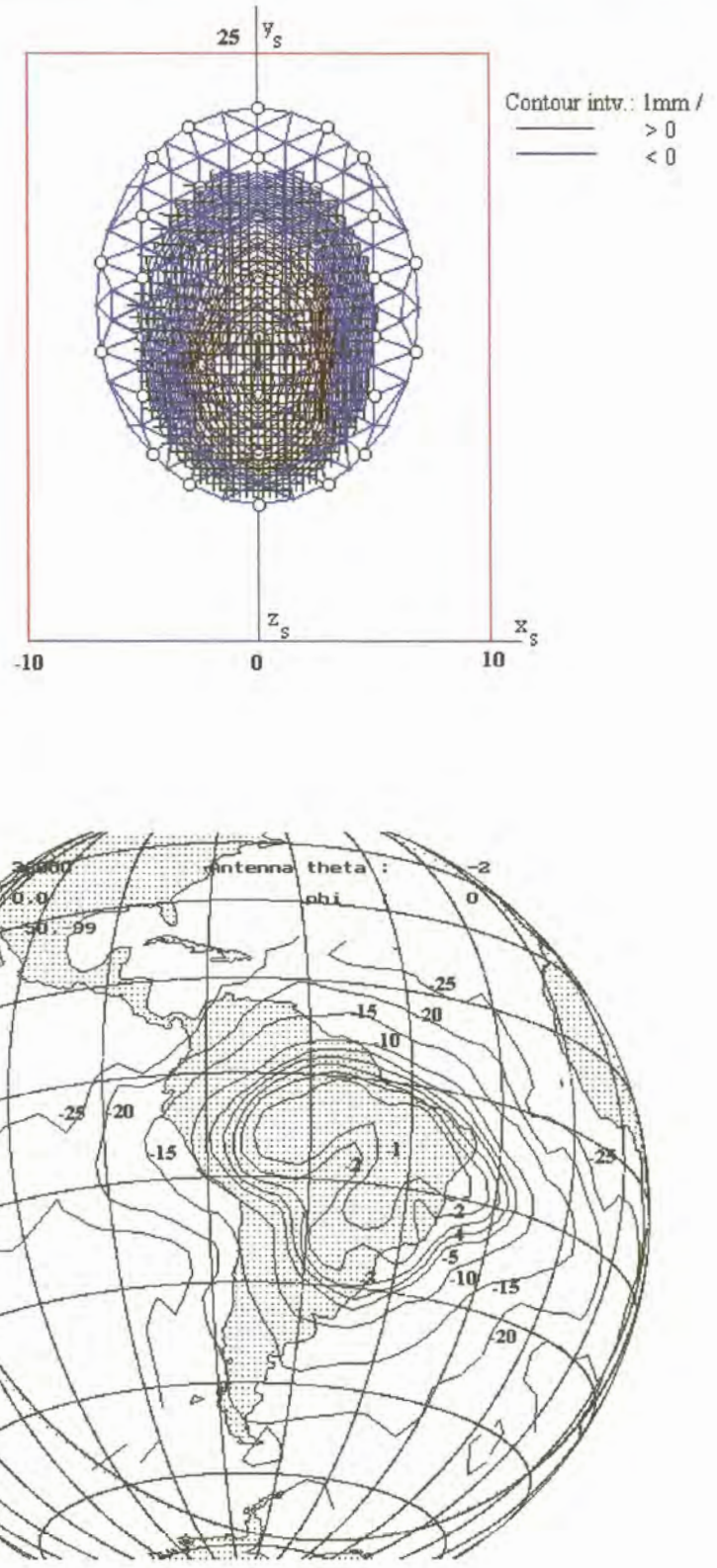

Figure 38. Synthesized subreflector surface and Brazilian co-polarized radiation pattern footprint.

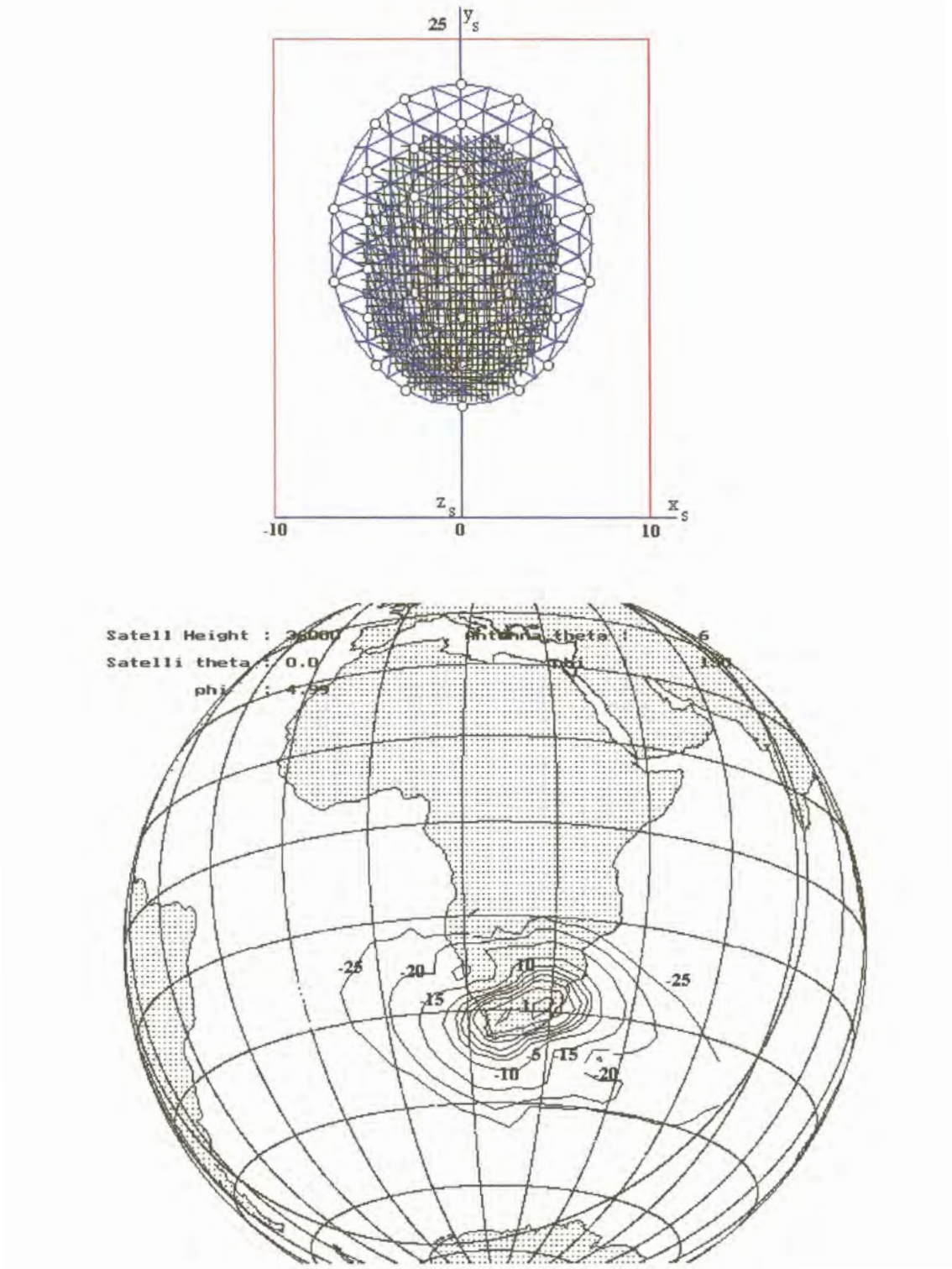

Figure 39. Synthesized subreflector surface and Southern African co-polarized radiation pattern footprint.

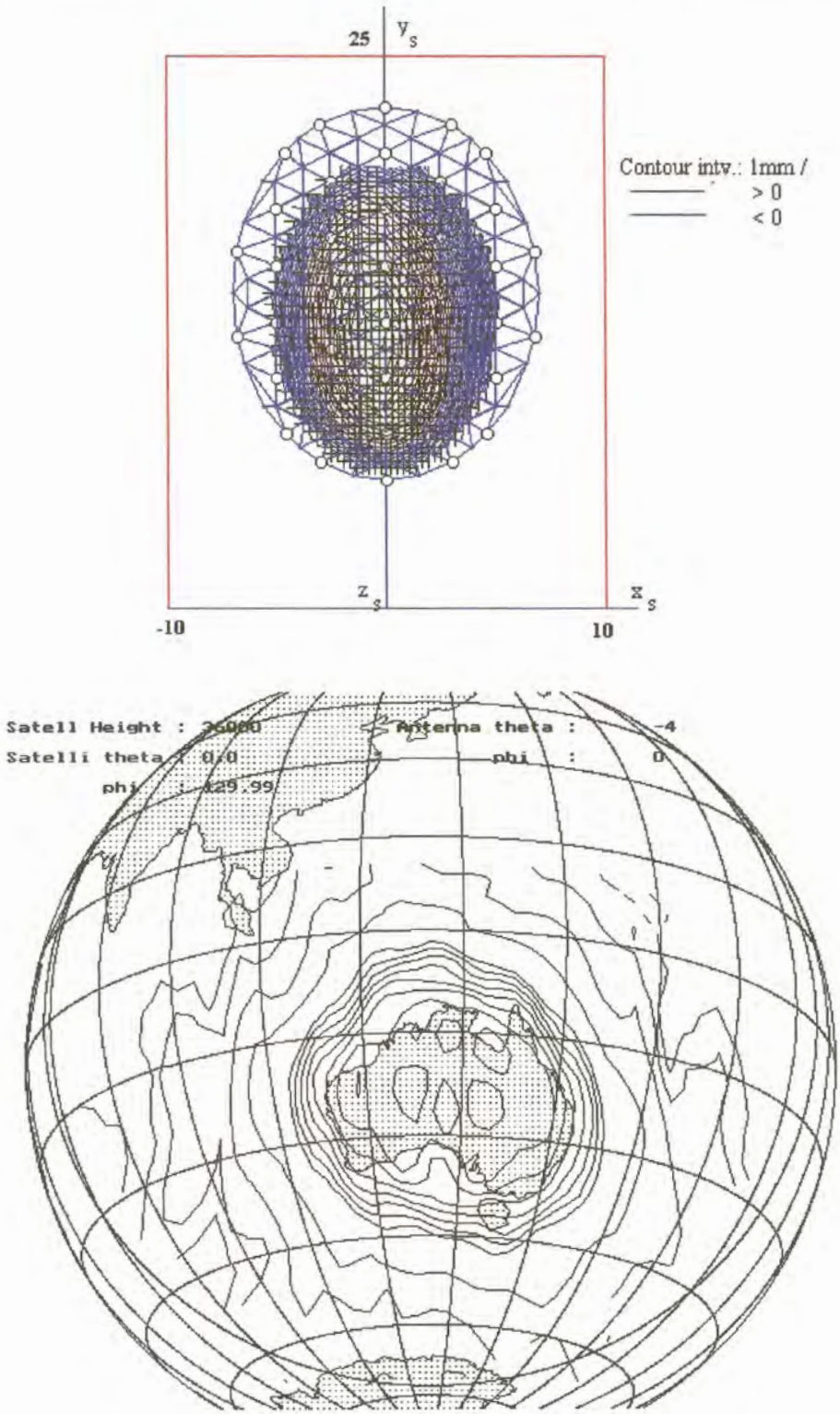

Figure 40. Synthesized subreflector surface and Australian co-polarized radiation pattern footprint.

Chapter 6: Conclusion

In this work the mechanically adjustable surfaces of dual offset reflector antennas have been studied as a possible solution to the problem of creating reconfigurable contour beams for application on geostationary satellites.

A motivation for studying this problem was provided in the introduction. It was stated that reconfigurability of contour beams would increase reflector antenna efficiency and be necessary to comply with FCC regulations on spillover allowed in adjacent geographical regions if the satellite operator or service area changes.

Various algorithms to compute the far-field of a DOSR antenna efficiently were investigated including the Jacobi-Bessel series expansion method and the pseudo sampling technique. The accuracy of the developed code was verified against a PO code developed at the Ohio State University by Rudduck and Lee. A new efficient method to calculate the far-field using a Gaussian beam expansion of the feed pattern to launch and reflect GB's from the main reflector of a front fed offset parabolic reflector, was used to synthesize a CONUS beam [5]. The subreflector analysis was done using UTD. These aspects were discussed in Chapter 2.

Methods to describe the surface using the modified Jacobi polynomial series and Fourier harmonics, which describe a complete orthogonal set over the unit circle, were used to synthesize contour beams. Various methods to describe and optimize the cost function including genetic algorithms and the steepest gradient solver were used.

A reconfigurable DOSR antenna was designed assuming a fixed shaped main reflector and a flexible metal coated surface subreflector. Piezoelectric actuators attached to a support structure will enable reconfiguration of the surface. A family of possible shapes were generated and used to perform an actuator placement study. The mechanical finite element description of the surface was then used to predict the antenna radiation footprint for a few cases [23]. After this it was concluded that the design would be a viable option to consider for future applications.

A mechanical finite element Delphi unit was then developed by Yoon [30] using a shell description of the surface. This unit was added and used in the synthesis software. The surface description could now be made directly in terms of actuator amplitudes and synthesis can thus also be performed directly in terms of the actuator amplitudes. This unique tool for contour beam synthesis is the main contribution of this work and is described in Chapter 5 where a case study to implement a rotating elliptical beam and three shaped beams in reconfigured configuration are also described.

Future work will concentrate on optimizing actuator numbers and placement as well as a method to use piezoelectric strips bonded to the back of the reflector surfaces. This will work will likely be performed under sponsorship from a major aerospace company.

7. References

[1] S.von Hoerner, "The Design of Correcting Secondary Reflectors," IEEE Trans. Antennas Propagation vol. AP-24, pp. 336-340, May 1976.

[2] P.R. Lawson and Y.L. Yen, "A Piecewise Deformable Subreflector for Compensation of Cassegrain Main Reflector Errors," IEEE Trans. Antennas Propag., vol. AP-36, pp.1342-1350, October 1988.

[3] B.S. Westcott, F.A. Stevens and F. Brickell, "GO synthesis of offset dual reflectors," IEE Proc., vol. 128, Pt. H, no. 1, pp. 11-18, Feb.1981.

[4] H.-T. Chou and P.H. Pathak, "Uniform asymptotic solution for electromagnetic reflection and diffraction of an arbitrary Gaussian beam by a smooth surface with an edge," Radio Science, vol. 32, no. 4 pp. 1319-1336, July-August 1997.

[5] H-T. Chou, W.H. Theunissen and P.H. Pathak, "Novel Gaussian Beam Approach for Fast Synthesis of Large Reflector Antenna Configurations for Contoured Beam Applications," Accepted for presentation at PIERS Symposium, March 1999, Taiwan.

[6] P.J.B. Clarricoats, A.D. Monk and H. Zhou, "Array-fed reconfigurable reflector for spacecraft systems," Electron. Lett., 30, (8), pp.613-614, 1994.

[7] T.H. Lee and R.C. Rudduck, "OSU Reflector Antenna Code - Version 3.0 (NECREF Version 3.0) User's Manual," The Ohio State University ElectroScience Laboratory Technical Report 318021, February 1994.

[8] C. Scott, "Modern Methods of Reflector Antenna Analysis and Design," Artech House, ISBN 0-89006-419-9, 1990.

[9] R.G. Kouyoumjian and P.H. Pathak, "A Uniform Geometric Theory of Diffraction for the Edge of a Perfectly Conducting Surface," IEEE Proc., vol. 62, pp. 1448-1461, Nov. 1974.

[10] B.S. Westcott, "Shaped Reflector Antenna Design." London Research Studies Press Ltd., 1983.

[11] D. Duan and Y. Rahmat-Samii, "A Generalized Diffraction Synthesis Technique for High Performance Reflector Antennas," IEEE Trans. Antennas Propag., vol. AP-43, pp. 27-40, January 1995.

[12] C.J. Sletten, "Reflector and Lens Antennas - Analysis and Design using Personal Computers," Artech House, ISBN 0-89006-240-4, 1988.

[13] K.W. Brown and A. Prata, "A Design Procedure for Classical Dual Offset Reflector Antennas with Circular Apertures," IEEE Trans. Antennas Propag., vol. AP-42, No. 8, August 1994.

[14] A.W. Rudge, Milne, A.D. Olver and Knight, "The Handbook of Antenna Design Volume 1," Peter Peregrinus, ISBN 0-906048-82-6, 1982.

[15] Y. Rahmat-Samii and V. Galindo-Israel, "Shaped Reflector Analysis using the Jacobi-Bessel Series," IEEE Trans. Antennas Propag., vol. AP-28, No. 4, July 1980.

[16] A. Papoulis, "A new algorithm in spectral analysis and band limited extrapolation," IEEE Trans. On Circuits and Systems, vol. CAS-22, no. 9, September 1975.

[17] J. Michael Johnson and Y. Rahmat-Samii, "Genetic Algorithms in Engineering Electromagnetics,", IEEE AP Magazine, Vol. 39, No.4, August 1997, pp. 7-21.

[18] D.E. Goldberg, "Genetic Algorithms in Search, Optimization and Machine Learning," Addison-Wesley Publishing, ISBN 0-201-15767-5, 1989.

[19] R.L. Haupt, "An Introduction to Genetic Algorithms for Electromagnetics,", IEEE AP Magazine, Vol. 37, No. 2, April 1995, pp. 7-15.

[20] A.R. Cherrette, S.W. Lee and R.J. Acosta, " A Method for Producing a Shaped Contour Radiation Pattern Using a Single Reflector and a Single Feed," IEEE Trans. Antenn. Propagat., vol.37, no.6, pp. 698-702, June 1989.

[21] H.-S. Yoon and G. Washington, "Piezoceramic actuated aperture antennas," Smart Mater. Struct. vol.7(1998), pp. 537-542.

[22] H.-H. Viskum, S.B. Sørensen and K. Pontoppidan, "A dual reflector system with a reconformable subreflector," IEEE AP-S Symposium and USNC/URSI Nat. Radio Science Meeting, Atlanta, 1998.

[23] W.H.Theunissen, Hwansik T. Yoon, G. Washington and W.D. Burnside, "Reconfigurable Contour Beam Reflector Antennas using Adjustable Subreflector and an Adjustable Single Feed," Accepted for publication IEEE Microwave and Optical Technology Letters, July 1999.

[24] E.O. Brigham, "The fast Fourier transform and its applications," Prentice-Hall International, 1985.

[25] V. Krichevsky and D.F. DiFonzo, "Optimum Beam Scanning in Offset Single and Dual Reflector Antennas," IEEE Trans. Antennas Propag., vol. AP-33, No. 2, February 1985.

[26] S.W. Lee, "Differential Geometry for GTD Applications," Electromagnetics Laboratory Report No. 77-21, University of Illinois at Urbana-Champaign.

[27] W.H. Theunissen, "Qualification of an X-band Spaceborne Patch Array Antenna," 1991 SAIEEE Symposium, July 1992, Johannesburg South Africa.

[28] G. Washington, "Smart aperture antennas," Smart Mater. Struct. vol. 5(1996), pp. 801-805.

[29] H-S.Yoon, G. Washington and W.H. Theunissen, "Analysis of Doubly Curved Antenna Structures," Submitted to IEEE Trans. Antennas and Propagat.

[30] W.H.Theunissen, Hwansik T. Yoon, G. Washington and W.D. Burnside, "Mechanical finite element diffraction synthesis of reconfigurable contour beams from dual offset reflector antennas," Submitted to IEEE Trans. Antennas and Propagat.

[31] W.H.Theunissen, Hwansik T. Yoon, G. Washington and W.D. Burnside, "Mechanical finite element diffraction synthesis of reconfigurable contour beams from dual offset reflector antennas," Accepted for presentation at IEEE AP-S International Symposium and USNC/URSI National Radio Science Meeting, Orlando Florida, July 1999.

[32] W.H. Theunissen, J.W. Odendaal and J. Joubert, "Using Measured Feed Data in Dual Reflector System Software Models to Predict Antenna Parameters," Presented at the 10th IEE Conference, Edinburgh, Scotland, April 1997.